De novo macrocyclic peptides for inhibiting, stabilising and probing the function of the Retromer endosomal trafficking complex

Kai-En Chen[1], Qian Guo[1#], Timothy A. Hill[1,2#], Yi Cui[3], Amy K. Kendall[4,5], Zhe Yang[3], Ryan J. Hall[1], Michael D. Healy[1], Joanna Sacharz[6], Suzanne J. Norwood[1], Sachini Fonseka[1], Boyang Xie[4,5], Robert C. Reid[1,2], Natalya Leneva[1,7], Robert G. Parton[1,8], Rajesh Ghai[1,9], David A. Stroud[6], David P. Fairlie[1,2], Hiroaki Suga[10], Lauren P. Jackson[4,5], Rohan D. Teasdale[3], Toby Passioura[10,11], Brett M. Collins[1]*

1. The University of Queensland, Institute for Molecular Bioscience, St. Lucia, Queensland, 4072, Australia.
2. ARC Centre of Excellence for Innovations in Peptide and Protein Science, Institute for Molecular Bioscience, The University of Queensland, St. Lucia, Queensland, 4072, Australia.
3. The University of Queensland, School of Biomedical Sciences, St Lucia, Queensland, 4072, Australia.
4. Department of Biological Sciences, Vanderbilt University, Nashville, TN 37232, USA.
5. Center for Structural Biology, Vanderbilt University, Nashville, TN 37232, USA.
6. Department of Biochemistry and Molecular Biology, Bio21 Molecular Science and Biotechnology Institute, University of Melbourne, Parkville, 3052 Victoria, Australia.
7. Current address: Cambridge Institute for Medical Research, Cambridge, CB2 0XY, UK.
8. The University of Queensland, Centre for Microscopy and Microanalysis, Queensland, Australia.
9. Current address: CSL Ltd, Parkville, Victoria, 3052, Australia.
10. Department of Chemistry, Graduate School of Science, The University of Tokyo, 7-3-1 Hongo, Bunkyo-Ku, Tokyo 113-0033, Japan.
11. Sydney Analytical, School of Life and Environmental Sciences and School of Chemistry, The University of Sydney, Camperdown, New South Wales 2050, Australia.

#These authors contributed equally.

***Corresponding author:** Brett M. Collins, Tel: +61-7-3346-2043, b.collins@imb.uq.edu.au

Running title: Cyclic peptides targeting Retromer

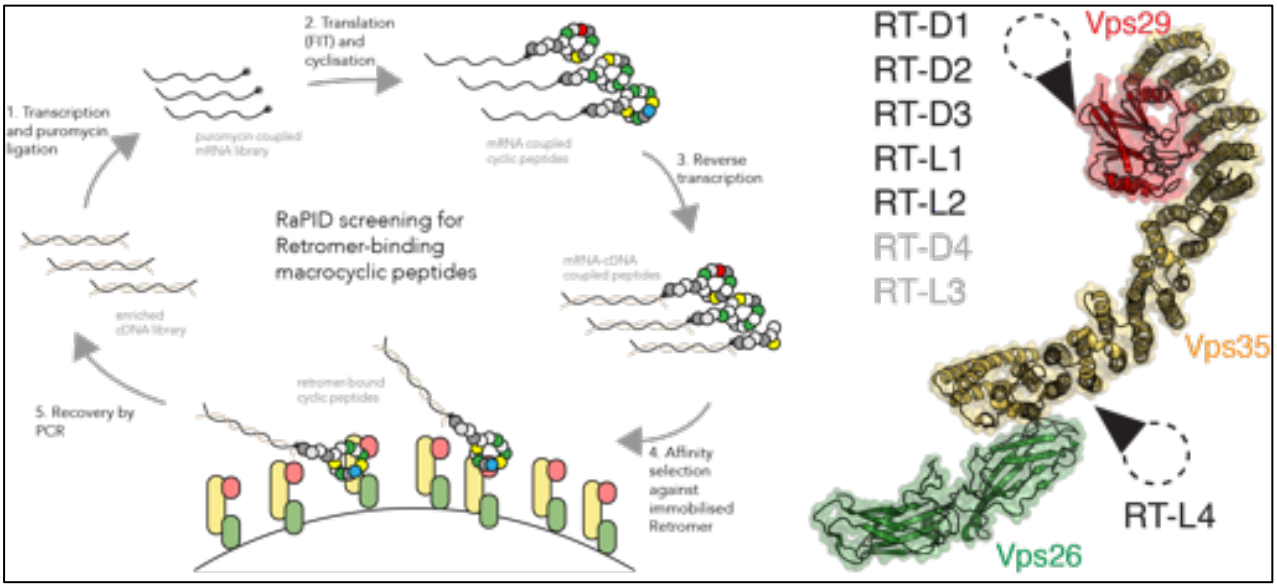
1. Transcription and puromycin ligation
puromycin coupled mRNA library
2. Translation (FIT) and cyclisation
mRNA coupled cyclic peptides
3. Reverse transcription
mRNA-cDNA coupled peptides
4. Affinity selection against immobilised Retromer
retromer-bound cyclic peptides
5. Recovery by PCR
enriched cDNA library
RaPID screening for Retromer-binding macrocyclic peptides
RT-D1
RT-D2
RT-D3
RT-L1
RT-L2
RT-D4
RT-L3
Vps29
Vps35
Vps26
RT-L4

1

ABSTRACT (150 words)

The Retromer complex (Vps35-Vps26-Vps29) is essential for endosomal membrane trafficking and signalling. Mutation of Retromer subunit Vps35 causes late-onset Parkinson's disease, while viral and bacterial pathogens can hijack the complex during cellular infection. To modulate and probe its function we have created a novel series of macrocyclic peptides that bind Retromer with high affinity and specificity. Crystal structures show the majority of cyclic peptides bind to Vps29 via a Pro-Leu-containing sequence, structurally mimicking known interactors such as TBC1D5, and blocking their interaction with Retromer *in vitro* and in cells. By contrast, macrocyclic peptide RT-L4 binds Retromer at the Vps35-Vps26 interface and is a more effective molecular chaperone than reported small molecules, suggesting a new therapeutic avenue for targeting Retromer. Finally, tagged peptides can be used to probe the cellular localisation of Retromer and its functional interactions in cells, providing novel tools for studying Retromer function.

INTRODUCTION

Endosomal compartments serve as central hubs for transmembrane protein and lipid sorting, and as platforms for cell signalling. Transmembrane protein cargos that arrive in the endosomal network via endocytosis or anterograde trafficking are routed either for lysosomal degradation or recycling to other compartments including the trans-Golgi network (TGN) and the cell surface. Endosomal trafficking thus plays a pivotal role in maintaining cellular homeostasis and this is controlled by a number of essential protein machineries (*1-3*).

The evolutionarily conserved Retromer complex composed of Vps26, Vps29 and Vps35 is a master regulator of endosomal dynamics responsible for cargo sorting and recycling within tubulovesicular transport carriers (*2, 4-8*), and in higher eukaryotes cooperates with an array of cargo adaptors and accessory proteins to allow membrane recruitment, cargo sorting and trafficking to occur (*2, 3, 9*). The known cargo adaptors are derived from the sorting nexin (SNX) protein family and include SNX3 and SNX27.

Retromer mutation or dysregulation in humans leads to defective endosomal and lysosomal function implicated in neurodegenerative disorders including Parkinson's disease (PD) (*10-15*), Alzheimer's disease (AD) (*16-19*) and amyotrophic lateral sclerosis (ALS) (*20*). Retromer dysfunction impacts endosomal and lysosomal homeostasis in neurons and microglia in multiple ways (*11, 21*); involving deficits in regulatory protein interactions such as WASH and Leucine-rich repeat kinase 2 (LRRK2) (*14, 22, 23*), mis-sorting of specific endosomal cargos (*10, 24-27*), defects in mitochondrial function and mitophagy (*28-31*), and other widespread deficiencies in lysosomal and autophagic degradation of toxic material (*14, 17, 19, 32-34*). Retromer is also a prominent target hijacked by intracellular pathogens to facilitate their transport and replication. This includes viruses such as SARS-CoV-2, human immunodeficiency virus (HIV), hepatitis C virus (HCV), and human papilloma virus (HPV) (*35-39*), and intracellular bacteria such as *Coxiella burnetii* and *Legionella pneumophila* (*40-44*). Mechanistic studies have shown that the secreted effector protein RidL from *L. pneumophila* binds directly to Vps29, competing with endogenous regulators TBC1D5 and VARP, inhibiting Retromer mediated cargo transport, and supporting the growth of *L. pneumophila* in intracellular endosome-derived vacuoles (*40, 41, 43, 44*). Similarly, the minor capsid protein L2 from human Papilloma virus (HPV) is thought to hijack Retromer-SNX3-mediated endosomal transport by mimicking sequence motifs found in endogenous cargoes such as the cation-independent mannose-6-phosphate receptor (CI-MPR) and divalent metal transporter 1-II (Dmt1-II) (*38, 45*).

Given the importance of Retromer in endosomal trafficking, neurodegenerative disease, and cellular infection, there is significant interest in developing molecular approaches to either inhibit or enhance Retromer activity. Inhibition of Retromer may provide a novel avenue for targeting infectious pathogens. For example peptide-based inhibitors of Retromer, derived from the HPV L2 protein, are able to reduce infection by slowing the normal retrograde transport of incoming virions (*38, 45*). Conversely, because of its neuroprotective role, Retromer-binding 'molecular chaperones' may be used to enhance Retromer function in diseases including AD, PD and ALS, with the goal of boosting normal endosome-dependent clearance pathways to reduce accumulation of toxic aggregates of proteins such as amyloid β (Aβ), tau and α-synuclein (*46, 47*). Previously a small molecule called R55 (also called TPT-260) was identified, which can bind with modest affinity to

Retromer at the interface between Vps35 and Vps29 and stabilise its structure (*48*). This molecule has since been shown to have activity in stabilising Retromer in cells, and as predicted can enhance the transport of essential receptors and reduce the accumulation of toxic material including Aβ and α-synuclein in cell, fly, and mouse models (*33, 48-51*). Recently a derivative of R55 was found to improve Retromer stability and lysosomal dysfunction in a model of ALS (*20*). Nonetheless, the low potency and specificity of these compounds mean that other molecules are actively being sought.

We have adopted a novel screening strategy, referred to as the RaPID (Random nonstandard Peptides Integrated Discovery) system, to identify a series of eight *de novo* macrocyclic peptides with high affinity and specificity for Retromer, possessing either inhibitory or stabilising activities. These peptides bind to Retromer with affinities (K_d) ranging from 0.2 to 850 nM and can be classified into two groups based on their binding sites. Most interact specifically with the Vps29 subunit, and crystal structures show that these peptides associate with a highly conserved pocket on Vps29 that is also used by the accessory proteins TBC1D5 and VARP, as well as the bacterial protein RidL, and are potent inhibitors of their binding. We also identified one peptide, RT-L4, that shows *in vitro* activity as a molecular chaperone. RT-L4 stabilizes Retromer assembly via binding to the interface between Vps26 and Vps35, does not disrupt Retromer's association with known accessory proteins and cargo adaptors, and indeed allosterically enhances binding to several ligands including SNX27 and TBC1D5. Finally, using reversible cell permeabilization and fluorescent peptides, we demonstrate that they specifically co-label Vps35-positive endosomal structures, can perturb endosomal recruitment of TBC1D5 by Retromer, and can be used as baits for isolating Retromer from cells. These macrocyclic peptides thus provide novel research tools and suggest potential new avenues for developing therapeutic modifiers of Retromer function.

RESULTS

Identification of highly potent Retromer-binding macrocyclic peptides

The procedure of the RaPID system (**Fig. 1A**) exploits the diverse molecular topology of macrocyclic peptide populations numbering >10^{12} unique sequences to enrich for and amplify low abundance, high-affinity ligands (*23, 52-55*). We performed the RaPID selection using purified His-tagged human Retromer complex as bait: a puromycin-linked semi-randomized messenger RNA library, of the general form AUG-$(NNK)_{4-15}$-UGC, was translated in an *in vitro* translation reaction to generate peptides covalently linked to their cognate mRNAs through the puromycin moiety. Macrocyclization was effected through genetic code reprogramming of initiating AUG (methionine) codons to incorporate either *N*-chloroacetyl-L-tyrosine (ClAc-L-Tyr) or *N*-chloroacetyl-D-tyrosine (ClAc-D-Tyr), leading to spontaneous reaction with a downstream UGC-encoded cysteine to form a library of thioether bridged cyclic peptides each linked to their cognate mRNA (total diversity >10^{12} molecules). Retromer ligands were then identified through iterative cycles of affinity selection against immobilised Retromer complex followed by RT-PCR recovery, transcription and regeneration of peptide-mRNA fusion libraries, with deconvolution of the final enriched library achieved through next-generation sequencing.

We selected the four most abundant peptides from each of the ClAc-L-Tyr or ClAc-D-Tyr initiated libraries (**Fig. 1B**; **Fig. S1; Table S1**) for further characterisation, and each was synthesised using standard Fmoc chemistry. These were validated against the Retromer complex by surface plasmon resonance (SPR) and all were confirmed to bind very strongly to Retromer with affinities (K_ds) in the range of <0.2 to 30 nM (**Fig. S2**). Secondary SPR comparisons showed that these molecules also bound the purified Retromer complex from *Danio rerio* (zRetromer) (**Fig. S2**) and the thermophilic yeast *Chaetomium thermophilum* (ctRetromer) with a similar range of binding affinities, indicating that they associate with evolutionarily conserved sites in the complex.

Macrocyclic peptide binding to Retromer was validated using isothermal titration calorimetry (ITC). Among the eight cyclic peptides tested, six were confirmed to bind Retromer with nanomolar binding affinity while the peptides RT-D4 and RT-L3 were not sufficiently soluble for ITC experiments (**Figs. 1C and 1D; Table S2**). Affinities for Retromer measured by ITC were systematically lower but correlated well with those measured by SPR, ranging from 25 to 850 nM. These affinities are comparable to or better than the high affinities for the Retromer binding regulatory protein TBC1D5 (220 nM) (*56*), or the bacterial effector RidL (150 nM) (*43, 44*).

The Retromer structure consists of a long Vps35 α-helical solenoid, with Vps26A or Vps26B bound to the N-terminus and Vps29 bound at the C-terminus (**Fig. 1E**) (*57-61*). We examined the specific subunits of Retromer required for binding each of the cyclic peptides by testing either Vps29 alone, Vps26A alone, the Vps35-Vps29 heterodimer, or sub-complexes of Vps26A with N-terminal fragments of Vps35 (**Fig. 1D; Table 1)**. Full-length Vps35 is relatively unstable on its own and was not tested separately. Interestingly, RT-D1, RT-D2, RT-D3, RT-L1 and RT-L2 all bind specifically to either Vps29 alone or to the Vps35-Vps29 heterodimer, but not to Vps26A. Their affinities for Vps29 alone were not significantly different to their

binding to the Retromer holo-complex or Vps35-Vps29 heterodimer, ranging from 8 to 783 nM. This indicates they bind specifically and exclusively to the Vps29 subunit. Although peptides RT-D4 and RT-L3 were not tested for binding specific subunits, it is likely they also bind to Vps29 as they possess a Pro-Leu motif that we show below mediates Vps29 interaction by the other five peptides (**Figs. 1B and 1E**).

In contrast to other peptides, RT-L4 did not bind to any of the Retromer subunits individually or to the Vps35-Vps29 dimer, but rather only to sub-complexes that contained *both* Vps26A and Vps35 (**Fig. 1C**). N-terminal fragments of Vps35 in complex with Vps26A, including $Vps35_{1-390}$, and $Vps35_{1-224}$ supported binding to the RT-L4 peptide with a similar affinity to the Retromer trimeric holo-complex, while $Vps35_{1-390}$ on its own did not (**Fig. 1D**). When Vps35 was truncated to the shortest region still capable of Vps26A interaction ($Vps35_{1-172}$) a small but consistent decrease in binding affinity was observed, suggesting that α-helix 8 in Vps35 (residues 175 to 195) of Vps35 contributes to the binding but is not essential. Overall, we have found that the cyclic peptides RT-D1, RT-D2, RT-D3, RT-L1 and RT-L2 (and likely RT-D4 and RT-L3) bind specifically to Vps29, but RT-L4 binding occurs at the interface between the Vps26A and Vps35 subunits (**Fig. 1E**).

Macrocyclic peptides bind to Vps29 through a conserved site mimicking endogenous accessory proteins

To understand the molecular basis of how the discovered macrocyclic peptides bind to Retromer, we next co-crystallized Vps29 with RT-D1, RT-D2, RT-D3, RT-L1 and RT-L2. With extensive crystallization trials, we successfully solved structures of human Vps29 in complex with RT-D1, RT-D2, RT-L1 and RT-L2 (**Fig. 2; Table S3**). For RT-D3, the complex structure was successfully determined using Vps29 from *C. thermophilum* (ctVps29). In all five complex structures the conformation of Vps29 is highly similar to apo Vps29 (root mean square deviation ranges from 0.6 Å to 1.3 Å), with cyclic peptide density clearly visible (**Fig. 2A; Fig. S3A**). Surprisingly, although the precise details differed for each macrocyclic peptide, they all bound to the same hydrophobic surface groove on Vps29 composed of multiple conserved residues including Leu2, Leu25, Leu152, Tyr163, Tyr165 and Val174 (human numbering) (**Fig. 2B**). This hydrophobic cavity is highly conserved throughout evolution (**Fig. 2B**) and is located on the opposite surface of Vps29 relative to the Vps35 binding region (**Fig. 2C**).

Each cyclic peptide adopts a different conformation when bound to Vps29, as expected from their lack of sequence identity (**Fig. 2D; Fig. S3B**). However, a notable feature of all of the Vps29 binding peptides is a Pro-Leu di-peptide motif present in a β-hairpin structure that inserts into the conserved hydrophobic site on Vps29 (**Fig. 1B; Figs. 2D and 2E**). Further analysis reveals the residue in front of the Pro-Leu motif (position -1, with the Pro designated as position '0') is important for stabilizing the β-hairpin like configuration, forming multiple hydrogen bonds with nearby residues including the side-chain hydroxyl group of Vps29 Tyr165 (**Figs. 2D and 2E**). Notably TBC1D5, VARP and the bacterial hijacking molecule RidL all engage Vps29 at the same site, employing a similar Pro-Leu dipeptide at their core (**Fig. 2F**) (*40, 43, 44, 56, 62-64*).

147 The Vps29-binding peptides that we have identified mimic the interactions of endogenous and bacterial
148 ligands but bind with higher affinity. We assessed the importance of peptide cyclisation for this increased
149 affinity using a linear version of RT-D1 and found that this reduced the affinity by ~six-fold to 0.76 μM (**Fig.**
150 **S3C**). In addition to the core Pro-Leu di-peptide motif and the cyclic structure, the residues at positions +4 to
151 +7 of the peptides also form extensive contacts with a surface groove composed of Vps29 side chains Val172,
152 Lys173 and Val174 (**Fig. 2D; Fig. S3B**). Again, using RT-D1 as an example, we found that mutations of these
153 residues (positions +4, +5, +7 and +8) to alanine significantly reduced the affinity for Retromer to ~2.2 μM
154 (**Fig. S3C**). Interestingly, this interaction network is shifted by 8 Å towards Lys188 in the ctVps29 – RT-D3
155 structure (equivalent to Arg176 in human Vps29), which may explain the weaker binding of ctVps29 to RT-
156 D3 compared to human Vps29 (**Fig. 2D; Fig. S3D**). Another noteworthy observation was found in the Vps29
157 – RT-L1 structure, where a potential secondary cyclic peptide binding pocket was identified, surrounded by
158 helix 3 and Ile91 of Vps29 (**Fig. S3E**), a region known to be required for Vps35 binding. In this binding pocket,
159 we found two RT-L1 peptides are bound to each other, forming extensive contacts with residues located on
160 helix 3 and adjacent loop region of Vps29 (**Fig. S3F**). This binding of RT-L1 to a secondary site in Vps29 is
161 likely due to a crystallisation-induced contact, but it could suggest a potential site for targeting the Vps29-
162 Vps35 interaction in the future.
163
164 ***The RT-L4 macrocyclic peptide is a molecular chaperone that binds to the interface between Vps26A and***
165 ***Vps35***
166 One of our initial goals was to identify potential molecular chaperones that can stabilise the Retromer complex,
167 hence we next assessed the impact of the macrocyclic peptides on the thermal stability of Retromer using
168 differential scanning fluorimetry (DSF) (**Fig. S4A**). The Vps29-binding peptides RT-D1, RT-D2, RT-D3, RT-
169 L1 and RT-L2 all increased the melting temperature (T_m) of Vps29 upon addition of a 20-fold molar excess
170 (**Fig. S4A**), consistent with their high affinities. In contrast however, none of the Vps29-specific macrocyclic
171 peptides had a significant impact on the thermal stability of the trimeric Retromer holo-complex (**Fig. S4B**).
172 This suggests that increasing the thermal stability of Vps29 alone is insufficient to enhance the stability of the
173 entire Retromer complex in solution. In contrast, the addition of RT-L4 resulted in a substantial 2°C to 6.5°C
174 enhancement in the T_m of the Retromer holo-complex in a dose-dependent manner (**Fig. 3A; Figs. S4C and**
175 **S4D**). Similarly, the RT-L4 peptide resulted in an 8°C increase in T_m for the Vps26A-Vps35$_{1-390}$ sub-complex,
176 and as expected in control experiments it did not affect the thermal stability of either Vps26A or Vps29 alone
177 (**Fig. S4C**). Using mass photometry, we found that the Retromer holo-complex was maintained at its trimeric
178 state upon the addition of cyclic peptides, suggesting that the enhancement in the T_m of the Retromer was not
179 the result of high-order oligomer formation (**Fig. S5A**). These results together indicate that RT-L4 stabilizes
180 Retromer through its interaction at the interface between Vps26A and Vps35, possibly by acting as a molecular
181 'staple' between the two subunits. In parallel, we also compared the binding and thermal stability effect of RT-
182 L4 against the previously published Retromer chaperone R55 and its derivative compound 2a (*20, 48*). Using
183 ITC we confirmed that both chaperone R55 and compound 2a bind Retromer, but with much lower affinity

than RT-L4 (**Table S4; Fig. S5B**). While we observed weak binding, we were unable to detect significant improvement in the T_m of Retromer in the presence of either R55 or compound 2a under the same experimental conditions as RT-L4 (**Fig. S5C**). Even in the presence of 1 mM R55 (> 300-fold molar excess) little impact on Retromer stability was detectable (**Fig. S5D**), although a second unfolding event was observed that might indicate partial stabilisation of the Vps29-Vps35 complex (*20, 48*). The difference is likely explained by lower binding affinity of both R55 and compound 2a to Retromer. Our results thus indicate that RT-L4 can act as a potent molecular stabiliser of Retromer *in vitro*.

Next, we sought to map the exact binding region of RT-L4 to better investigate the mechanism of its interaction and how this results in the enhanced thermal-stability of Retromer. Using ITC we found that RT-L4 binds to zRetromer with a K_d of 80 nM, which is highly comparable to human Retromer or the Vps26A-Vps35$_{1-390}$ sub-complex (**Table S2**; **Fig. S6A**). In contrast, RT-L4 binds with lower affinity to ctRetromer with a K_d of 6 μM (**Table S2**; **Fig. S6B**). As our data indicated that RT-L4 binds to a site that is formed by a combined interface on Vps35-Vps26A, streptavidin agarose beads coated with biotinylated RT-L4 were used to pulldown purified Vps26A-Vps35$_{1-390}$ incorporating several specific point mutations, and this revealed that peptide binding was abolished by a D128R mutation in Vps35 (**Fig. 3B**). The Asp128 side-chain is part of a conserved surface adjacent to the Vps35-Vps26A interface (**Fig. 3C**), and makes a minor contact with the extended N-terminus of SNX3 when in a ternary complex with the SNX3 adaptor and ΩΦ[LV] sequence containing-cargo peptides (where Ω and Φ are aromatic and hydrophobic side-chains) (*3, 59*). In contrast, RT-L4 contains a number of aromatic residues that could potentially contribute to high affinity binding. Indeed, mutation of any of these residues to alanine shows that they are essential for Retromer interaction (**Fig. 3D** and **3E**). Similarly, the linear form of RT-L4 was unable to bind to Retromer (**Fig. 3D**), suggesting both aromatic residues and peptide cyclisation are critical for the interaction.

With the multiple attempts to co-crystallize RT-L4 without success, we further explored the site where RT-L4 binds Retromer using single particle cryo-electron microscopy (cryoEM). In previous work, wild-type Retromer was found to form a mixed population of hetetrotrimers and multiple higher order oligomers in vitreous ice, so we used an established mutant called "3KE Retromer" (point mutations E615A/D616A/E617A in Vps35) that favours the heterotrimeric species over higher order oligomers for our analyses (*61*). We determined structures of both apo and RT-L4-bound 3KE Retromer under the same conditions to ascertain whether the RT-L4 binding site could be identified (**Fig. 3F-H**; **Figs. S6C-F**; **Table S5**). At the current resolution we detected no structural differences between wild-type heterotrimer (*61*) and the 3KE mutant. Comparison of our reconstructions indicates there is additional density at the Vps26-Vps35 interface in the presence of the RT-L4 peptide, although the estimated resolution of apo and RT-L4/Retromer structures (~5.9 Å; 0.143 FSC cut-off in RELION) is too low to unambiguously assign peptide density (**Figs. 3F-H**; **Figs. S6C and S6D**). Overall, our cryoEM data shows that there are no gross structural changes in Retromer induced by the RT-L4 peptide, and although not conclusive these reconstructions provide support for our biophysical and mutagenesis data indicating that RT-L4 binds and stabilizes Retromer at the Vps26/Vps35 interface. Higher

220 resolution data will be required however to unambiguously identify specific residues in both Retromer and the
221 peptide that mediate the interaction.
222
223 ***The impact of cyclic peptides on the interactions between Retromer and known regulatory proteins***
224 Given the high affinity and specificity of the macrocyclic peptides for Retromer, it was critical to assess their
225 potential effects on Retromer's interaction with essential regulatory, accessory and adaptor proteins. We used
226 RT-L4, with its distinct affinity for the Vps26-Vps35 complex, and RT-D3 as a representative Vps29-binding
227 peptide, and tested Retromer binding proteins for which binding mechanisms were known including TBC1D5
228 (*56*), SNX3 (*59*), Fam21 (*65*), SNX27 (*66*) and the bacterial hijacking molecule RidL (*40, 43, 44*) (**Figs. 4A-**
229 **E; Fig. S7A**). GST-tagged TBC domain of human TBC1D5 ($TBC1D5_{TBC}$) bound Retromer in pulldowns, and
230 this interaction was inhibited by addition of RT-D3 as expected based on their overlapping binding site (**Fig.**
231 **4A**). A similar result was observed using ITC, where we observed binding between $TBC1D5_{TBC}$ and Retromer
232 with a K_d of 370 nM (consistent with previous reports (*56*)), while binding was undetectable in the presence
233 of competing RT-D3 (**Fig. 4B, Table S6**). The same inhibitory effect was also observed for the N-terminal
234 region of the bacterial effector RidL ($RidL_{1-236}$) (**Fig. S7A**). In contrast, while the addition of RT-D3 blocked
235 Retromer from interacting with $TBC1D5_{TBC}$ or RidL as would be predicted from their overlapping binding
236 sites, it had no impact on Retromer binding to either SNX27 or SNX3 as assessed in pulldowns and ITC
237 experiments (**Figs. 4A, 4C, and 4D**). Note that for ITC and pull-down experiments with SNX3, we found it
238 was necessary to include a synthetic peptide corresponding to DMT1-$II_{550-568}$ containing a ΩΦ[LV] cargo motif
239 (where Ω = an aromatic side-chain and Φ = a hydrophobic side-chain) (*59*). In the absence of this peptide we
240 could not detect binding of SNX3 to Retromer, likely because SNX3 and cargo motifs form a co-dependent
241 binding interface with the Retromer complex (*3, 59*). To our surprise, the addition of RT-D3 modestly affected
242 Retromer binding to Fam21 C-terminal LFa repeats 19 to 21 (**Figs. 4A and 4E**), a sequence known to associate
243 with a C-terminal region of Vps35 (*22, 65*). It is therefore likely that Vps29 contributes partially to the binding
244 of LFa sequences of Fam21 as previously reported (*67*), and RT-D3 either directly competes with Fam21 or
245 allosterically affects the Fam21 binding site. These results were further validated using qualitative pulldowns
246 from HeLa cell lysates with biotinylated RT-D3 peptide, where specific loss of TBC1D5 and VARP binding
247 was seen, without any effect on the association of other Retromer ligands SNX27, Fam21, SNX3 and SNX27
248 (**Fig. 4F**). Altogether our data indicates RT-D3 can specifically inhibit binding to TBC1D5, and most likely
249 will also compete with other proteins such as VARP and RidL that bind to the same conserved hydrophobic
250 cavity on Vps29.
251 In contrast to RT-D3, we found that the RT-L4 peptide had little negative impact on the interaction of
252 Retromer with any ligands tested. In GST-pulldowns using purified proteins or using biotinylated peptides and
253 HeLa lysates Retromer was able to interact with TBC1D5, VARP, Fam21, SNX27 and the SNX3-DMT1-II
254 complex in the presence of RT-L4 (**Figs. 4A and 4E**). Interestingly, by ITC we found that the affinity and
255 enthalpy of binding between Retromer for either $SNX27_{PDZ}$, $TBC1D5_{TBC}$, or $Fam21_{R19-R21}$ were substantially

256 improved by the addition of RT-L4 (**Figs. 4B, 4D and 4E; Fig. S7B; Table S6**). The enhancement of Retromer
257 binding to $TBC1D5_{TBC}$ by RT-L4, also led to a slight improvement of GAP-stimulated GTP hydrolysis of
258 Rab7a (**Fig. S7C and S7D**). In the case of SNX27, the binding between $SNX27_{PDZ}$ and PDZ-dependent cargo
259 peptide, $PTHR_{586-593}$, was also further improved to a K_d of 700 nM by the presence of RT-L4 (**Fig. 4G**). This
260 suggests that the stabilization of Retromer by RT-L4 may be able to enhance binding to some of its key
261 partners, promote GAP activity, and possibly also improve cargo recognition. However, we did observe a
262 modest reduction in the binding affinity of Retromer for the SNX3-DMT1-II complex from 154 μM to 230
263 μM in the presence of RT-L4 (**Fig. 4C; Table S6**). We speculate that there may be a small degree of overlap
264 between the binding site for RT-L4 and the first part of the N-terminal loop of SNX3, although not enough to
265 perturb the interaction dramatically. Given this subtle change however, we then asked whether the peptide
266 would perturb the interactions between Retromer and SNX3 in the presence of a lipid membrane. To do this,
267 we performed a liposome binding assay, where we fused a palmitoylated fatty acid to the N-terminus of a
268 cargo peptide. For these experiments we used a sequence derived from the CI-MPR ($CIMPR_{2347-2376}$) and
269 allowed it to insert into liposomes compose of Folch I lipids supplemented with the SNX3-binding
270 phosphatidylinositol-3-phosphate (PtdIns3*P*) (**Fig. 4H; Figs. S7E and S7F**). In our control experiments, we
271 found that SNX3 alone was capable of binding Folch I - PtdIns3*P* liposomes both in the presence and absence
272 of cargo peptide. In contrast, Retromer only bound stably to PtdIns3*P*-containing liposomes when both SNX3
273 *and* cargo peptides were added, similar to previous studies (*68*). In the presence of RT-L4 we observed a subtle
274 reduction of Retromer binding to SNX3-CI-MPR cargo-PtdIns3*P* liposomes, consistent with the slightly lower
275 affinity observed by ITC (**Fig. S7G**). In summary, peptides binding to Vps29 have a strong and specific impact
276 on a subset of Retromer-associated proteins including TBC1D5 and VARP, without affecting interactions that
277 occur near the Vps35-Vps26 interface (**Fig. 4I**). The stabilising RT-L4 peptide does not prevent binding of
278 any known ligands (**Fig. 4I**), which is an important property of a potential molecular chaperone, although it
279 does have subtle effects on these interactions depending on their respective binding sites.
280

281 ***RT-L4 reveals an unexpected autoinhibitory role for the C-terminal disordered tails of Vps26A and***
282 ***Vps26B***

283 During our analyses of RT-L4 we noted that it showed a lower binding affinity for the paralogous Vps26B-
284 $Vps35_{1-390}$ subcomplex when compared to Vps26A-$Vps35_{1-390}$ (**Fig. 5A; Table S2**). According to the sequence
285 alignment of Vps26, the residues responsible for Vps35 interaction are highly conserved (**Figs. S8A and S8B**),
286 while the extended C-terminal tails (residues 298 to 327 in Vps26A) are highly divergent apart from the
287 QRF/YE motif (**Fig 5B; Fig. S8A**). Strikingly when the disordered C-terminal domains of either Vps26A or
288 Vps26B are removed (Vps26AΔC and Vps26BΔC respectively) the binding affinity for RT-L4 is increased to
289 ~40 nM K_d and is now identical for both sub-complexes (**Fig. 5A**). We also find a similar improved affinity of
290 RT-L4 for *C. thermophilum* Retromer when the tail of Vps26 is removed (**Fig. S9**). This shows that the C-
291 terminal tails of Vps26A and Vps26B have an autoinhibitory effect on binding to RT-L4, with the Vps26B C-
292 terminus inhibiting the interaction more strongly.

Given that the RT-L4 peptide also subtly affects binding of Retromer to SNX3 and cargos, we were interested to determine whether the C-terminal tails of Vps26 might also influence SNX3 interactions. Intriguingly, SNX3 (in the presence of DMT1-II cargo) binds to Vps26AΔC-Vps35$_{1-390}$ with a significantly increased affinity compared to full-length Vps26A-Vps35$_{1-390}$ (**Fig. 5C; Table S7**). This suggests that there is a self-association of the C-terminal tail that weakens the SNX3-cargo interaction. Previous proteomics have shown that the C-terminal disordered sequences of human and mouse Vps26A and Vps26B can be phosphorylated, although the role of these post-translational modifications (PTMs) and their regulation has not been studied (*69*) (**Fig. 5B)**. We engineered a Vps26A variant with three phosphomimetic mutations in its C-terminal tail and tested the affinity of the Vps35$_{1-390}$/Vps26A phosphomimic complex for SNX3 in the presence of DMT1-II by ITC (**Fig. 5C**). Interestingly this mutant showed an enhanced affinity to the cargo-adaptor complex, although not to quite the extent of the complete removal of the Vps26A tail. Similar enhancement of binding to SNX3 cargo-adaptor complex was also observed when we mutated the conserved QRFE motif of Vps26A to polyalanine (**Figs. 5D and 5E**). Our data suggests that the tails of Vps26A and Vps26B play an unexpected autoinhibitory role in the interaction of Retromer with the SNX3 adaptor and associated cargos such as Dmt1-II and CI-MPR *in vitro*, and potentially phosphorylation of these tails could enhance SNX3-cargo interactions. The observation that Vps26B is more strongly autoinhibited than Vps26A might explain previous studies showing that the CI-MPR can only bind to Retromer containing Vps26B with the tail removed (*70*). However, this will require further studies of their interactions *in situ* to be confirmed.

Macrocyclic peptides as molecular probes to study Retromer mediated endosomal trafficking

With established mechanisms of binding *in vitro* we sought to assess the basic utility of these macrocyclic peptides as novel molecular tools for the study of Retromer. In the first instance we examined their use as fluorescent probes of Retromer localisation in cells (**Fig. 6**). As the peptides were not membrane permeable for cellular uptake we used a reversible cell permeabilization approach with the pore-forming bacterial toxin Streptolysin O (SLO) (*71*). After permeabilization cells were treated with FITC-labelled RT-D3 and RT-L4 and then processed for imaging and co-labelling with specific endosomal markers. In the absence of SLO permeabilization no intracellular fluorescence was detected for the FITC-labelled peptides indicating they are not crossing the membrane or being non-specifically internalised into the lumen of endosomal compartments (**Fig. 6A**). In permeabilised cells however, both FITC-labelled RT-D3 and RT-L4 were recruited to endosomal structures labelled with SNX1 (**Fig. 6A**). Using Airyscan super-resolution microscopy we found that the peptides also co-labelled endosomal structures marked with mCherry-tagged Vps35 (**Fig. 6B**). Lastly, we examined the impact of the peptides on the endosomal recruitment of TBC1D5, which has previously been shown to depend on interaction with Retromer (*40, 43, 44, 56, 72*). As expected, addition of unlabelled RT-L4 had no discernible effect on TBC1D5 localisation; however, RT-D3, which binds to the same site on Vps29 as TBC1D5, caused significant dispersal of TBC1D5 from endosomal structures (**Fig. 6C**). In orthogonal experiments we adapted an electroporation approach to deliver peptides to cells (*73*), and observed a similar inhibition of Retromer-dependent TBC1D5 localisation using electroporation (**Fig. S10**). Overall, our data

330 suggests that the Retromer-binding macrocyclic peptides are capable of acting as molecular probes for
331 Retromer localisation.
332
333
334

DISCUSSION

De novo macrocyclic peptides that target the Retromer endosomal trafficking complex

In this work the versatile RaPID screen was used to identify a series of potent Retromer-targeting macrocyclic peptides. These bind with high affinity and specificity to Retromer using two distinct evolutionarily conserved binding sites on either Vps29, or at the interface between Vps26 and Vps35. The cyclic peptides in the inhibitor sub-group (RT-D1, RT-D2, RT-D3, RT-L1 and RT-L2) reveal strong binding through the highly conserved surface groove of Vps29, lying on the opposite surface to that bound by the Vps35 subunit. Detailed structural analyses showed that these cyclic peptide inhibitors all form a β-hairpin configuration with a core Pro-Leu motif. These Vps29-binding cyclic peptides are effective at blocking association with TBC1D5, VARP and the bacterial hijacking molecule RidL, which are known to bind the same site using a similar β-hairpin structure (*40, 43, 44*). It is intriguing that all of the Vps29-binding peptides have been selected for the presence of this Pro-Leu dipeptide, and that this peptide has also evolved to mediate binding of endogenous ligands of the Retromer complex such as TBC1D5, VARP and RidL. The *de novo* macrocyclic peptide screening has therefore inadvertently identified an evolutionarily conserved binding mechanism, and interestingly previous screens of BET domain-binding peptides also uncovered sequence preferences that partly mimicked known endogenous ligands (*74*). Given that Vps29 is also a component of the Retriever complex, a Retromer-related assembly containing homologous subunits Vps35L and Vps26C (*75, 76*), these cyclic peptide inhibitors may also provide tools for studies of Retriever. However, known Retromer interactors such as TBC1D5 or VARP that depend on Vps29 for association have not been detected in Retriever interactomes (*75*), so whether the same binding site in Vps29 is accessible within the Retriever complex remains to be confirmed.

Among the identified macrocyclic peptides RT-L4 binds specifically to the interface between the N-terminal domain of Vps35 and the C-terminal sub-domain of Vps26 and is the sole molecule to show a significant ability to stabilise the Retromer complex. In the recent cryoEM structure of mammalian Retromer it was found that Vps26 and the N-terminal portion of Vps35 exhibit substantial flexibility compared with other regions of the complex (*61*). We speculate that the improved thermal stability of Retromer in the presence of RT-L4 may be partly due to reduced flexibility in these two subunits. Importantly, the RT-L4 peptide did not inhibit the binding of Retromer to its essential interacting partners including SNX27, Fam21, TBC1D5 and VARP, and in fact led to a general increase in their binding affinity *in vitro*. RT-L4 did have a minor effect however on binding of Retromer to SNX3 and ΩΦ[LV] motif-containing cargo, consistent with the fact that the RT-L4 binding site partially overlaps with the site where the N-terminal disordered domain of SNX3 engages Vps26 and Vps35 (*59*). Certainly, the impact of RT-L4 on the ability of the Retromer to form the membrane-associated arches with SNX3 and ΩΦ[LV] motif-containing cargo (*77*) will need to be tested.

Macrocyclic peptides as molecular tools for the study of Retromer function

The series of macrocyclic peptides discovered here provide novel molecular probes for the study of Retromer and endosomal trafficking. Firstly, using a simple reversible permeabilization approach, we have successfully

371 delivered the cyclic peptides RT-D3 and RT-L4 into cells and find they are specifically targeted to the
372 Retromer-positive endosomal structures. Thus, the peptides can be used to examine endogenous Retromer
373 localisation *in situ* and could feasibly be used to study Retromer in live cells or using super-resolution
374 approaches with different types of fluorescent dyes apart from the simple FITC labelling strategy used here.
375 The RT-D3 peptide also impacts recruitment of proteins such as TBC1D5 that depend on binding to the Vps29
376 subunit of the complex, and therefore could be used to probe the impact of acutely disrupting this interaction
377 in the future. In addition to studying the localisation of Retromer, the RT-L4 peptide provided a highly specific
378 substrate for purification of the Retromer complex from cells, and in the future could be useful for proteomic
379 studies of Retromer in diverse cells, tissues, and organisms. We also envisage that these peptides will provide
380 tools for enhancing Retromer stability for future structural studies of its interactions with accessory and
381 regulatory proteins by cryoEM and X-ray crystallography.
382 Our studies of the RT-L4 peptide binding to the Vps26–Vps35 interface revealed an autoinhibitory role
383 for the C-terminus of the Vps26A and Vps26B paralogues. Removal of their divergent C-terminal tails
384 significantly increased the affinity of both Retromer complexes for the RT-L4 peptide to similar levels, leading
385 us to then test the impact of the Vps26A and Vps26B tail domains on binding to the SNX3–DMT1-II cargo-
386 adaptor complex, a native ligand that engages Retromer at a similar location. Again, removal of the C-terminal
387 disordered domains significantly improved the affinity of Retromer for SNX3–DMT1-II, confirming their
388 autoinhibitory activity has a functional importance. Furthermore, this may be regulated by phosphorylation of
389 the Vps26A and Vps26B tails, as phosphomimetic mutants have a higher affinity for SNX3-DMT1-II than the
390 wild-type proteins. Since the discovery of the Vps26B paralogue of Vps26A it was clear that the most
391 significant difference between the two proteins was the sequence of their C-terminal domains (*78, 79*). Later
392 it was shown that Vps26A but not Vps26B Retromer bound to the SNX3-dependent cargo CI-MPR, however,
393 CI-MPR binding and trafficking by Vps26B was restored when its tail was deleted (*70*). Our data demonstrates
394 a direct role for both the Vps26A and Vps26B tails in negatively regulating the binding of SNX3-cargo *in*
395 *vitro*, with the Vps26B tail possessing a more potent autoinhibitory sequence than that of Vps26A. This
396 suggests that an activating switch such as phosphorylation of Vps26 proteins or binding of another regulatory
397 protein may promote the recruitment of SNX3-cargo complexes by Retromer in cells, although the specific
398 nature of this switch remains to be determined.
399
400 ***Towards therapeutic targeting of Retromer***
401 Endolysosomal trafficking and regulation of proteostasis is emerging as an attractive target in the treatment of
402 a range of diseases, including neurodegenerative disorders like AD and PD, infection by viral and bacterial
403 pathogens, and other diseases impacted by defective endosomal signalling such as cancer. There is an
404 increasing interest in developing molecules for both inhibition and enhancement of Retromer activity in these
405 processes (*11, 80, 81*). As shown previously, peptides that target Retromer and compete with the viral L2
406 protein can reduce HPV infection in cell and animal models (*38, 45, 82*), while a small molecule with Retromer
407 chaperoning activity can reduce cellular accumulation of toxic material causing neurodegeneration (*33, 46-51,*

408 *83-87*). However, these peptides and small molecules have only a relatively low affinity for Retromer, and
409 their specificities and pharmacological profiles are essentially unknown.

410 Because of their typically high affinity and larger surface area coverage, macrocyclic peptides are
411 emerging as an important class of molecules for the design of new drugs and molecular probes targeting
412 proteins and protein-protein interactions, often considered difficult using traditional small molecule
413 approaches (*54, 88-91*). The peptides we have discovered can be classified as either Retromer inhibitors or
414 stabilizers, and we provide a comprehensive biochemical and structural explanation for how each cyclic
415 peptide associates with Retromer and affects its native molecular interactions. The Retromer inhibitors we
416 identified were able to potently block TBC1D5, VARP and bacterial effector RidL binding, suggesting this
417 conserved site in Retromer is primed for targeting by peptide or small molecule-based inhibition. The
418 stabilising peptide RT-L4 enhanced Retromer association with known regulatory proteins. In particular, the
419 enhancement of binding between Retromer and Fam21 of the WASH complex by RT-L4 suggests the potential
420 use of RT-L4 to rescue the binding caused by the PD-linked Vps35 D620N mutant. The RT-L4 peptide has
421 much higher affinity and capacity to stabilise Retromer *in vitro* compared to the previously reported small
422 molecule chaperones R55 (*48*) and its derivative compound 2a (*20*). This highlights the potential of targeting
423 the Vps26 and Vps35 interface for the design of novel pharmacological chaperones of Retromer in future
424 studies. While the macrocyclic peptides described here are potential leads for therapeutic targeting of
425 Retromer, notable hurdles will include cell permeability, oral availability, and an ability to cross the blood
426 brain barrier when targeting neurological diseases. However, new approaches show promise in overcoming
427 these barriers, including the use of non-standard amino acids with novel activities and solubility profiles,
428 coupling to various cell-targeting peptides, and novel delivery methods (*91-94*). Alternatively, the peptides
429 discovered here could provide the basis for competitive screening for drug-like molecules that target the same
430 binding sites.

431 In summary, we have identified a series of Retromer-targeting macrocyclic peptides and demonstrate
432 their potential for Retromer inhibition and activation based on a comprehensive understanding of their different
433 mechanisms of action. They will be a valuable resource for the study of Retromer function at the cellular and
434 molecular level and represent promising leads for the targeting of Retromer in a variety of diseases caused by
435 dysregulation or disruption of the endosomal membrane trafficking system.

436

437

438 **MATERIALS AND METHODS**

439 *Chemicals and antibodies*

440 Rabbit polyclonal anti-TBC1D5 was purchased from Proteintech (17078-1-AP). Goat polyclonal TBC1D5
441 antibody was from Santa Cruz Biotechnology (sc-99661). Mouse monoclonal anti-SNX1 was purchased from
442 BD Transduction Laboratories (611483). Rabbit polyclonal Vps26A antibody was from Abcam (ab23892).
443 Mouse monoclonal anti–α-tubulin (clone DM1A; T9026) was purchased from Sigma-Aldrich. Goat polyclonal
444 anti-Vps35 (NB100-1397) was purchased from Novus Biologicals. Secondary donkey anti-mouse IgG Alexa
445 Fluor 647 (A31571), and donkey anti-rabbit IgG Alexa Fluor 555 (A31572) were purchased from Thermo
446 Fisher Scientific. The linear peptides DMT1-II$_{550-568}$ (AQPELYLLNTMDADSLVSR), CI-MPR$_{2347-2375}$ and
447 palmitoylated CI-MPR$_{2347-2375}$ with N-terminal di-lysine (KKSNVSYKYSKVNKEEETDENETEWLMEEIQ)
448 were synthesised by Genscript (USA).

449

450 *Molecular Biology and Cloning*

451 pmCherry-SNX1 was generated by subcloning the full-length open reading frame of human SNX1 from
452 pEGFP-SNX1 described previously (*95*), into the multiple cloning site of pmCherry-C1. pmCherry-Vps35
453 was generated by subcloning the full-length open reading frame of human Vps35 from pEGFP-Vps35
454 described previously (*10*), into the multiple cloning site of pmCherry-N1.

455 For bacterial expression, Retromer constructs encoding full-length human and zebrafish Vps29,
456 Vps26A and Vps35 were cloned into either pET28a and pGEX4T-2 vectors as described previously (*60, 96*).
457 *Chaetomium thermophilum* Vps29, Vps26 and Vps35 were also cloned using protocol described previously
458 (*58*). In all cases, Vps26A was cloned as a N-terminal His$_6$-tag fusion protein and Vps29 was cloned into
459 pGEX4T-2 vector as a cleavable N-terminal GST fusion protein. For mouse Vps26B, full-length cDNA was
460 inserted into pMW172Kan vector (*78*). For the truncation constructs, the DNA sequence encoding the N-
461 terminal part of Vps35 (Vps35$_{1-172}$, Vps35$_{1-224}$ and Vps35$_{1-390}$) was cloned into pGEX4T-2 vector. Vps26 ΔC-
462 term. tail (ΔC) constructs (Vps26A$_{9-298}$ and Vps26B$_{7-296}$) were cloned into pET28a vector containing His$_6$-tag.
463 Full-length Vps26A pm mutant (substituted S315E, S318E and S321E), Vps26A$_{QRFE-AAAA}$ (substituted residues
464 311 - 314 to alanine) and Vps26B pm mutant (S302E, S304E, S311E, S319E, T325E, S327E, and S330E
465 substitution) were synthetic genes by Genscript (USA). cDNA encoding full-length human SNX3 was cloned
466 into pGEX4T-2 vector. Similarly, the cDNA encoding the human Fam21 LFa motif repeats 19 to 21 was
467 cloned into pGEX4T-2 vector. The TBC domain of human TBC1D5 was cloned into the pMCSG9 vector
468 containing a N-terminal GST and a TEV cleavage site. Full-length mouse SNX27 was cloned into the
469 pMCSG7 vector containing a N-terminal His and a TEV cleavage site (*97*). PDZ domain of mouse SNX27
470 was cloned into the pGEX4T2 vector similar to the one described previously (*98*). cDNA encoding *L.*
471 *pneumophila* effector RidL residues 1 to 236 was also cloned into the pGEX4T2 vector. Full-length human

472 Rab7a was cloned into pET28a vector. Site-directed mutagenesis was performed to generate mutant constructs
473 with custom-designed primers. All constructs were verified using DNA sequencing.
474
475 *RaPID screening*
476 For the first round of RAPID selection, an mRNA library was generated by T7 polymerase mediated *in vitro*
477 transcription of a PCR assembled DNA template, purified by PAGE, and covalently ligated to a puromycin
478 linked oligonucleotide with T4 RNA ligase. 1.2 μM puro-linked mRNA library was translated in a 150 μL *in*
479 *vitro* translation reaction (genetically reprogrammed to incorporate L- or D- ClAC-Tyr in place of the initiator
480 formyl-methionine) at 37°C for 30 min. Peptide-mRNA fusion molecules were released from the ribosome by
481 treatment with 17 mM EDTA for 30 min. at 37°C, reverse transcribed using MMLV reverse transcriptase (H-
482)(Promega) at 42°C for 1 hour and buffer exchanged to TBS-T using sephadex G-25. The resulting cyclic
483 peptide-mRNA:cDNA library was counter-selected 3 times against His Pull-Down Dynabeads (Thermo
484 Fisher), and affinity selected against 200 nM bead-immobilised Retromer for 30 min. at 4°C, with the beads
485 washed 3 times with TBS-T, overlaid with 0.1% triton-X100 and heated to 95°C to elute the cDNA for
486 recovery by PCR.
487 For the second and subsequent rounds of selection, the translation reaction was scaled down to 2.5 μL
488 total volume, and 6 iterative counter-selections using uncoated beads were conducted prior to affinity selection
489 against Retromer. Following 5 iterative rounds of selection, Retromer ligands were identified by sequencing
490 the final enriched cDNA using a MiSeq sequencer (Illumina).
491
492 *Synthesis of Cyclic Peptides*
493 Untagged peptides were synthesized at 25 μM scale on NovaPEG Rink Amide resin (0.53 mmol/g) using
494 Fmoc-based chemistry on a Syro I peptide synthesizer (Biotage). Fmoc-protected amino acid (6 eq.), (2-(1H-
495 benzotriazol-1-yl)-1,1,3,3-tetramethyluronium hexafluorophosphate (HBTU, 6 eq.), hydroxybenzotriazole
496 (HOBt, 6 eq.) and disopropylethylamine (DIPEA, 12 eq.) with 30 min coupling cycles. Deprotection of fmoc
497 was achieved with 40% piperidine/DMF for 1 × 3 min. then 1 x 12 min. Chloroacetic acid was coupled
498 manually after the final deprotection using the same conditions.
499 Linear peptides were cleaved from resin with TFA/TIS/H_2O/EDT (92.5:2.5:2.5:2.5) over 2 h. Crude
500 peptides were precipitated and washed (5x cold Et_2O), redissolved in DMSO, and cyclized by adding DIPEA
501 until basic followed by incubating at room temperature. Cyclic peptides were acidified, diluted to 50% DMSO
502 with water and purified by RP-HPLC using a Chromolith C18 column with a gradient of 10 to 70% buffer B
503 (99.9% CH_3CN/0.1% TFA in buffer A, 0.1% TFA in water) over 40 min and lyophilized, before the TFA salt
504 was exchanged to HCl by triplicate lyophilization from 5 mM HCl aq.
505
506 *Synthesis of biotinylated and FITC labelled cyclic peptides*

Biotin and FITC labelled peptides were synthesized (100 μM scale) on Rink Amide MBHA resin (0.6 mmol/g) using Fmoc-based chemistry and a peptide synthesizer (Symphony, Protein Technologies) Fmoc -Lys(Mtt)-OH in position 1. Fmoc-protected amino acid (4 eq.), 2-(6-chloro-1H-benzotriazole-1-yl)-1,1,3,3 tetramethylaminium hexafluorophosphate (HCTU, 4 eq.), and disopropylethylamine (DIPEA, 4 eq.) were used in 2 × 30 min coupling cycles. Fmoc deprotection was achieved by treatment with 1:2 piperidine/DMF for 2 × 3 min. Chloroacetic acid was coupled manually after the final deprotection using chloroacetic acid (4 eq.) and HATU (4 eq.), and DIPEA (4 eq.) in N,N-dimethylformamide (DMF). Selective side-chain deprotection of the methyl trityl (Mtt) group on lysine was achieved using 3% TFA in dichloromethane (DCM) (5 × 2 min). Biotin was coupled using biotin 2-(1H-7-azabenzotriazol-1-yl)-1,1,3,3-tetramethyl uraniumhexafluorophosphate methanaminium (HATU, 2 eq.) and DIPEA in DMF. FITC was coupled using FITC (2 eq.) and DIPEA.

Linear peptides were cleaved from the resin by treatment with TFA/TIS/H_2O (95:2.5:2.5) for 2 h. The crude peptides were precipitated and washed with cold Et_2O, redissolved in 50% acetonitrile/0.05% TFA in water, and lyophilized. Peptides were purified by RP-HPLC using a Phenomenex Luna C18 column eluting at a flow rate of 20 mL/min and a gradient of 20 to 70% buffer B (90% CH_3CN/10% H_2O/0.1% TFA in buffer A, 0.1% TFA in water) over 30 min and lyophilized.

Cyclization to form the thioether was achieved by dissolving the linear peptide in DMF with DIPEA (10 eq.) and the reaction monitored by UP-LCMS. After no more linear peptide was detected, DMF was removed *in vacuo* and the cyclic peptide purified by RP-HPLC using a Phenomenex Luna C18 column eluting at a flow rate of 20 mL/min and a gradient of 20 to 70% buffer B (90% CH_3CN/10% H_2O/0.1% TFA in buffer A, 0.1% TFA in water) over 30 min and lyophilized.

Peptides were characterised and purity determined by analytical RP-UPLC and UPLC-MS methods. UPLC was performed on Shimadzu Nexre UPLC with PDA using an AgilentEclipse plus C18RRHD 1.8 μm, 2.1´100 mm UPLC Column., and a gradient of 0 to 80% buffer B (90% CH_3CN/10% H_2O/0.1% TFA in buffer A, 0.1% TFA in water) over 6 min. UPLC-MS was performed on Shimadzu Nexre UPLC system connected to LCMS-2020 single quadrupole mass spectrometer using an phenomonex Aeris Peptide 1.7 μm XB-C18 column 50 x 2.1 mm and a gradient of 0 to 80% buffer B (90% CH_3CN/10% H_2O/0.1% formic acid in buffer A, 0.1% formic acid in water) over 6 min.

Cell culture and transfection

HeLa cells (ATCC CCL-2) were maintained in high glucose Dulbecco's Modified Eagle Medium (DMEM; Thermo Fisher Scientific) supplemented with 10% fetal bovine serum (FBS) and 2 mM L-glutamine (Thermo Fisher Scientific) in a humidified 37 °C incubator with 5% CO_2. Transfection was performed using Lipofectamine 2000 (Thermo Fisher Scientific) according to the manufacturer's instructions.

542 *Peptide delivery by reversible permeabilization and and indirect fluorescence microscopy and image*
543 *analysis*

544 Reversible permeabilization of HeLa cells with Streptolysin O (SLO; 25,000 - 50,000 U; Sigma-Aldrich) was
545 performed as previously described (*99*). In brief, an aliquot of SLO stock was reduced by 10 mM DTT (Sigma
546 Aldrich) for 20 min at 37°C, then diluted to working concentration (200x) in DPBS containing 1 mM $MgCl_2$.
547 HeLa cells grown on coverslips were incubated in the SLO containing solution for 9 min at 37°C, washed
548 twice with DPBS containing 1 mM $MgCl_2$, then incubated with ice-cold transport buffer (140 mM NaCl, 5
549 mM KCl, 1 mM $MgCl_2$, 10 mM HEPES, 10 mM glucose, pH 7.4) containing fluorescent peptides (5 µg/ml)
550 on ice for 5 min. After labeling, the cells were washed with ice-cold transport buffer twice and incubated with
551 the recovery medium (DMEM, 10% FBS, 1.8 mM $CaCl_2$, without antibiotics) for 20 min at 37 °C. Cells were
552 fixed with 4% PFA or ice-cold methanol and subjected for microscopy analysis.

553 HeLa cells grown on coverslips were routinely fixed and permeabilized in ice-cold methanol for 5 min
554 at −20°C, unless otherwise cited. After blocking with 2% BSA in PBS for 30 min, cells were labeled with anti-
555 TBC1D5 (1:200) and anti-SNX1 (1:100) for 1 h at room temperature followed by the incubation with
556 AlexaFluor555 and AlexaFluor647 conjugated secondary antibodies. Coverslips were mounted on glass
557 microscope slides using Fluorescent Mounting Medium (Dako), and the images were taken at room
558 temperature using the Leica DMi8 SP8 inverted confocal equipped with 63x Plan Apochromatic objectives or
559 the Zeiss LSM880 Axiovert 200 inverted confocal with AiryScan FAST detector equipped with 63x Plan
560 Apochromatic objectives. For quantification, images were taken from multiple random positions for each
561 sample.

562 Images were processed using ImageJ software. Colocalization analysis was performed as described
563 previously (*100*). In brief, single cells were segregated from fields of view by generating regions of interest,
564 cropped, split into separated channels, and applied for threshold processing. Colocalization analysis was
565 conducted on three independent experiments and represented as Pearson's correlation coefficient.
566 Colocalization values were exported to R studio and tabulated accordingly.

567

568 *Peptide electroporation and indirect fluorescence microscopy and image analysis*

569 Peptide electroporation was performed on the Neon Transfection System from Thermo Fisher Scientific
570 according to manufactor's instructions, adapting the protein electroporation strategy of Alex et al., (2018) (*73*).
571 In brief, aliquots of 3 x 10^5 HeLa cells were pelleted and resuspended in 10 µl of the electroporation Buffer R
572 (Thermo Fisher Scientific). The RT-D3 peptide or a scrambled RT-D3 control peptide were then mixed with
573 cell suspensions to reach the final concentrations of 20 µM, while cell suspensions alone served as mock
574 controls. The peptide/cell suspension mixtures were loaded with 10 µl Neon Pipette Tips (Thermo Fisher
575 Scientific) and electroporated with two pulses at 1000 V for 35 ms. Electroporated cells were then transferred

576 onto poly-L-lysine-coated glass coverslips in a 12-well plate containing the complete DMEM medium to allow
577 the recovery for 16 – 18 h.

578 Cells grown on coverslips were fixed with 4% PFA in PBS for 15 min followed by permeablisation
579 and blocking with 0.1% saponin in 2% BSA/PBS for 20 min. Cells were then labelled with the diluted goat
580 polyclonal TBC1D5 antibody (1:100) and rabbit polyclonal Vps26A antibody (1:500) in 0.1% saponin
581 followed by the corresponding fluorescently-conjugated secondary antibodies for 1 h at room temperature.
582 Coverslips were mounted on glass microscope slides using the Fluorescence Mounting Medium (DAKO), and
583 the images were taken using a Leica DMi8 SP8 inverted confocal microscope equipped a 63x Plan
584 Apochromatic 1.4 NA oil objective. Images were processed using Fiji/Image J software and the co-localization
585 analysis was performed using the Fiji/Image J EzColocalization plugin. In brief, ~ 60 individual cells for each
586 condition were randomly selected and cropped to generate and record regions of interest (ROI). The selected
587 ROI was then split into the separate channels and threshold applied before co-localization analysis by Pearson's
588 correlation coefficient. Statistical analysis and graph generation were performed using Prism9 (GraphPad)
589 software. Error bars on the graphs represent ± SEM. All p values were calculated using a Student's t test and
590 $p < 0.05$ was considered as statistically significant.

591

592 *Recombinant Protein Expression and Purification*

593 All the Retromer constructs were expressed using BL21 Star^{TM} (DE3) cells and induced by the addition of
594 IPTG to a final concentration of 1 mM at an OD_{600} of ~ 0.8. The temperature was then reduced to 18°C and
595 incubated overnight. To obtain the Retromer trimer complex (including human, zebrafish and *Chaetomium*
596 *thermophilum*), full-length GST-tagged Vps29 co-expressed with Vps35 was mixed with cell pellet of Vps26A
597 and lysed through a Constant System TS-Series cell disruptor in lysis buffer containing 50 mM HEPES pH
598 7.5, 200 mM NaCl, 5% glycerol, 50 µg/ml benzamidine and DNase I. The homogenate was cleared by
599 centrifugation and loaded onto Talon® resin (Clonetech) for purification. To obtain the correct stoichiometry
600 ratio of the Retromer complex, the purified elution from Talon® resin was further passed through the
601 glutathione sepharose (GE healthcare). Removal of the GST-tag from human and zebrafish Vps29 was
602 performed using on-column cleavage with thrombin (Sigma-Aldrich) overnight at 4°C. For *Chaetomium*
603 *thermophilum* Vps29, the GST-tag was cleaved using PreScission protease overnight at 4°C. The flow-through
604 containing Retromer complex with GST-tag removed was further purified using size-exclusion
605 chromatography (SEC) on a Superdex200 column equilibrated with a buffer containing 50 mM HEPES pH
606 7.5, 200 mM NaCl, 5% glycerol and 0.5 mM TCEP. Production of Retromer individual subunits (Vps29,
607 Vps26A and Vps35) and subcomplexes (Vps29 - Vps35, Vps26A - $Vps35_{1-172}$, Vps26A - $Vps35_{1-224}$, Vps26A
608 - $Vps35_{1-390,}$ $Vps26A_{\Delta C\text{-term. tail}}$ - $Vps35_{1-390}$, $Vps26A_{pm}$ - $Vps35_{1-390}$, $Vps26A_{QRFE\text{-}AAAA}$ - $Vps35_{1-390}$, Vps26B -
609 $Vps35_{1-390}$, $Vps26B_{\Delta C\text{-term. tail}}$ - $Vps35_{1-390}$, and $Vps26B_{pm}$ - $Vps35_{1-390}$) were expressed and purified under the
610 same method. In brief, glutathione sepharose was used for Vps29, Vps35 and subcomplexes purification, and
611 Talon® resin was applied for Vps26A.

612 Expression and purification of GST-SNX3, GST-Fam21$_{R19-R21}$, GST-TBC1D5$_{TBC}$, GST-SNX27$_{PDZ}$,
613 His-SNX27, GST-RidL$_{1-236}$ and His-Rab7a were performed using similar methods as described previously (*56,*
614 *59, 97, 98*). Cell pellets were lysed by Constant System TS-Series cell disruptor using the same buffer as
615 Retromer. All proteins were passed through either Talon® resin or Glutathione sepharose depending on the
616 affinity tag. Removal of fusion tag was performed on-column overnight using either thrombin for SNX3 and
617 RidL$_{1-236}$, and TEV protease for SNX27$_{PDZ}$ and TBC1D5$_{TBC}$. The flow-through samples containing GST-tag
618 removed SNX3, RidL$_{1-236}$, TBC1D5$_{TBC}$ and SNX27$_{PDZ}$ were further purified using SEC in the same way as
619 Retromer. For, His-tagged SNX27 and His-Rab7a, the fractions eluted from Talon® resin was further purified
620 SEC directly using the same buffer as described above. Similarly, the GST-tagged Fam21$_{R19-R21}$ eluted from
621 Glutathione sepharose was directly injected into SEC for final purification.
622 Retromer 3KE construct design, expression, and purification has previously been described (*61*).
623 Briefly, Retromer plasmids were co-transformed into BL21(DE3) Rosetta2 pLysS cells (Millipore). Cells were
624 grown to OD_{600} between 0.8-1.0 and induced for 16-20 hours at 20°C with 0.4 mM IPTG. Cells were lysed by
625 a disruptor (Constant Systems Limited). Protein was purified in 10 mM Tris-HCl (pH 8.0), 200 mM NaCl, 2
626 mM βME using glutathione sepharose (GE Healthcare). Protein was cleaved overnight using thrombin
627 (Recothrom, The Medicines Company) at room temperature and batch eluted in buffer. Retromer was further
628 purified by gel filtration on a Superdex S200 10/300 column (GE Healthcare) into 10 mM Tris-HCl (pH 8.0),
629 200 mM NaCl.
630
631 *Biotinylated Cyclic Peptides Pull-down Assay*
632 Culture dishes (15 cm) with HeLa cells at approximately 90% confluency were washed with PBS and lyzed
633 by the lysis buffer containing 50 mM HEPES pH 7.5, 200 mM NaCl, 1% Triton, 25 µg/ml DNase I and one
634 protease-inhibitor cocktail tablet per 50 ml lysis buffer. Soluble and insoluble fractions were separated by
635 centrifugation at 13,000 *g* for 20 min at 4°C. After centrifugation, supernatant was then added to the
636 streptavidin agarose (Thermo Scientific) pre-incubated with 140 µM of either biotinylated RT-D3 or
637 biotinylated RT-L4 cyclic peptides for 2 h at 4°C. Both cyclic peptides were carefully prepared without
638 forming precipitation before mixing with streptavidin agarose.
639 In the case of capturing SNX3, roughly 5 µM of DMT1-II$_{550-568}$ peptide was added to the supernatant
640 prior mixing with the streptavidin agarose. Beads were then spun down at 2,000 g for 2 min and washed five
641 times with washing buffer containing 50 mM HEPES pH 7.5, 200 mM NaCl, 5% glycerol, 0.05% triton X-
642 100 and 0.5 mM TCEP. Bound complex was eluted from the streptavidin agarose by boiling in 100 mM DTT
643 added SDS loading buffer (Life Science) and subjected to SDS-PAGE analysis and western blotting.
644
645 *RT-L4 Binding Site Screening Assay*
646 Mapping the potential binding region of RT-L4 was carried out using purified Vps26A, Vps35$_{1-390}$, Vps26-
647 Vps35$_{1-390}$ subcomplex and the associated mutants. First, 10 µM of purified proteins were incubated with fresh

648 streptavidin agarose containing either 100 μM of RT-L4 or equivalent percentage (v/v) of DMSO. The mixture
649 was incubated in binding buffer containing 50 mM HEPES pH 7.5, 200 mM NaCl, 5% glycerol, 0.5 mM TCEP
650 for 30 min at 4°C. Beads were then washed three times with binding buffers followed by SDS-PAGE analysis.
651
652 *GST Pull-down Assay*
653 GST pull-down assay was carried out using either GST-tagged Retromer, GST-Fam21$_{R19-R21}$, or GST-
654 TBC1D5$_{TBC}$ as bait protein. For pull-down assays containing either SNX27 or SNX3 + DMT1-II$_{550-568}$ peptide,
655 GST-tagged Retromer and GST alone were first incubated with fresh glutathione sepharose bead for 2 hours
656 at 4°C. To avoid precipitation caused by cyclic peptides, SNX3/SNX27 - cyclic peptides mixture were
657 centrifuged at 17,000 rpm for 20 min at 4°C before added into the glutathione sepharose bead samples. The
658 reaction mixtures were incubated for at least 4 hours in binding buffer containing 50 mM HEPES pH 7.5, 200
659 mM NaCl, 5% glycerol, 0.1% triton X-100 and 0.5 mM TCEP. Beads were then washed four times with
660 binding buffers and samples of beads were analyzed by SDS-PAGE. Retromer - TBC1D5 and Retromer –
661 Fam21 pull-down assay were performed using identical protocol as described above. For Retromer - TBC1D5
662 pull-down assay, GST-TBC1D5$_{TBC}$ was used in order to differentiate GST-Vps29 and TBC1D5$_{TBC}$ on the SDS-
663 PAGE.
664
665 *Crystallization and Data Collection*
666 Crystallization screening was performed using hanging drop vapour diffusion method under 96-well format at
667 20°C. To co-crystallize Vps29 with cyclic peptides, a 1.5-fold molar excess of the RT-D1, RT-D2, RT-D3,
668 RT-L1 and RT-L2 peptides were added separately to the purified hVps29 to a final concentration of 14 mg/ml.
669 Initial crystals were obtained in hVps29 - RT-D1, hVps29 - RT-D2 and hVps29 - RT-L2 complex samples.
670 For hVps29 - RT-D1, plate shape crystals were observed in many different commercial screen conditions, but
671 the best quality crystals were obtained in a condition comprising 3.5 M sodium formate. For hVps29 – RT-
672 D2, the optimized crystals were obtained by streak-seeding crystals grown in 0.1 M potassium thiocyanate,
673 30% PEG 2000 MME into the same condition prepared with protein at 8 mg/ml. For hVps29 – RT-L2 sample,
674 precipitation was observed after the addition of the cyclic peptide. Precipitation was removed by centrifugation
675 and diamond shape crystals were obtained after overnight incubation in condition consisted of 0.1 M HEPES
676 pH 7.0, 1 M succinic and 1% PEG2000 MME. Initial attempts to co-crystallize hVps29 – RT-D3 and hVps29
677 – RT-L1 were unsuccessful. For hVps29 – RT-L1, small long needle shape crystals were observed in condition
678 consisted of 1.4 M sodium malonate pH 6.0 using 26 mg/ml protein with 1.5 fold molar excess of RT-L1 and
679 10 fold molar excess of 18-crown-6. Diffraction quality crystals were obtained by streak-seeding crystals
680 grown in the 26 mg/ml into the same condition prepared with protein at 15.5 mg/ml. To grow crystals
681 containing RT-D3, we substituted hVps29 to ctVps29, and managed to obtain diffraction quality crystals in
682 condition consisted of 0.18 M ammonium citrate dibasic and 20% PEG 3350 using 14 mg/ml protein with 2-
683 fold molar excess RT-D3. Prior to data collection, all the crystals were soaked in the appropriate cryoprotectant

684 solutions. X-ray diffraction data were measured on the MX1 and MX2 beamlines at the Australian Synchrotron
685 at 100 K.
686
687 *Crystal Structure Determination*
688 All the data collected were indexed and integrated by AutoXDS (*101*) and scaled using Aimless (*102*). Crystal
689 structures of hVps29 - RT-D1, hVps29 - RT-D2, ctVps29 - RT-D3, hVps29 - RT-L1 and hVps29 - RT-L2
690 were solved by molecular replacement using Phaser (*103*) with native hVps29 crystal structure (PDB ID:
691 1W24) as the initial model. The initial electron density map obtained from the best solution guided the
692 locations of the cyclic peptides and 18-crown-6. Structure refinement was performed using the PHENIX suite
693 (*104*) with iterative rebuilding of the model. The refined model was manually rebuilded using Coot guided by
694 F_o - F_c difference maps. Coordinates for D-tyrosine and sulfanylacetic acid linking N-terminal and C-terminal
695 of the peptides were generated using LIBCHECK from Coot. The quality and geometry of the refined
696 structures were evaluated using MolProbity (*105*). Data collection and refinement statistics are summarized in
697 **Table S3**. Sequence conservation was based on a *T-Coffee* multiple sequence alignment (*106*) and calculated
698 using the ConSurf Server (*107*). Structure comparison was analysed using DALI (*108*) and molecular figures
699 were generated using PyMOL.
700
701 *Surface Plasmon Resonance*
702 SPR experiments were conducted at room temperature using a Biacore T-200 instrument (Cytiva) in HBS-P+
703 buffer (10 mM HEPES, 150 mM NaCl, 0.05 % (v/v) surfactant P20, pH 7.4) containing 0.1% (v/v) DMSO.
704 100 nM human or zebrafish Retromer was immobilized on a Ni^{2+}-primed Series S Sensor Chip NTA (Cytiva)
705 following the manufacturer's instructions. A single cycle kinetics protocol involving five 120 s injections of
706 peptide as analyte at a flow rate 60 $\mu L.min^{-1}$ was employed, with kinetics determined using a 1:1 binding
707 model.
708
709 *Isothermal Titration Calorimetry*
710 ITC experiments were conducted at 25°C using a Microcal PEAQ ITC (Malvern) in buffer containing 50 mM
711 HEPES pH 7.4, 200 mM NaCl, 5% glycerol, 0.5 mM TCEP. Cyclic peptides in the range of 120 μM to 300
712 μM were titrated into 6 – 20 μM of Retromer, subcomplexes or individual subunits. The interaction of
713 Retromer and $TBC1D5_{TBC}$ in the presence of cyclic peptide was carried out by titrating 80 μM of $TBC1D5_{TBC}$
714 into 6 μM of Retromer + 30 μM of either RT-D3 or RT-L4. In the native control, the cyclic peptide was
715 substituted with equivalent percentage (v/v) of DMSO. Under the same experimental condition, 180 μM of
716 $RidL_{1-236}$ was titrated into 9 μM of Retromer with 72 μM of RT-D3 or equivalent percentage (v/v) of DMSO.
717 Similarly, the effect of the cyclic peptides on the interaction of Retromer and $SNX27_{PDZ}$ was performed by
718 titrating 1.3 mM of $SNX27_{PDZ}$ into 30 μM of Retromer + 150 μM of either RT-D3 or RT-L4. The interaction
719 of Retromer and Fam21 was performed by titrating 300 μM of GST-$Fam21_{R19-R21}$ into 12 μM of Retromer +
720 60 μM of either RT-D3 or RT-L4. In the case of SNX3, 1.2 mM SNX3 was titrated into 12 μM of Retromer +

721 180 μM DMT1-II$_{550-568}$ peptide + 60 μM of either RT-D3 or RT-L4. Similarly, 1.2 mM SNX3 was titrated into
722 12 μM of Retromer + 180 μM CIMPR$_{2347-2376}$ peptide to examine its effect on Retromer and SNX3 interaction.
723 To ensure that RT-L4 binds specifically only to Retromer but not the accessory proteins, 90 μM of RT-L4 was
724 titrated into 7 μM Retromer, TBC1D5$_{TBC}$, SNX3 or SNX27 using buffer described above. The effect of Vps26
725 C-terminal disordered tail on RT-L4 and SNX3 binding was first performed by titrating 90 μM of RT-L4 into
726 8 μM of Vps26A/B - Vps35$_{1-390}$, or Vps26A/B$_{\Delta C\text{-term. tail}}$ - Vps35$_{1-390}$ subcomplexes. In the case of SNX3
727 binding, 970 μM of SNX3 was titrated into 17 μM of FL, pm mutant, QRFE-AAAA or ΔC Vps26A/B - Vps35$_{1-}$
728 $_{390}$ subcomplexes with and without 255 μM DMT1-II$_{550-568}$ peptide. For the Retromer, R55 and compound 2a
729 interactions, 120 μM - 540 μM of freshly prepared R55 or compound 2a was titrated into 9 μM – 16 μM of
730 Retromer using the same buffer as the cyclic peptide ITC experiments.
731 In all cases, the experiments were performed with an initial 0.4 μl (not used in data processing)
732 followed by 12 serial injections of 3.22 μl each with 180 sec intervals. Data were analyzed with Malvern
733 software package by fitting and normalized data to a single-site binding model, yielding the thermodynamic
734 parameters K_d, ΔH, ΔG and -TΔS for all binding experiments. The stoichiometry was refined initially, and if
735 the value was close to 1, then N was set to exactly 1.0 for calculation. All experiments were performed at least
736 in triplicate to check for reproducibility of the data.
737
738 *Differential Scanning Fluorimetry*
739 Thermal unfolding experiments were carried out through preferential binding of a fluorophore to unfolded
740 protein using a ViiA7 real-time PCR instrument (Applied Biosystems). In brief, 0.4 mg/ml of freshly purified
741 Retromer, subcomplex and individual subunits was pre-incubated with 20 - 60 molar excess of cyclic peptides,
742 R55 or compound 2a for at least 30 min on ice followed by centrifugation at 17,000 rpm for 20 min at 4°C to
743 remove all possible precipitation. To measure thermal denaturation, freshly prepared SYPRO orange dye (Life
744 Science) was then added to protein-cyclic peptide complex mixture to a final concentration of 5X before loaded
745 into the 96-well plate. Relative fluorescence units (R.F.U.) were measured from 25°C to 90°C using the ROX
746 dye calibration setting at 1°C increments. Experiments were performed with four replicates and T_m was
747 calculated using Boltzmann sigmoidal in Prism version 8.0.1 (GraphPad software).
748
749 *Mass Photometry*
750 Molecular mass measurement of Retromer in the presence of cyclic peptide was performed using Refeyn
751 OneMP mass photometer (Refeyn Ltd). In brief, 10 μl of standard buffer containing 50 mM HEPES pH 7.5,
752 200 mM NaCl was applied. Next, 1 μl of 50 nM Retromer + RT-D3 & RT-L4 cyclic peptide was added to the
753 drop to a final concentration of 5 nM and 10000 frames were recorded. Calibration was performed using three
754 protein standards (i.e. 66, 146 and 480 kDa) (ThermoFisher Scientific).
755
756 *GTPase activity assay*

757 The Rab7 GAP activity of TBC1D5 in the presence of Retromer and cyclic peptides was carried out using the
758 GTPase-Glo™ assay kit (Promega) according to the manufacturer's instructions. Briefly, 10 μM of Rab7a
759 containing 10 μM GTP, 1 mM DTT in GTPase/GAP buffer was incubated with 3 μM $TBC1D5_{TBC}$, 6 μM
760 Retromer and 60 μM of cyclic peptides or equivalent percentage (v/v) of DMSO for 60 min at room
761 temperature. For the Rab7a only experiment, 10 μM Rab7a was incubated with 60 μM of cyclic peptides
762 without $TBC1D5_{TBC}$ or Retromer. Similarily, $TBC1D5_{TBC}$ only experiments was performed by incubating 10
763 μM of Rab7a with 3 μM $TBC1D5_{TBC}$ and 60 μM of cyclic peptides witout Retromer. Opposite reactions were
764 also prepared for Retromer only experiments. To complete the GTPase reaction, an equal volume of the
765 reconstituted GTPase-Glo™ reagent containing 5 μM ADP was then added to the reaction mix and incubated
766 for a further 30 min at room temperature. The luminescence of residual GTP after GTPase reaction was
767 measured by adding detection reagent to the reaction mix and recorded using infinite® M1000 PRO multimode
768 microplate reader (TECAN) at 25°C.
769
770 *Cryo-EM Grid Preparation and Data Collection*
771 For cryo-electron microscopy of Retromer+RT-L4, Retromer 3KE at a final concentration of 0.5 mM in 20
772 mM Tris pH 8.0 / 100 mM NaCl / 2 mM DTT was combined with RT-L4 at a final concentration of 0.1 mM,
773 incubated for 1 hour, and spun briefly in a tabletop centrifuge. 2 μl of the sample was applied to freshly glow
774 discharged Quantifoil 1.2/1.3 300 mesh grids, and the grids were vitrified in liquid ethane using a
775 ThermoFisher Mark IV Vitrobot, using a 3.5 second blot time at 100% humidity and 20°C. 4791 micrographs
776 were collected on a ThermoFisher FEI Titan Krios G3i microscope in the Center for Structural Biology's Cryo-
777 EM Facility at Vanderbilt. The microscope operated at 300 keV and was equipped with a ThermoFisher
778 Falcon3 direct electron detector camera. The nominal magnification used during data collection was 120,000x,
779 and the pixel size was 0.6811 Å/pix. The total electron dose was 50 e^-/A^2, and micrographs were collected at
780 +/-30° tilts. Data collection was accomplished using EPU (ThermoFisher).
781
782 For cryo-electron microscopy of *apo* Retromer, 2 μl WT Retromer at a concentration of 0.5 mM in 20 mM
783 Tris pH 8.0 / 100 mM NaCl / 2 mM DTT was applied to freshly glow discharged Quantifoil 1.2/1.3 300 mesh
784 grids, and the grids were vitrified in liquid ethane using a ThermoFisher Mark IV Vitrobot, using a 2s blot
785 time at 100% humidity and 8°C. 891 micrographs were collected on a ThermoFisher FEI Titan Krios
786 microscope at the National Resource for Automated Molecular Microscopy (NRAMM). The microscope
787 operated at 300 keV and was equipped with a Gatan BioQuantum energy filter with a slit width of 20eV and
788 a Gatan K2 Summit direct electron detector camera. The nominal magnification used during data collection
789 was 105,000x, and the pixel size was 1.0691 Å/pix. The total electron dose was 73.92e^-/A^2, and micrographs
790 were collected at +/-15° tilts. Data collection was accomplished using Leginon (*109*)
791
792 *Single Particle Cryo-EM Image & Data Processing*

All images were motion corrected using MotionCor2 (Zheng et al., 2017). Micrographs from the *apo* Retromer data collection were rescaled to match the 1.096Å/pix pixel size from published data collections (*61*) using an NRAMM script written for MotionCor2. The CTF of each micrograph was determined using Gctf (*110*). Defocus values for the Retromer/RT-L4 data varied between -0.8 and -2.6 µm; defocus values for the *apo* Retromer data varied between -0.8 and -4.7 µm. RELION-3 (*111*) was used for all image processing unless otherwise indicated.

Retromer/RT-L4 processing. Micrographs were autopicked using a 20Å low-pass filtered 3D model that had been produced in early rounds of processing, and this template-based autopicking identified 968,806 particles. Multiple rounds of 2D classification yielded 171,270 particles suitable to continue to 3D classification. The same 3D model used for autopicking was filtered to 60Å and used as an initial model for 3D classification. The particles underwent multiple rounds of CTF refinement and Bayesian polishing to produce a final set of 28,083 particles suitable for 3D refinement and postprocessing. The final masked model had a resolution of 5.9Å and a Relion-determined B-factor of -88.

Apo Retromer processing. Data giving rise to the published Retromer *apo* reconstruction lacked tilted views (**Table S5**); an additional data set (**Table S5**; data collection #3) was collected to add tilted views and to improve the reconstruction for this study. Several thousand particles were manually selected from dataset #3 (**Table S5**) to perform initial 2D classification and produce templates for autopicking. Template-based autopicking identified 207,026 particles, which were subjected to initial 2D and 3D classification and refinement as well as CTF refinement. 250,500 particles from data collections #1 and #2 (**Table S5**) Retromer datasets(*61*) were imported to combine with data collection #3. Multiple rounds of 2D classification yielded 72,795 particles suitable to continue to 3D classification. Initial models for 3D classification (*61*) were filtered to 60 Å resolution for use in these experiments. The particles underwent multiple rounds of CTF refinement and Bayesian polishing to produce a final set of 43,808 particles suitable for 3D refinement and postprocessing. The final masked model had a resolution of 4.9Å and a Relion-determined B-factor of -113.799.

For both reconstructions, rigid-body docking and map visualization were performed in Chimera(*112*) using the Fit in Map routine. Models for N-VPS35 and VPS26A subunits were obtained from PDB 5F0J.

Liposome preparation

Sucrose-loaded liposome binding assay were performed using the standard extrusion method with some modification (*113*). In brief, cargo loaded Folch liposomes were made by mixing 25 µl of 4 mg/ml N-terminal palmitoylated $CIMPR_{2347-2376}$ peptide, 50 µl of 10 mg/ml Folch fraction I (Sigma Aldrich) and 50 µl of 1 mg/ml di-C16 PtdIns(3)*P* (Echelon Biosciences), each freshly prepared in chloroform, to a total volume of 500 µl chloroform. The solution was dried down on the walls of a mini-round bottom flask under a N_2 stream and left overnight in a vacuum desiccator to yield a lipid film. This yields liposomes with a final PtdIns(3)P ratio of

10% (w/v). For PC/PE liposome, 50 µl of 10 mg/ml stock of 1-palmitoyl-2-oleoyl-sn-glycero-3-phosphocholine (POPC) and 1-palmitoyl-2-oleoyl phosphatidylethanolamine (POPE) in a 9:1 ratio (Avanti Polar Lipids) was freshly prepared in a 500 µl volume and lipid films formed using the same method as Folch liposomes. This results in a POPC/POPE liposome in a 90%:10% w/v ratio. To form multilamellar vesicles (MLV), the lipid films were hydrated with a buffer comprising 20 mM HEPES pH 7.5 and 220 mM sucrose with agitation follow by10 cycles of rapid freeze-thaw. The sucrose loaded heavy MLVs were centrifuged at 180,000 x *g* for 30 min at 4°C using Optima TL benchtop Ultracentrifuge (Beckman Coulter). The resulting pellets were buffer exchanged by resuspension into the assay buffer comprising 50 mM HEPES pH 7.5, 125 mM NaCl, 0.5 mM TCEP. To avoid buffer mismatch, the protein samples were also buffer exchanged into the same buffer.

Liposome-Binding Assays

The binding assay was performed in a total volume of 80 µl comprising 40 µl of sucrose-loaded MLVs and 7 µM Retromer, 7 µM SNX3 or 7 µM of Retromer – SNX3 mixture in 1 to 1 ratio. The reaction mixtures were incubated at room temperature for 15 min followed by centrifugation at 36000 x *g* using Optima TL benchtop ultracentrifuge (Beckman Coulter) for 15 min at 4°C. The supernatant and pelleted fractions were then carefully separated. The pellet was then resuspended in 80 µl of buffer containing 50 mM HEPES pH 7.5, 125 mM NaCl, 0.5 mM TCEP before analyzed by SDS-PAGE.

Statistics

Statistical analysis was completed in R studio using dplyr, ggplot2, ggpubr packages. Error bars on graphs were represented as the standard error of the mean (± SEM). P values were calculated using the two-tailed Student's *t*-test. $P < 0.05$ was considered as significant.

Data deposition

Crystal structural data have been deposited at the Protein data bank (PDB) under the accession number 6XS5 (hVPS29 – RT-D1), 6XS7 (hVPS29 – RT-D2), 6XS8 (ctVPS29 – RT-D3), 6XS9 (hVPS29 – RT-L1), and 6XSA (hVPS29 – RT-L2). CryoEM data has been deposited at the Electron Micrscopy Data Bank (EMDB) under accession numbers D_1000253118 and D_1000253090 for the apo and RT-L4-bound Retromer complexes respectively. All the relevant raw data related to this study is available from the corresponding authors on request.

Acknowledgments

We acknowledge the use of the Australian Microscopy and Microanalysis Research Facility at the Centre for Microscopy and Microanalysis at The University of Queensland. We also acknowledge use of the University of Queensland Remote Operation Crystallization and X-ray (UQ ROCX) Facility and the assistance of Gordon King and Karl Byriel. X-ray data were collected on the MX1 and MX2 microfocus beamline at the Australian Synchrotron. This work is supported by funds from the Australian Research Council (ARC) (DP160101743; DP180103244, CE140100011), National Health and Medical Research Council (NHMRC) (APP1156493; APP1156732), and Bright Focus Foundation (A2018627S). BMC is supported by an NHMRC Senior Research Fellowship (APP1136021), DPF by an NHMRC Senior Principal Research Fellowship (1117017), RGP is supported by an NHMRC Senior Principal Research Fellowship (APP1058565) and by the Australian Research Council Centre of Excellence in Convergent Bio-Nano Science and Technology, and DAS is by an NHMRC Career Development Fellowship (APP1140851). This work was also supported by the Japan Agency for Medical Research and Development (AMED), Platform Project for Supporting Drug Discovery and Life Science Research (JP20am0101090) and the Japan Society for the Promotion of Science (JSPS), Specially Promoted Research (JP20H05618) to H.S. CryoEM data were collected at the Vanderbilt Center for Structural Biology Cryo-Electron Microscopy Facility. We thank Dr. Scott Collier and Dr. Melissa Chambers for data collection support. Some of this work was performed at the National Center for CryoEM Access and Training (NCCAT) and the Simons Electron Microscopy Center located at the New York Structural Biology Center, supported by the NIH Common Fund Transformative High Resolution Cryo-Electron Microscopy program (U24 GM129539), and by grants from the Simons Foundation (SF349247) and NY State Assembly. AKK, BX, and LPJ are supported by NIH R35GM119525. LPJ is a Pew Scholar in the Biomedical Sciences, supported by the Pew Charitable Trusts.

886 **FIGURE LEGENDS**

887

888 **Figure 1. Cyclic peptides reveal strong binding characteristics with Retromer.**

889 (**A**) Schematic diagram showing the RaPID system used to screen for cyclic peptides binding to Retromer. (**B**)
890 Eight Retromer-binding macrocyclic peptides were identified with either N-chloroacetyl-$_{D}$-tyrosine or N-
891 chloroacetyl-$_{L}$-tyrosine as initiating residues. (**C**) Binding of RT-D1, RT-D2, RT-D3, RT-L1, RT-L2, and RT-
892 L4 with Retromer (blue), Vps29 (light green), Vps26A (orange), Vps29 – Vps35 (red) and Vps26A – Vps35$_{1-}$
893 $_{390}$ (dark green) by ITC. SPR binding curves for each peptide are shown in **Fig. S3**. (**D**) ITC thermogram
894 showing that addition of α-helix 8 and 9 of Vps35 (residues 173 to 224) contributes to RT-L4 binding affinity
895 but is not essential for interaction. All ITC graphs represent the integrated and normalized data fit with 1 to 1
896 ratio binding. The binding affinity (K_d) is given as mean of at least three independent experiments (**Table S2**).
897 (**E**) Relative binding position of each cyclic peptide to Retromer based on the ITC measurements indicated on
898 the structure of the mouse Retromer complex (PDB ID 6VAC) (*61*).

899

900 **Figure 2. Crystal structures of Vps29 in complex with cyclic peptides.**

901 (**A**) Superimposition of the crystal structures of Vps29 in complex with five macrocyclic peptides. (**B**)
902 Sequence conservation mapped onto the hVPS29 structure surface highlights the conserved binding site for
903 each of the cyclic peptides, with RT-D1 shown as an example. (**C**) Superimposition of the Vps29 – RT-D1
904 peptide complex with the Vps29 - Vps35$_{483-780}$ crystal structure (PDB ID: 2R17) (*57*). The cyclic peptides bind
905 opposite to the Vps35 interface. (**D**) Details of macrocyclic peptides in stick representation bound to Vps29.
906 Schematic diagrams indicate the number of intermolecular contacts (salt bridge, hydrogen bonds and
907 hydrophobic interactions) of each residue on the peptide with Vps29. The residues on the peptide with 0, 1, 2
908 and ≥3 contacts are shown in grey, light green, green and dark green boxes respectively. Each peptide utilises
909 a core Pro-Leu sequence forming a β-hairpin, labelled as position 0 and 1 for reference. Electron density for
910 each peptide is shown in **Fig. S3**. (**E**) Close-up of the β-hairpin conformation of the bound RT-D1 peptide. (**F**)
911 TBC1D5 (PDB ID 5GTU) (*56*), VARP (PDB ID 6TL0) (*64*) and RIDL (PDB ID 5OSH) (*43*) bind to the same
912 site of Vps29 using a similar β-hairpin comprised of a Pro-Leu dipeptide sequence. For clarity, only the key
913 residues involve in the contact are shown. (**G**) ITC thermogram for the titration of RT-D1 (purple) and RT-D1
914 L7E (blue) with Retromer showing the importance of Pro-Leu motif in the interaction. The graph represents
915 the integrated and normalized data fit with a 1 to 1 binding ratio.

916

917 **Figure 3. The RT-L4 macrocylic peptide is a molecular chaperone that binds Retromer at the Vps35-**
918 **Vps26 interface.**

919 (**A**) Bar graph summarizing the measured thermal unfolding temperatures (T_m) of Retromer in the presence of
920 cyclic peptides. Raw data is shown in **Fig. S4**. (**B**) Pull-down assay showing the interaction of biotinylated
921 RT-L4 bound to streptavidin-coated agarose beads with either wild-type Vps26A-Vps35$_{1-390}$ subcomplex or

922 indicated point mutants. Individual Vps26A and $Vps35_{1-390}$ proteins do not bind the peptide, while the D128R
923 mutation in $Vps35_{1-390}$ specifically blocks sub-complex interaction. (**C**) Sequence conservation map of
924 Vps26A-$Vps35_{12-470}$ subcomplex (PDB ID 5F0L) highlighting the proposed RT-L4 binding site, and its
925 relationship to known binding sites for SNX3 (*59*) and SNX27 (*66*). **(D)** ITC thermograms showing that linear
926 RT-L4, or RT-L4 with alterations in bulky aramotic sidechains is unable to bind to Retromer. The graph
927 represents the integrated and normalized data fit with a 1 to 1 binding ratio. **(E)** Schematic diagram of RT-L4
928 highlighting aromatic residues important for binding to Retromer. (**F**) CryoEM reconstruction of the human
929 Retromer (apo form) and (**G**) in complex with RT-L4. CryoEM density shown as transparent molecular
930 envelope, with crystal structures of Retromer subcomplexes (PDB ID 2R17 and 5F0L) overlapped to the map
931 (contoured at 4.7σ). The additional density seen on addition of the cyclic peptide added Retromer supports the
932 mutagenesis data indicating RT-L4 binds at the Vps26 and Vps35 interface. (**H**) Enlarged view of the Vps26
933 and Vps35 interface highlighting the additional density in the CryoEM map of RT-L4 added Retromer but not
934 in the apo form. For clarity, D128 of Vps35 is highlighted in red.
935
936 **Figure 4. The effect of cyclic peptides on the interaction of Retromer with known regulatory and adaptor**
937 **proteins.**
938 (**A**) Interactions of Retromer with TBC1D5, SNX3, SNX27 and Fam21 in the presence of either RT-D3 or
939 RT-L4. GST-$TBC1D5_{TBC}$ and GST-$Fam21_{R19-R21}$ were used as baits for Retromer, while GST-tagged Retromer
940 (Vps29 subunit) was used as bait for SNX3 and SNX27. (**B**) ITC measurement of $TBC1D5_{TBC}$, (**C**) SNX3
941 (with DMT1-$II_{550-568}$ present), (**D**) SNX27, and (**E**) GST-$Fam21_{R19-R21}$ with Retromer in the presence or
942 absence of RT-D3 or RT-L4. (**F**) Hela cell lysates were incubated with streptavidin agarose coated with
943 biotinylated RT-D3 or RT-L4 and bound proteins subjected to SDS-PAGE and western blotting with
944 antibodies against indicated proteins. (**G**) ITC measurement of $PTHR_{586-593}$ cargo peptide (*98*) with $SNX27_{PDZ}$
945 alone (yellow), Retromer + RT-L4 (red), Retromer + $SNX27_{PDZ}$ (green) and Retromer + $SNX27_{PDZ}$ + RT-L4
946 (blue). RT-L4 allosterically enhances the affinity of Retromer + $SNX27_{PDZ}$ for cargo. The cargo peptide binds
947 to SNX27 All ITC graphs represent the integrated and normalized data fit with a 1 to 1 binding ratio. The
948 binding affinity (K_d) is given as mean of at least two independent experiments. (**H**) Liposome-binding assay
949 of Retromer with membrane-associated SNX3 cargo complex in the presence of cyclic peptides. Multilamellar
950 vesicles were composed of either control PC/PE lipids, or Folch I lipids containing added PtdIns(3)*P* and N-
951 terminal palmitoylated $CIMPR_{2347-2376}$ peptide (schematic diagram on top). "S" and "P" indicates unbound
952 supernatant and bound pellet respectively. Control experiments are shown in **Fig. S7B** and **S7C**. (**I**) Schematic
953 summarizing the effects of RT-D3 and RT-L4 on Retromer engagement with known regulatory, adaptor and
954 bacterial effector proteins.
955
956 **Figure 5. An autoinhibitory role for the disordered C-terminal tail of Vps26 in binding RT-L4 and**
957 **SNX3**.

958 (**A**) ITC thermogram for the titration of RT-L4 with $Vps35_{1-390}$ sub-complex with either full-length or C-
959 terminal truncated Vps26A and Vps26B paralogues. (**B**) Sequence alignment of the C-terminal region of
960 Vps26 highlighting the low-sequence similarity of the unstructured C-terminal tail apart from the QRF/YE
961 motif highlighted with a blue square. Sites of phosphorylation are indicated in circle (www.phosphosite.org)
962 (*69*). Hs, *Homo sapiens*; Dr, *Danio rerio*; Ct, *Chaetomium thermophilum*; Pf, *Plasmodium falciparum*, Sc,
963 *Saccharomyces cerevisiae.* (**C**) ITC measurement of SNX3 binding to native, phosphomimetic (pm), and C-
964 terminal tail truncated (ΔC) versions of Vps26A/B – $Vps35_{1-390}$ subcomplexes. In each case, the presence of
965 DMT1-II cargo peptide was required to detect SNX3 binding. (**D**) ITC measurement of SNX3 binding to
966 QRFE-AAAA mutant Vps26A – $Vps35_{1-390}$. ITC thermograms in (**A**), (**C**) and (**D**) represent the integrated and
967 normalized data fit with a 1 to 1 binding ratio. (**E**) Summary of binding affinities of SNX3 for each Vps26A/B
968 – $Vps35_{1-390}$ subcomplex in the presence of DMT1-$II_{550-568}$ cargo peptide. For clarity, the association constant
969 (K_d^{-1}) is shown. The binding affinity is given as mean of at least two independent experiments.
970
971 **Figure 6. Macrocyclic peptides can be used to study Retromer localization in cells.**
972 (**A**) Specific targeting of endosomal structures by streptolysin O (SLO) delivered cyclic peptides. HeLa cells
973 transiently expressing SNX1-mCherry were exposed to SLO at 37°C for 9 min before incubating with the
974 cyclic peptide RT-D3-FITC or RT-L4-FITC on ice for 5 min. Permeabilized cells were recovered in the
975 recovery medium containing Hoechst 33342 for 20 min, then fixed in 4% PFA. The negative control (-SLO)
976 shows no labeling of intracellular structures. Scale bar, 10 µm. Graphs show the fluorescence intensity of RT-
977 D3-FITC or RT-L4-FITC in HeLa cells (means ± SEM). Two-tailed Student's *t-test* was used to determine the
978 statistical significance (n=3). **, $P < 0.01$. (**B**) HeLa cells transiently expressing Vps35-mCherry were labeled
979 by SLO-delivered cyclic peptide RT-D3-FITC or RT-L4-FITC, fixed in 4% PFA, and imaged by Airyscan
980 super-resolution microscopy. Scale bar, 5 µm. (**C**) HeLa cells treated with SLO-delivered RT-D3-FITC, RT-
981 L4-FITC, or DMF control were incubated in recovery medium for 2 h, fixed in ice-cold methanol, and co-
982 immunolabeled with antibodies against endogenous TBC1D5 and SNX1, followed by Alexa Fluor-conjugated
983 fluorescent secondary antibodies. Scale bar, 10 µm. The colocalization between TBC1D5 and SNX1 was
984 quantified by Pearson's correlation coefficient and represented in the graph (means ± SEM). Two-tailed
985 Student's *t-test* was utilized to determine the statistical significance (n=3). ****, $P < 0.0001$; ns, not significant.
986
987

988 **SUPPLEMENTARY INFORMATION.**

989

990 **Figure S1. MALDI-TOF spectra of the Retromer associated cyclic peptides.**

991 The molecular mass of RT-D1, RT-D2, RT-D3, RT-D4, RT-L1, RT-L2, RT-L3 and RT-L4 are shown in the
992 spectrum.

993

994 **Figure S2. Preliminary SPR binding kinetics of Retromer-associated cyclic peptides.**

995 (**A**) Single cycle kinetics experiments were performed using SPR with His-tagged human or zebrafish
996 Retromer with varying concentrations of cyclic peptides. In each case, 2-fold serial dilutions of peptide were
997 tested starting from a highest concentration of 200 or 1000 nM as indicated. (**B**) Binding kinetics of
998 macrocyclic peptides for human and zebrafish Retromer complexes as determined by SPR. (**C**) Gels showing
999 purity of human and zebrafish Retromer complexes used for Rapid peptide screening and SPR experiments.

1000

1001 **Figure S3. Interaction analysis of Vps29 and cyclic peptides.**

1002 (**A**) Structures of the Vps29 bound cyclic peptides, RT-D1, RT-D2, RT-D3, RT-L1 and RT-L2. For clarity,
1003 the main chain backbones are shown in ribbon and side chains are shown in stick form. The electron density
1004 shown corresponds to a simulated-annealing OMIT Fo - Fc map contoured at 3σ. (**B**) Highlighted details of
1005 the residues involved in the interactions between Vps29 and bound macrocyclic peptides. (**C**) ITC thermogram
1006 showing that both linear and mutant form of RT-D1 binds weakly to Retromer. (**D**) ITC titration of RT-D2
1007 (red line) and RT-D3 (blue line) with ctVps29. Both graphs represent the integrated and normalized data fit
1008 with a 1 to 1 binding ratio. The binding affinity (K_d) is given as mean of three independent experiments. (**E**)
1009 Surface and (**F**) cartoon representations of the human Vps29 – RT-L1 structure highlighting the secondary
1010 binding site located opposite to the primary common binding site. Residues involve in contact with Vps35 are
1011 shown in light blue.

1012

1013 **Figure S4. RT-L4 enhances the thermal stability of Retromer in solution.**

1014 (**A**) Temperature dependent unfolding of Vps29 in the presence of 30-fold molar excess of RT-D1, RT-D2,
1015 RT-D3, RT-L1 and RT-L2. (**B**) Temperature dependent unfolding of native Retromer in the presence of 30-
1016 fold molar excess of RT-D1, RT-D2, RT-D3, RT-L1 and RT-L2 complexes, and (**C**) in the presence of 30-
1017 fold molar excess of RT-L4. Melting temperatures (Tm) were assessed by differential scanning fluorimetry.
1018 The sigmoidal curve is characteristic of cooperative thermal denaturation of a folded protein. A shift in melting
1019 temperature indicates the stabilization of the proteins upon the addition of cyclic peptide. (**D**) Dose-response
1020 curve of Retromer in the presence of RT-L4 (red line) or RT-D3 (green line).

1021

1022 **Figure S5. R55 does not significantly increase the thermal-stability of Retromer.**

1023 **(A**) Molecular mass of Retromer in the presence of RT-D3 and RT-L4 monitored by mass photometry. In this
1024 experiment, Retromer shows a mass of 151 kDa, corresponding to the heterotrimeric state of Retromer. (**B**)

1025 ITC thermogram for the titration of R55, compound 2a and RT-L4 with Retromer under two different
1026 concentrations. Both graphs represent the integrated and normalized data fit with a 1 to 1 binding ratio. The
1027 binding affinity (K_d) is given as mean of three independent experiments. (**C**) Temperature dependent unfolding
1028 of 3 μM Retromer (blue dot) compared with samples containing 60 μM of R55 (brown triangle), 60 μM
1029 compound 2a (orange rhombus) or 60 μM RT-L4 (green square). (**D**) Same as (**C**) but with 1 mM of R55
1030 showing two stages of unfolding. Note that preparation of 1 mM compound 2a and RT-L4 in aqueous buffer
1031 was not possible due solubility characteristics. (**E**) Summary of Retromer binding properties and thermal-
1032 stability effect of molecular chaperones R55, compound 2a and RT-L4.
1033
1034 **Figure S6. Binding of RT-L4 to Retromer from different species and assessed by cryoEM.**
1035 (**A**) ITC thermograms for the titration of RT-L4 with zebrafish Retromer showing a strong binding similar to
1036 human Retromer. (**B**) ITC thermograms for the titration of RT-L4 with *C. thermophilum* Retromer shows a
1037 lower affinity compared to zebrafish or human Retromer. The graphs represents the integrated and normalized
1038 data fit with a 1 to 1 binding ratio. The binding affinity (K_d) is given as mean of at least three independent
1039 experiments. (**C**) CryoEM density map of human Retromer (apo form) and in complex with RT-L4 displayed
1040 as mesh surface, with crystal structures of Retromer subcomplexes (PDB ID 2R17 and 5F0L) overlapped to
1041 the map. Red arrow indicates the Vps35 model fitting into α helices. Yellow arrow indicates the extra density
1042 observed between Vps26 and Vps35 interface in the RT-L4-bound Retromer. (**D**) Three different views of the
1043 Retromer CryoEM structure reconstructions highlighting the Vps35 and Vps26 interface. The cryoEM density
1044 from apo Retromer (grey mesh) is overlayed with the cryoEM density from RT-L4-bound Retromer (light blue
1045 surface). Maps were scaled to represent equivalent Å/pixel and box size in relion_image_handler and rendered
1046 in Chimera. *Apo* map shown at 1.096 Å/pixel and 220 pixel box size; retromer/RTL4 is shown at 1.099 Å/pixel
1047 and 228 pixel box size. (**E**) Fourier Shell Correlation (FSC) plots highlighting masked and unmasked resolution
1048 estimates from RELION are shown for Retromer (apo form) and in complex with RT-L4. The intersections of
1049 the curve with FSC=0.143 (grey dotted line) are shown. (**F**) Angular distribution of the particles used for the
1050 final round of refinement. The height and colour of the cylinder bars is proportional to the number of particles
1051 in those views.
1052
1053 **Figure S7. The effect of cyclic peptides on the interaction of Retromer with RidL, Rab7a and SNX3.**
1054 (**A**) ITC measurements of $RidL_{1-236}$ with Retromer in the presence or absence of RT-D3. (**B**) Interaction of RT-
1055 L4 with Retromer, $SNX27_{PDZ}$, $TBC1D5_{TBC}$ and SNX3 demonstrate the binding specificity of the cyclic peptide
1056 to Retromer. (**C**) GAP-stimulated GTPase activity of Rab7a in the presence of $TBC1D5_{TBC}$ and Retromer.
1057 Effect of cyclic peptide was perfomed by adding either RT-D3 or RT-L4 into the reaction. For the native
1058 control, equivalent percentage (v/v) of DMSO was added to the reaction. (**D**) Retromer and RT-L4 shows
1059 enhancement of GAP-stimuated GTPase activity of Rab7a over TBC1D5 alone. Two-tailed Student's *t-test*
1060 was utilized to determine the statistical significance (n=3). ****, $P < 0.0001$; *, $P<0.05$, ns, not significant.
1061 (**E**) Liposome-binding assay of SNX3 and Retromer using Folch I liposomes containing 10% PtdIns(3)*P* and

10% N-terminal palmitoylated $CIMPR_{2347-2376}$ peptide. (**F**) Liposome-binding assay of Retromer and SNX3 mixture as in (**E**) except Folch I liposomes contain only 10% PtdIns(3)*P* without the CI-MPR cargo. Retromer binds only weakly to Folch liposomes in the absence of either SNX3 or cargo sequence. In all three SDS-PAGE gels, "S" indicates unbound supernatant and "P" indicates bound pellet after ultracentrifugation. (**G**) ITC measurement of SNX3 with Vps26A –$Vps35_{1-390}$ subcomplex in the presence of $CIMPR_{2347-2376}$ cargo peptide. The graph represents the integrated and normalized data fit with a 1 to 1 binding ratio. The binding affinity (K_d) is given as mean of three independent experiments.

Figure S8. Sequence alignment of Vps29 and Vps35.

(A) Sequence alignment of the C-terminal region of Vps26 and (**B**) the N-terminal region of Vps35 showing the similarity between species. Key residues involve in contacts with Vps35 (yellow arrow) and Vps26 (blue dots) are labelled on top of the sequence. h, *Homo sapiens*; zf, *Danio rerio*; Ct, *Chaetomium thermophilum*; m, *Mus musculus.*

Figure S9. ctVps26 C-terminal disordered tail reveals similar autoinhibitory characteristics.

ITC measurement of RT-L4 with native and ctVps26 C-terminal tail truncated ctRetromer. The graph represents the integrated and normalized data fit with a 1 to 1 ratio binding. The binding affinity (K_d) is given as mean of at least three independent experiments.

Figure S10. Electroporation of RT-D3 inhibits Retromer-dependent endosomal localisation of TBC1D5.

(**A**) HeLa cells were electroporated with either RT-D3 peptide or scrambled RT-D3 as a negative control. Electroporated cells were recovered for 16 h, fixed and then labelled for endogenous TBC1D5 (cyan) and Vps26A (magenta). In a large proportion of cells (indicated by dashed areas) the endosomal colocalisation of TBC1D5 with Vps26A was significantly reduced. (**B**) The colocalization between TBC1D5 and SNX1 was quantified by Pearson's correlation coefficient (means ± SEM). Two-tailed Student's *t-test* was used to determine the statistical significance (n=3). ****, $P < 0.0001$; ns, not significant.

Figure S11. Unprocessed original scans of western blots for the main figure.

Unprocessed images of all blots in this study.

1091 **Table S1: List of synthesized cyclic peptides.**

Name	Sequence	Ext. Co.	MW. (Da)
Cyclic peptides from initial screen			
RT-D1	Ac-yIIDTPLGVFLSSLKRC-NH2	1490	1963.9
RT-D2	Ac-yTTIYWTPLGTFPRIRC-NH2	8480	2126.9
RT-D3	Ac-yGYDPLGLKYFAC-NH2	4470	1548.6
RT-D4	Ac-yGWDPLYVNYFVC-NH2	9970	1677.7
RT-L1	Ac-YIKTPLGTFPNRHGC-NH2	1490	1742.9
RT-L2	Ac-YLPTITGVGHLWHPLC-NH2	6990	1845.9
RT-L3	Ac-YLEFDPLYVRLFYVNC-NH2	4470	2093.0
RT-L4	Ac-YWISNSWTTYRYVSTC-NH2	15470	2068.9
Modified cyclic peptides			
RT-D1 L7E	Ac-yIIDTPEGVFLSSLKRC-NH2	1490	1979.9
RT-D1 FLSL/AAAA	Ac-yIIDTPLGVAASAAKRC-NH2	1490	1803.6
RT-D1 linear	yIIDTPLGVFLSSLKRC	1490	1925.3
RT-D3-scramble	Ac-yGLYLKYGFPDAC-NH2	4470	1548.6
RT-L4 W2A/W7A	Ac-YAISNSATTYRYVSTC-NH2	4470	1838.6
RT-L4 Y10A/Y12A	Ac-YWISNSWTTARAVSTC-NH2	12490	1884.7
RT-L4 linear	YWISNSWTTYRYVSTC	15470	2030.2
Biotinylated RT-D3	Ac-[yGYDPLGLKYFAC]AGAGK(Biotin)-NH2	4470	2195.4
Biotinylated RT-L4	Ac-[YWISNSWTTYRYVSTC]AGAGK(Biotin)-NH2	15470	2715.7
RT-D3-FITC	Ac-[yGYDPLGLKYFAC]AGAGK(FITC)-NH2	4470	2340.4
RT-L4-FITC	Ac-[YWISNSWTTYRYVSTC]AGAGK(FITC)-NH2	15470	2860.7
RT-D3-TAT-FITC	Ac-yGYDPLGLKYFAC-(GRKKRRQRRR)-(FITC)-NH2	4470	3737.1
RT-D3-TAT-FITC (PL/AA)	Ac-yGYDAAGLKYFAC-(GRKKRRQRRR)-(FITC)-NH2	4470	3668.9
RT-L4-TAT-FITC	Ac-YWISNSWTTYRYVSTC-(GRKKRRQRRR)-(FITC)-NH2	15470	4257.4

1092 All peptides have >95% purity determined by analytical RP-UPLC.

1093

1094 **Table S2: Thermodynamic parameters for the binding of Retromer with cyclic peptides by ITC.**

	K_d (nM)	ΔH (kcal/mol)	ΔG (kcal/mol)	$-T\Delta S$ (kcal/mol)
Retromer				
RT-D1	130 ± 9	-11.5 ± 0.5	-9.4 ± 0.08	2.1 ± 0.6
RT-D2	53 ± 6	-9.7 ± 1.6	-9.9 ± 0.08	0.5 ± 0.2
RT-D3	25 ± 1	-13.4 ± 1.4	-10.4 ± 0.06	3.9 ± 0.1
RT-L1	96 ± 1	-11.0 ± 0.9	-9.5 ± 0.06	1.4 ± 0.9
RT-L2	852 ± 14	-16.0 ± 0.7	-8.2 ± 0.06	7.7 ± 0.7
RT-L4	273 ± 7	-7.0 ± 0.1	-8.9 ± 0.08	-2.0 ± 0.1
RT-D1 FLSL/AAAA	2195 ± 686	-4.3 ± 0.9	-7.7 ± 0.09	-3.5 ± 1.1
RT-D1 linear	763 ± 55	-7.2 ± 0.3	-8.3 ± 0.06	-1.1 ± 0.3
RT-L4 W2A/W7A		No binding detected		
RT-L4 Y10A/Y12A		No binding detected		
RT-L4 linear		No binding detected		
Vps29				
RT-D1	95 ± 1	-14.2 ± 0.3	-9.5 ± 0.06	4.6 ± 0.3
RT-D2	64 ± 1	-11.6 ± 0.1	-9.8 ± 0.08	1.7 ± 0.1
RT-D3	8 ± 2	-17.4 ± 1.4	-11.1 ± 0.21	6.4 ± 1.2
RT-L1	64 ± 5	-13.0 ± 1.1	-9.8 ± 0.08	3.2 ± 1.0
RT-L2	783 ± 7	-9.1 ± 1.6	-8.4 ± 0.06	1.6 ± 0.9
RT-L4		No binding detected		
Vps29-Vps35				
RT-D1	106 ± 4	-10.5 ± 0.4	-9.5 ± 0.09	0.9 ± 0.3
RT-D2	65 ± 5	-11.2 ± 1.0	-9.8 ± 0.07	1.4 ± 0.9
RT-D3	29 ± 2	-11.6 ± 1.3	-10.3 ± 0.08	2.4 ± 1.1
RT-L1	90 ± 3	-7.9 ± 1.2	-9.6 ± 0.07	1.8 ± 1.0
RT-L2	763 ± 12	-8.7 ± 1.7	-8.4 ± 0.08	2.1 ± 1.1
RT-L4		No binding detected		
Vps26-Vps35 truncations				
Vps26A_Vps35$_{1-390}$: RT-L4	165 ± 8	-6.8 ± 1.2	-9.2 ± 0.06	-2.5 ± 1.2
Vps26B_Vps35$_{1-390}$: RT-L4	491 ± 27	-2.7 ± 1.2	-8.6 ± 0.10	-5.4 ± 0.4
Vps26A_Vps35$_{1-224}$: RT-L4	222 ± 4	-7.0 ± 1.7	-9.1 ± 0.11	-2.1 ± 1.7
Vps26A_Vps35$_{1-172}$: RT-L4	339 ± 7	-6.3 ± 2.5	-8.8 ± 0.10	-2.5 ± 2.5
Vps26A$_{9-298}$_Vps35$_{1-390}$: RT-L4 (Δ C-term. tail complex)	33 ± 2	-11.9 ± 1.0	-10.2 ± 0.07	1.7 ± 1.0

Vps26A				
RT-D1, D2, D3, L1, L2, L4	No binding detected			
zfRetromer				
RT-L4	88 ± 11	-6.9 ± 1.8	-9.6 ± 0.08	-2.6 ± 2.0
ctRetromer				
RT-L4	5030 ± 900	-7.4 ± 0.3	-7.3 ± 0.10	-2.7 ± 1.9
ctRetromer ΔC-term. tail				
RT-L4	1770 ± 170	-6.0 ± 0.7	-7.9 ± 0.06	-1.9 ± 0.7
ctVps29				
RT-D2	135 ± 3	-10.5 ± 1.0	-9.3 ± 0.08	1.1 ± 0.9
RT-D3	603 ± 6	-7.4 ± 0.3	-8.5 ± 0.07	-0.9 ± 0.1

1095

1096

1097 **Table S3. Summary of crystallographic structure determination statistics**

Data collection statistics	Vps29 - RT-D1	Vps29 - RT-D2	ctVps29 - RT-D3	Vps29 – RT-L1	Vps29 - RT-L2
PDB ID	6XS5	6XS7	6XS8	6XS9	6XSA
Space group	C121	$P2_12_12$	$P3_121$	$P4_12_12$	$P2_12_12$
Resolution (Å)	42.41 – 2.01 (2.06 – 2.01)	48.00 – 1.58 (1.61 – 1.58)	42.75 – 1.83 (1.87 – 1.83)	49.16 – 2.69 (2.82 – 2.69)	44.10 – 1.83 (1.87 – 1.83)
a, b, c (Å)	114.39, 43.77, 43.14	38.06, 144.01, 43.02	47.52, 47.52, 170.99	119.44, 119.44, 125.63	37.48, 132.30, 39.87
α, β, γ (°)	90.0, 100.5, 90.0	90.0, 90.0, 90.0	90.0, 90.0, 120.0	90.0, 90.0, 90.0	90.0, 90.0, 90.0
Total observations	98,823 (7,278)	440,767 (17,466)	217,001 (12,613)	142,659 (11,469)	125,257 (6,931)
Unique reflections	14,170 (1,030)	33,360 (1,514)	20,529 (1,206)	25,371 (3,013)	18,052 (1,041)
Completeness (%)	99.9 (98.8)	99.6 (92.7)	99.6 (99.0)	97.8 (88.9)	98.6 (93.5)
R_{merge}^{+}	0.077 (0.585)	0.062 (0.712)	0.039 (0.146)	0.085 (0.557)	0.080 (0.264)
R_{pim*}	0.032 (0.235)	0.018 (0.213)	0.013 (0.047)	0.053 (0.421)	0.035 (0.110)
CC1/2	0.999 (0.917)	1.000 (0.867)	1.000 (0.995)	0.997 (0.879)	0.996 (0.976)
$\langle I/\sigma(I)\rangle$	12.2 (2.5)	18.9 (2.6)	28.0 (9.5)	8.2 (1.3)	15.5 (6.4)
Multiplicity	6.9 (7.0)	13.0 (11.5)	10.2 (10.5)	5.6 (3.8)	6.3 (6.6)
Molecule/asym	1	1	1	2	1
Refinement statistics					
R_{work}/R_{free} (%) ¶#	19.0/22.5	17.8/19.1	20.5/25.1	24.7/28.8	19.0/22.7
No. protein atoms	1469	1523	1483	2986	1481
Waters	87	179	165	38	191
Ligand (peptide)	143	155	110	492	131
Wilson B ($Å^2$)	26.4	19.2	16.9	68.9	17.1
Average B ($Å^2$)^	32.3	24.2	21.5	111.0	20.6
Protein	32.3	22.5	20.1	108.0	19.6
Cyclic peptide	27.9	27.7	30.9	101.8	21.1
Water	35.9	36.4	26.6	88.5	28.4
rmsd bonds (Å)	0.007	0.011	0.011	0.017	0.007
rmsd angles (°)	1.210	1.101	1.314	1.968	0.968
Ramachandran plot:					
Favored/outliers (%)	96.5/1.0	98.6/0.0	99.0/0.0	95.3/1.4	98.0/0.5

1098 Values in parentheses refer to the highest resolution shell. $^{+}R_{merge} = \Sigma|I - \langle I\rangle| / \Sigma\langle I\rangle$, where I is the intensity of each individual reflection. $*R_{pim}$ indicates
1099 all I^{+} & I^{-}. $^{¶}R_{work} = \Sigma h|F_o - F_c| / \Sigma_i|F_o|$, where F_o *and* F_c are the observed and calculated structure-factor amplitudes for each reflection h. $^{\#}R_{free}$ was
1100 calculated with 10% of the diffraction data selected randomly and excluded from refinement. ^Calculated using Baverage.

1101

1102 **Table S4: Thermodynamic parameters for the binding of Retromer with R55 and compound 2a**

	K_d (μM)	ΔH (kcal/mol)	ΔG (kcal/mol)	$-T\Delta S$ (kcal/mol)
Retromer				
R55	18.2 ± 5.0	-0.8 ± 0.3	-6.5 ± 0.2	-5.7 ± 0.5
Compound 2a	8.3 ± 0.8	-1.1 ± 0.9	-6.9 ± 0.05	-5.8 ± 1.0

1103

1104 **Table S5: CryoEM data collection parameters for 3KE Retromer complex in the presence of the RT-**
1105 **L4 cyclic peptide.**
1106

	Retromer + RT-L4		***apo* Retromer**	
EMDB ID	D_1000253090		D_1000253118	
Microscope	ThermoFisher FEI Titan Krios G3i Vanderbilt V-CEM	FEI Titan Krios Krios2 NRAMM Data collection 1	FEI Titan Krios Krios3 NRAMM Data collection 2	FEI Titan Krios Krios3 NRAMM Data collection 3
Cs	2.7 mm	2.7 mm	2.7 mm	2.7 mm
Voltage	300 keV	300 keV	300 keV	300 keV
Detector	ThermoFisher Falcon 3 direct electron detector	Gatan K2 Summit direct electron detector	Gatan K2 Summit direct electron detector	Gatan K2 Summit direct electron detector
Magnification	120,000x	105,000x	105,000x	105,000x
Pixel size	0.6811Å/pix	1.096Å/pix	1.06Å/pix (rescaled to 1.096Å/pix with motioncorr2 script)	1.06Å/pix (rescaled to 1.096Å/pix with motioncorr2 script)
Dose rate	$1.4e^-/Å^2/sec$	$\sim 8e^-/Å^2/sec$	$\sim 8e^-/Å^2/sec$	$\sim 8e^-/Å^2/sec$
Total dose	$50e^-/A^2$	$69.34e^-/Å^2$	$73.92e^-/Å^2$	$73.92e^-/Å^2$
Tilt	+/-30°	N/A	N/A	+/-15°
Defocus range	-0.8 to -2.6µm	-0.7 to 2.6µm	-0.8 to -4.4µm	-0.8 to -4.7µm
Number of micrographs	4,791	1,480	1,299	891
Total particles (autopicked)	968,806	(250,500 particles selected from these datasets; Kendall *et al*., 2020)		207,026
Box size (Å)	251 Å		241 Å	
Particles in 2D classification	171,270		72,795	
Particles in final 3D model	28,083		43,808	
Symmetry	C1		C1	
Map resolution (masked FSC 0.143, RELION)	5.9Å		4.9Å	
B-factor	-88		-114	

1107 **Table S6: Thermodynamic parameters for the binding of Retromer and its partners in the presence of**
1108 **RT-D3 or RT-L4 cyclic peptides.**

	K_d (μM)	ΔH (kcal/mol)	ΔG (kcal/mol)	$-T\Delta S$ (kcal/mol)
TBC1D5$_{TBC}$				
Retromer + DMSO (Native)	0.37 ± 0.02	-2.5 ± 0.8	-8.8 ± 0.03	-6.2 ± 0.8
Retromer + RT-D3		No binding detected		
Retromer + RT-L4	0.19 ± 0.01	-5.7 ± 0.1	-9.2 ± 0.06	-3.5 ± 0.1
SNX27$_{PDZ}$				
Retromer + DMSO (Native)	13.0 ± 0.5	-1.1 ± 0.1	-6.7 ± 0.03	-5.6 ± 0.2
Retromer + RT-D3	15.1 ± 0.4	-1.2 ± 0.3	-6.6 ± 0.08	-5.4 ± 0.2
Retromer + RT-L4	8.2 ± 1.0	-5.5 ± 0.3	-6.9 ± 0.07	-1.4 ± 0.4
PTHR$_{586-593}$				
mSNX27$_{PDZ}$	5.2 ± 0.4	-10.6 ± 0.4	-7.2 ± 0.05	3.3 ± 0.4
Retromer + mSNX27$_{PDZ}$	2.4 ± 0.3	-11.1 ± 1.8	-7.7 ± 0.08	3.5 ± 1.9
Retromer + mSNX27$_{PDZ}$ + RT-L4	0.7 ± 0.1	-12.5 ± 0.6	-8.4 ± 0.05	4.3 ± 0.3
SNX3				
Retromer + DMT1* + DMSO (Native)	154.0 ± 25	-32.4 ± 9.8	-5.2 ± 0.14	27.1 ± 9.8
Retromer + DMT1* + RT-D3	164.0 ± 3	-33.2 ± 0.4	-5.2 ± 0.02	28.0 ± 0.4
Retromer + DMT1* + RT-L4	230.0 ± 14	-14.0 ± 0.6	-5.0 ± 0.03	9.0 ± 0.6
GST-Fam21$_{R19-R21}$				
Retromer + DMSO (Native)	10.6 ± 0.7	-16.5 ± 0.6	-6.8 ± 0.04	9.8 ± 0.9
Retromer + RT-D3	25.8 ± 0.5	-9.3 ± 3.3	-6.3 ± 0.02	4.0 ± 1.9
Retromer + RT-L4	2.8 ± 0.8	-26.0 ± 1.6	-7.5 ± 0.02	18.4 ± 1.8
RidL$_{1-236}$				
Retromer + DMSO (Native)	0.20 ± 0.02	-5.2 ± 0.9	-9.2 ± 0.07	-4.0 ± 1.0
Retromer + RT-D3	41.1 ± 1.8	-4.6 ± 1.3	-5.9 ± 0.02	-1.4 ± 1.3

1109 DMT1* corresponds to DMT1-II$_{550-568}$.

1110

1111 **Table S7. Thermodynamic parameters for the binding of Vps26 – Vps35 subcomplex with**
1112 **SNX3 in the presence of cargo peptide**.

	K_d (μM)	ΔH (kcal/mol)	ΔG (kcal/mol)	$-T\Delta S$ (kcal/mol)
Vps26A – Vps35$_{1\text{-}390}$ – DMT1-II$_{550\text{-}568}$: SNX3				
Native	149 ± 9	-14.6 ± 0.3	-5.2 ± 0.05	10.4 ± 1.6
Phosphomimetic mutant (pm)	61 ± 3	-18.7 ± 0.7	-5.8 ± 0.03	13.0 ± 0.8
QRFE to AAAA mutant	50 ± 2	-23.0 ± 3.2	-5.9 ± 0.03	17.1 ± 3.0
ΔC-term. tail (ΔC)	32 ± 1	-28.3 ± 0.2	-6.1 ± 0.04	22.1 ± 0.4
Vps26A – Vps35$_{1\text{-}390}$ – CIMPR$_{2347\text{-}2376}$: SNX3				
Native	201 ± 9	-11.8 ± 0.9	-5.1 ± 0.03	6.6 ± 0.8
Vps26A – Vps35$_{1\text{-}390}$: SNX3				
Native		No binding detected		
Phosphomimetic mutant (pm)		No binding detected		
ΔC-term.tail (ΔC)		No binding detected		
Vps26B – Vps35$_{1\text{-}390}$ – DMT1-II$_{550\text{-}568}$: SNX3				
Native	193 ± 4	-13.8 ± 0.5	-5.1 ± 0.02	8.7 ± 0.6
Phosphomimetic mutant (pm)	64 ± 2	-12.3 ± 2.3	-5.7 ± 0.02	7.1 ± 1.5
ΔC-term.tail (ΔC)	34 ± 2	-24.7 ± 2.7	-6.1 ± 0.03	18.6 ± 2.7
Vps26B – Vps35$_{1\text{-}390}$: SNX3				
Native		No binding detected		
Phosphomimetic mutant (pm)		No binding detected		
ΔC-term.tail (ΔC)		No binding detected		

1113

1114 **References**

1115 1. P. J. Cullen, F. Steinberg, To degrade or not to degrade: mechanisms and significance of endocytic
1116 recycling. *Nat Rev Mol Cell Biol* **19**, 679-696 (2018).

1117 2. K. E. Chen, M. D. Healy, B. M. Collins, Towards a molecular understanding of endosomal
1118 trafficking by Retromer and Retriever. *Traffic* **20**, 465-478 (2019).

1119 3. S. Weeratunga, B. Paul, B. M. Collins, Recognising the signals for endosomal trafficking. *Curr Opin*
1120 *Cell Biol* **In press**, (2020).

1121 4. C. Burd, P. J. Cullen, Retromer: a master conductor of endosome sorting. *Cold Spring Harb*
1122 *Perspect Biol* **6**, (2014).

1123 5. N. Heucken, R. Ivanov, The retromer, sorting nexins and the plant endomembrane protein
1124 trafficking. *J Cell Sci* **131**, (2018).

1125 6. M. Ma, C. G. Burd, Retrograde trafficking and plasma membrane recycling pathways of the budding
1126 yeast Saccharomyces cerevisiae. *Traffic* **21**, 45-59 (2020).

1127 7. M. N. J. Seaman, Retromer and Its Role in Regulating Signaling at Endosomes. *Prog Mol Subcell*
1128 *Biol* **57**, 137-149 (2018).

1129 8. M. N. Seaman, J. M. McCaffery, S. D. Emr, A membrane coat complex essential for endosome-to-
1130 Golgi retrograde transport in yeast. *J Cell Biol* **142**, 665-681 (1998).

1131 9. H. Zhang *et al.*, The Retromer Complex and Sorting Nexins in Neurodegenerative Diseases. *Front*
1132 *Aging Neurosci* **10**, 79 (2018).

1133 10. J. Follett *et al.*, The Vps35 D620N mutation linked to Parkinson's disease disrupts the cargo sorting
1134 function of retromer. *Traffic* **15**, 230-244 (2014).

1135 11. S. A. Small, G. A. Petsko, Retromer in Alzheimer disease, Parkinson disease and other neurological
1136 disorders. *Nat Rev Neurosci* **16**, 126-132 (2015).

1137 12. C. Vilarino-Guell *et al.*, VPS35 mutations in Parkinson disease. *Am J Hum Genet* **89**, 162-167
1138 (2011).

1139 13. E. T. Williams, X. Chen, D. J. Moore, VPS35, the Retromer Complex and Parkinson's Disease. *J*
1140 *Parkinsons Dis* **7**, 219-233 (2017).

1141 14. E. Zavodszky *et al.*, Mutation in VPS35 associated with Parkinson's disease impairs WASH complex
1142 association and inhibits autophagy. *Nat Commun* **5**, 3828 (2014).

1143 15. A. Zimprich *et al.*, A mutation in VPS35, encoding a subunit of the retromer complex, causes late-
1144 onset Parkinson disease. *Am J Hum Genet* **89**, 168-175 (2011).

1145 16. S. A. Small *et al.*, Model-guided microarray implicates the retromer complex in Alzheimer's disease.
1146 *Ann Neurol* **58**, 909-919 (2005).

1147 17. P. Tammineni, Y. Y. Jeong, T. Feng, D. Aikal, Q. Cai, Impaired axonal retrograde trafficking of the
1148 retromer complex augments lysosomal deficits in Alzheimer's disease neurons. *Hum Mol Genet* **26**,
1149 4352-4366 (2017).

1150 18. B. N. Vardarajan *et al.*, Identification of Alzheimer disease-associated variants in genes that regulate
1151 retromer function. *Neurobiol Aging* **33**, 2231 e2215-2231 e2230 (2012).

1152 19. L. Wen *et al.*, VPS35 haploinsufficiency increases Alzheimer's disease neuropathology. *J Cell Biol*
1153 **195**, 765-779 (2011).

1154 20. L. Muzio *et al.*, Retromer stabilization results in neuroprotection in a model of Amyotrophic Lateral
1155 Sclerosis. *Nat Commun* **11**, 3848 (2020).

1156 21. K. J. McMillan, H. C. Korswagen, P. J. Cullen, The emerging role of retromer in neuroprotection.
1157 *Curr Opin Cell Biol* **47**, 72-82 (2017).

1158 22. I. J. McGough *et al.*, Retromer binding to FAM21 and the WASH complex is perturbed by the
1159 Parkinson disease-linked VPS35(D620N) mutation. *Curr Biol* **24**, 1670-1676 (2014).

1160 23. M. E. Otero-Ramirez, T. Passioura, H. Suga, Structural Features and Binding Modes of Thioether-
1161 Cyclized Peptide Ligands. *Biomedicines* **6**, (2018).

1162 24. A. W. Fjorback *et al.*, Retromer binds the FANSHY sorting motif in SorLA to regulate amyloid
1163 precursor protein sorting and processing. *J Neurosci* **32**, 1467-1480 (2012).

1164 25. K. J. McMillan *et al.*, Atypical parkinsonism-associated retromer mutant alters endosomal sorting of
1165 specific cargo proteins. *J Cell Biol* **214**, 389-399 (2016).

1166 26. L. N. Munsie *et al.*, Retromer-dependent neurotransmitter receptor trafficking to synapses is altered
1167 by the Parkinson's disease VPS35 mutation p.D620N. *Hum Mol Genet* **24**, 1691-1703 (2015).

1168 27. F. L. Tang *et al.*, VPS35 in Dopamine Neurons Is Required for Endosome-to-Golgi Retrieval of
1169 Lamp2a, a Receptor of Chaperone-Mediated Autophagy That Is Critical for alpha-Synuclein
1170 Degradation and Prevention of Pathogenesis of Parkinson's Disease. *J Neurosci* **35**, 10613-10628
1171 (2015).

1172 28. A. Jimenez-Orgaz *et al.*, Control of RAB7 activity and localization through the retromer-TBC1D5
1173 complex enables RAB7-dependent mitophagy. *EMBO J* **37**, 235-254 (2018).

1174 29. F. L. Tang *et al.*, VPS35 Deficiency or Mutation Causes Dopaminergic Neuronal Loss by Impairing
1175 Mitochondrial Fusion and Function. *Cell Rep* **12**, 1631-1643 (2015).

1176 30. W. Wang, X. Ma, L. Zhou, J. Liu, X. Zhu, A conserved retromer sorting motif is essential for
1177 mitochondrial DLP1 recycling by VPS35 in Parkinson's disease model. *Hum Mol Genet* **26**, 781-789
1178 (2017).

1179 31. W. Wang *et al.*, Parkinson's disease-associated mutant VPS35 causes mitochondrial dysfunction by
1180 recycling DLP1 complexes. *Nat Med* **22**, 54-63 (2016).

1181 32. X. Chen *et al.*, Parkinson's disease-linked D620N VPS35 knockin mice manifest tau neuropathology
1182 and dopaminergic neurodegeneration. *Proc Natl Acad Sci U S A* **116**, 5765-5774 (2019).

1183 33. J. Follett *et al.*, Parkinson Disease-linked Vps35 R524W Mutation Impairs the Endosomal
1184 Association of Retromer and Induces alpha-Synuclein Aggregation. *J Biol Chem* **291**, 18283-18298
1185 (2016).

1186 34. F. L. Tang *et al.*, Coupling of terminal differentiation deficit with neurodegenerative pathology in
1187 Vps35-deficient pyramidal neurons. *Cell Death Differ*, (2020).

1188 35. R. Bayliss, J. Wheeldon, S. M. Caucheteux, C. M. Niessen, V. Piguet, Identification of host
1189 trafficking genes required for HIV-1 virological synapse formation in dendritic cells. *J Virol*,
1190 (2020).

1191 36. E. Groppelli, A. C. Len, L. A. Granger, C. Jolly, Retromer regulates HIV-1 envelope glycoprotein
1192 trafficking and incorporation into virions. *PLoS Pathog* **10**, e1004518 (2014).

1193 37. J. C. Hsiao *et al.*, Intracellular Transport of Vaccinia Virus in HeLa Cells Requires WASH-
1194 VPEF/FAM21-Retromer Complexes and Recycling Molecules Rab11 and Rab22. *J Virol* **89**, 8365-
1195 8382 (2015).

1196 38. A. Popa *et al.*, Direct binding of retromer to human papillomavirus type 16 minor capsid protein L2
1197 mediates endosome exit during viral infection. *PLoS Pathog* **11**, e1004699 (2015).

1198 39. Z. Daniloski *et al.*, Identification of Required Host Factors for SARS-CoV-2 Infection in Human
1199 Cells. *Cell* **184**, 92-105 e116 (2021).

1200 40. K. Barlocher *et al.*, Structural insights into Legionella RidL-Vps29 retromer subunit interaction
1201 reveal displacement of the regulator TBC1D5. *Nat Commun* **8**, 1543 (2017).

1202 41. I. Finsel *et al.*, The Legionella effector RidL inhibits retrograde trafficking to promote intracellular
1203 replication. *Cell Host Microbe* **14**, 38-50 (2013).

1204 42. H. E. Miller, C. L. Larson, R. A. Heinzen, Actin polymerization in the endosomal pathway, but not
1205 on the Coxiella-containing vacuole, is essential for pathogen growth. *PLoS Pathog* **14**, e1007005
1206 (2018).

1207 43. M. Romano-Moreno *et al.*, Molecular mechanism for the subversion of the retromer coat by the
1208 Legionella effector RidL. *Proc Natl Acad Sci U S A* **114**, E11151-E11160 (2017).

1209 44. J. Yao *et al.*, Mechanism of inhibition of retromer transport by the bacterial effector RidL. *Proc Natl*
1210 *Acad Sci U S A* **115**, E1446-E1454 (2018).

1211 45. P. Zhang, G. Monteiro da Silva, C. Deatherage, C. Burd, D. DiMaio, Cell-Penetrating Peptide
1212 Mediates Intracellular Membrane Passage of Human Papillomavirus L2 Protein to Trigger
1213 Retrograde Trafficking. *Cell* **174**, 1465-1476 e1413 (2018).

1214 46. B. Boland *et al.*, Promoting the clearance of neurotoxic proteins in neurodegenerative disorders of
1215 ageing. *Nat Rev Drug Discov* **17**, 660-688 (2018).

1216 47. S. A. Small, S. Simoes-Spassov, R. Mayeux, G. A. Petsko, Endosomal Traffic Jams Represent a
1217 Pathogenic Hub and Therapeutic Target in Alzheimer's Disease. *Trends Neurosci* **40**, 592-602
1218 (2017).

1219 48. V. J. Mecozzi *et al.*, Pharmacological chaperones stabilize retromer to limit APP processing. *Nat*
1220 *Chem Biol* **10**, 443-449 (2014).

1221 49. J. G. Li, J. Chiu, M. Ramanjulu, B. E. Blass, D. Pratico, A pharmacological chaperone improves
1222 memory by reducing Abeta and tau neuropathology in a mouse model with plaques and tangles. *Mol*
1223 *Neurodegener* **15**, 1 (2020).

1224 50. G. Lin *et al.*, Phospholipase PLA2G6, a Parkinsonism-Associated Gene, Affects Vps26 and Vps35,
1225 Retromer Function, and Ceramide Levels, Similar to alpha-Synuclein Gain. *Cell Metab* **28**, 605-618
1226 e606 (2018).

1227 51. J. E. Young *et al.*, Stabilizing the Retromer Complex in a Human Stem Cell Model of Alzheimer's
1228 Disease Reduces TAU Phosphorylation Independently of Amyloid Precursor Protein. *Stem Cell*
1229 *Reports* **10**, 1046-1058 (2018).

1230 52. N. K. Bashiruddin, H. Suga, Construction and screening of vast libraries of natural product-like
1231 macrocyclic peptides using in vitro display technologies. *Curr Opin Chem Biol* **24**, 131-138 (2015).

1232 53. C. J. Hipolito, H. Suga, Ribosomal production and in vitro selection of natural product-like
1233 peptidomimetics: the FIT and RaPID systems. *Curr Opin Chem Biol* **16**, 196-203 (2012).

1234 54. T. Passioura, H. Suga, A RaPID way to discover nonstandard macrocyclic peptide modulators of
1235 drug targets. *Chem Commun (Camb)* **53**, 1931-1940 (2017).

1236 55. H. Suga, Max-Bergmann award lecture:A RaPID way to discover bioactive nonstandard peptides
1237 assisted by the flexizyme and FIT systems. *J Pept Sci* **24**, (2018).

1238 56. D. Jia *et al.*, Structural and mechanistic insights into regulation of the retromer coat by TBC1d5. *Nat*
1239 *Commun* **7**, 13305 (2016).

1240 57. A. Hierro *et al.*, Functional architecture of the retromer cargo-recognition complex. *Nature* **449**,
1241 1063-1067 (2007).

1242 58. O. Kovtun *et al.*, Structure of the membrane-assembled retromer coat determined by cryo-electron
1243 tomography. *Nature* **561**, 561-564 (2018).

1244 59. M. Lucas *et al.*, Structural Mechanism for Cargo Recognition by the Retromer Complex. *Cell* **167**,
1245 1623-1635 e1614 (2016).

1246 60. S. J. Norwood *et al.*, Assembly and solution structure of the core retromer protein complex. *Traffic*
1247 **12**, 56-71 (2011).

1248 61. A. K. Kendall *et al.*, Mammalian Retromer Is an Adaptable Scaffold for Cargo Sorting from
1249 Endosomes. *Structure*, (2020).

1250 62. G. G. Hesketh *et al.*, VARP is recruited on to endosomes by direct interaction with retromer, where
1251 together they function in export to the cell surface. *Dev Cell* **29**, 591-606 (2014).

1252 63. H. Crawley-Snowdon *et al.*, Mechanism and evolution of the Zn-fingernail required for interaction
1253 of VARP with VPS29. *Nature Communications* **In Press**, (2020).

1254 64. H. Crawley-Snowdon *et al.*, Mechanism and evolution of the Zn-fingernail required for interaction
1255 of VARP with VPS29. *Nat Commun* **11**, 5031 (2020).

1256 65. D. Jia, T. S. Gomez, D. D. Billadeau, M. K. Rosen, Multiple repeat elements within the FAM21 tail
1257 link the WASH actin regulatory complex to the retromer. *Mol Biol Cell* **23**, 2352-2361 (2012).

1258 66. M. Gallon *et al.*, A unique PDZ domain and arrestin-like fold interaction reveals mechanistic details
1259 of endocytic recycling by SNX27-retromer. *Proc Natl Acad Sci U S A* **111**, E3604-3613 (2014).

1260 67. E. Helfer *et al.*, Endosomal recruitment of the WASH complex: active sequences and mutations
1261 impairing interaction with the retromer. *Biol Cell* **105**, 191-207 (2013).

1262 68. M. S. Harrison *et al.*, A mechanism for retromer endosomal coat complex assembly with cargo. *Proc*
1263 *Natl Acad Sci U S A* **111**, 267-272 (2014).

1264 69. P. V. Hornbeck *et al.*, PhosphoSitePlus, 2014: mutations, PTMs and recalibrations. *Nucleic Acids*
1265 *Res* **43**, D512-520 (2015).

1266 70. A. Bugarcic *et al.*, Vps26A and Vps26B subunits define distinct retromer complexes. *Traffic* **12**,
1267 1759-1773 (2011).

1268 71. K. W. Teng *et al.*, Labeling proteins inside living cells using external fluorophores for microscopy.
1269 *Elife* **5**, (2016).

1270 72. M. E. Harbour *et al.*, The cargo-selective retromer complex is a recruiting hub for protein complexes
1271 that regulate endosomal tubule dynamics. *J Cell Sci* **123**, 3703-3717 (2010).

1272 73. A. Alex *et al.*, Electroporated recombinant proteins as tools for in vivo functional complementation,
1273 imaging and chemical biology. *Elife* **8**, (2019).

1274 74. K. Patel *et al.*, Cyclic peptides can engage a single binding pocket through multiple, entirely
1275 divergent modes. *Biorxiv* **Epub**, (2019).

1276 75. K. E. McNally *et al.*, Retriever is a multiprotein complex for retromer-independent endosomal cargo
1277 recycling. *Nat Cell Biol* **19**, 1214-1225 (2017).

1278 76. S. Banos-Mateos, A. L. Rojas, A. Hierro, VPS29, a tweak tool of endosomal recycling. *Curr Opin*
1279 *Cell Biol* **59**, 81-87 (2019).

1280 77. N. Leneva, O. Kovtun, D. R. Morado, J. A. G. Briggs, D. J. Owen, Architecture and mechanism of
1281 metazoan retromer:SNX3 tubular coat assembly. *Sci Adv* **7**, (2021).

1282 78. B. M. Collins *et al.*, Structure of Vps26B and mapping of its interaction with the retromer protein
1283 complex. *Traffic* **9**, 366-379 (2008).

1284 79. M. C. Kerr *et al.*, A novel mammalian retromer component, Vps26B. *Traffic* **6**, 991-1001 (2005).

1285 80. F. M. Menzies *et al.*, Autophagy and Neurodegeneration: Pathogenic Mechanisms and Therapeutic
1286 Opportunities. *Neuron* **93**, 1015-1034 (2017).

1287 81. W. H. Toh, P. A. Gleeson, Dysregulation of intracellular trafficking and endosomal sorting in
1288 Alzheimer's disease: controversies and unanswered questions. *Biochem J* **473**, 1977-1993 (2016).

1289 82. P. Zhang, R. Moreno, P. F. Lambert, D. DiMaio, Cell-penetrating peptide inhibits retromer-mediated
1290 human papillomavirus trafficking during virus entry. *Proc Natl Acad Sci U S A*, (2020).

1291 83. J. Chu, D. Pratico, The retromer complex system in a transgenic mouse model of AD: influence of
1292 age. *Neurobiol Aging* **52**, 32-38 (2017).

1293 84. V. Singh *et al.*, Cholera toxin inhibits SNX27-retromer-mediated delivery of cargo proteins to the
1294 plasma membrane. *J Cell Sci* **131**, (2018).

1295 85. A. N. Vagnozzi *et al.*, VPS35 regulates tau phosphorylation and neuropathology in tauopathy. *Mol*
1296 *Psychiatry*, (2019).

1297 86. S. Eleuteri, A. Albanese, VPS35-Based Approach: A Potential Innovative Treatment in Parkinson's
1298 Disease. *Front Neurol* **10**, 1272 (2019).

1299 87. D. Ringe, G. A. Petsko, What are pharmacological chaperones and why are they interesting? *J Biol*
1300 **8**, 80 (2009).

1301 88. T. A. Cardote, A. Ciulli, Cyclic and Macrocyclic Peptides as Chemical Tools To Recognise Protein
1302 Surfaces and Probe Protein-Protein Interactions. *ChemMedChem* **11**, 787-794 (2016).

1303 89. Z. Qian, P. G. Dougherty, D. Pei, Targeting intracellular protein-protein interactions with cell-
1304 permeable cyclic peptides. *Curr Opin Chem Biol* **38**, 80-86 (2017).

1305 90. A. Zorzi, K. Deyle, C. Heinis, Cyclic peptide therapeutics: past, present and future. *Curr Opin Chem*
1306 *Biol* **38**, 24-29 (2017).

1307 91. A. A. Vinogradov, Y. Yin, H. Suga, Macrocyclic Peptides as Drug Candidates: Recent Progress and
1308 Remaining Challenges. *J Am Chem Soc* **141**, 4167-4181 (2019).

1309 92. D. S. Nielsen *et al.*, Orally Absorbed Cyclic Peptides. *Chem Rev* **117**, 8094-8128 (2017).

1310 93. J. M. Rogers, T. Passioura, H. Suga, Nonproteinogenic deep mutational scanning of linear and cyclic
1311 peptides. *Proc Natl Acad Sci U S A* **115**, 10959-10964 (2018).

1312 94. L. J. Walport, R. Obexer, H. Suga, Strategies for transitioning macrocyclic peptides to cell-
1313 permeable drug leads. *Curr Opin Biotechnol* **48**, 242-250 (2017).

1314 95. R. D. Teasdale, D. Loci, F. Houghton, L. Karlsson, P. A. Gleeson, A large family of endosome-
1315 localized proteins related to sorting nexin 1. *Biochem J* **358**, 7-16 (2001).

1316 96. B. M. Collins, C. F. Skinner, P. J. Watson, M. N. Seaman, D. J. Owen, Vps29 has a phosphoesterase
1317 fold that acts as a protein interaction scaffold for retromer assembly. *Nat Struct Mol Biol* **12**, 594-
1318 602 (2005).

1319 97. R. Ghai *et al.*, Phosphoinositide binding by the SNX27 FERM domain regulates its localization at
1320 the immune synapse of activated T-cells. *J Cell Sci* **128**, 553-565 (2015).

1321 98. T. Clairfeuille *et al.*, A molecular code for endosomal recycling of phosphorylated cargos by the
1322 SNX27-retromer complex. *Nat Struct Mol Biol* **23**, 921-932 (2016).

1323 99. K. W. Teng *et al.*, Labeling Proteins Inside Living Cells Using External Fluorophores for
1324 Fluorescence Microscopy. *Elife* **6**, (2017).

1325 100. Y. Cui *et al.*, Retromer has a selective function in cargo sorting via endosome transport carriers. *J*
1326 *Cell Biol* **218**, 615-631 (2019).

1327 101. W. Kabsch, Xds. *Acta Crystallogr D Biol Crystallogr* **66**, 125-132 (2010).

1328 102. P. R. Evans, G. N. Murshudov, How good are my data and what is the resolution? *Acta Crystallogr*
1329 *D Biol Crystallogr* **69**, 1204-1214 (2013).

1330 103. A. J. McCoy *et al.*, Phaser crystallographic software. *J Appl Crystallogr* **40**, 658-674 (2007).

1331 104. P. D. Adams *et al.*, PHENIX: a comprehensive Python-based system for macromolecular structure
1332 solution. *Acta Crystallogr D Biol Crystallogr* **66**, 213-221 (2010).

1333 105. V. B. Chen *et al.*, MolProbity: all-atom structure validation for macromolecular crystallography.
1334 *Acta Crystallogr D Biol Crystallogr* **66**, 12-21 (2010).

1335 106. C. Notredame, D. G. Higgins, J. Heringa, T-Coffee: A novel method for fast and accurate multiple
1336 sequence alignment. *J Mol Biol* **302**, 205-217 (2000).

1337 107. H. Ashkenazy *et al.*, ConSurf 2016: an improved methodology to estimate and visualize
1338 evolutionary conservation in macromolecules. *Nucleic Acids Res* **44**, W344-350 (2016).

1339 108. L. Holm, P. Rosenstrom, Dali server: conservation mapping in 3D. *Nucleic Acids Res* **38**, W545-549
1340 (2010).

1341 109. B. Carragher *et al.*, Leginon: An automated system for acquisition of images from vitreous ice
1342 specimens. *Journal of Structural Biology* **132**, 33-45 (2000).

1343 110. K. Zhang, Gctf: Real-time CTF determination and correction. *J Struct Biol* **193**, 1-12 (2016).

1344 111. J. Zivanov *et al.*, New tools for automated high-resolution cryo-EM structure determination in
1345 RELION-3. *Elife* **7**, (2018).

1346 112. E. F. Pettersen *et al.*, UCSF Chimera--a visualization system for exploratory research and analysis. *J*
1347 *Comput Chem* **25**, 1605-1612 (2004).

1348 113. K. E. Chen, V. A. Tillu, M. Chandra, B. M. Collins, Molecular Basis for Membrane Recruitment by
1349 the PX and C2 Domains of Class II Phosphoinositide 3-Kinase-C2alpha. *Structure* **26**, 1612-1625
1350 e1614 (2018).
1351

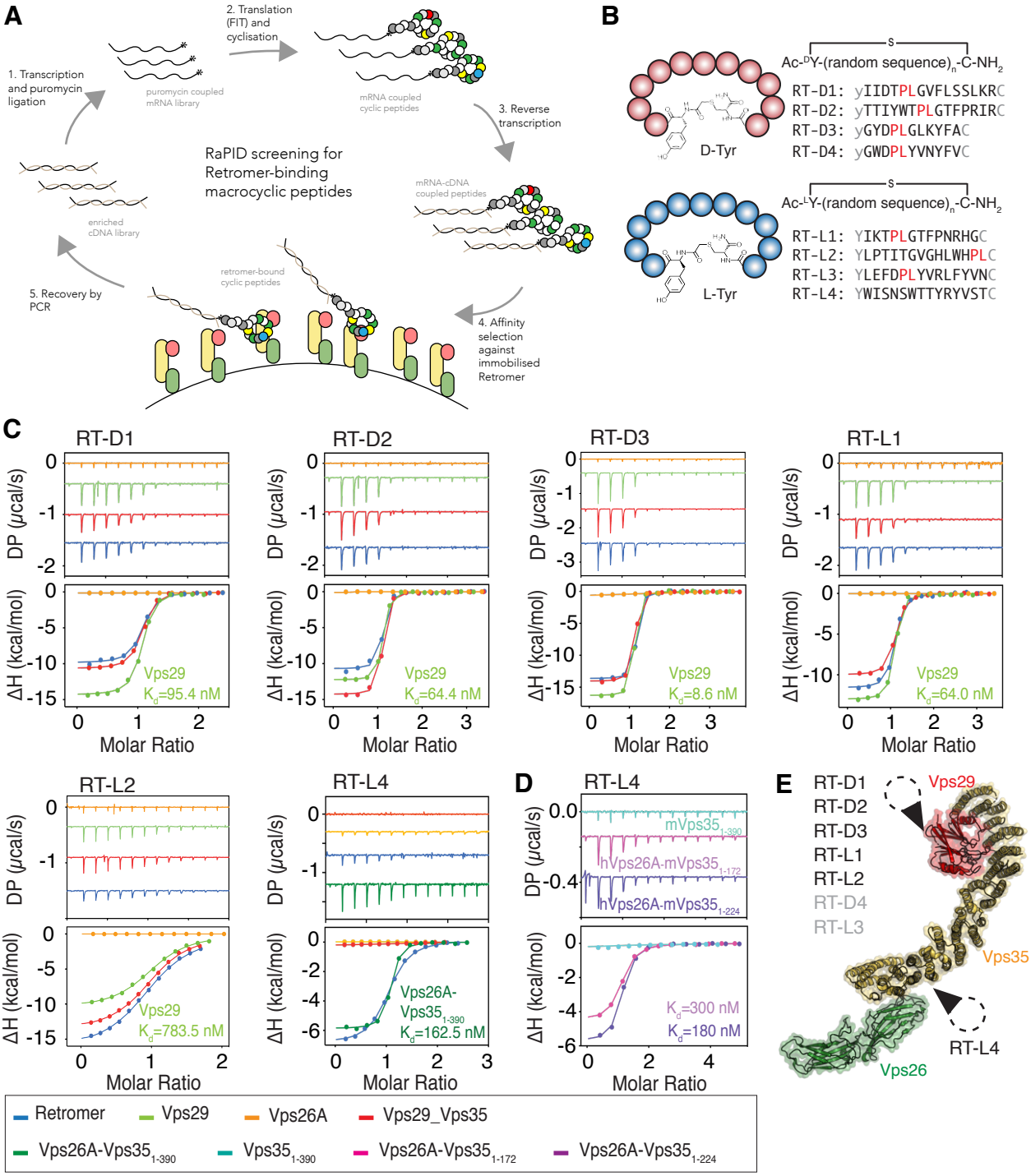

Figure 1. Cyclic peptides reveal strong binding characteristics with Retromer.
(A) Schematic diagram showing the RaPID system used to screen for cyclic peptides binding to Retromer. (B) Eight Retromer-binding macrocyclic peptides were identified with either N-chloroacetyl-D-tyrosine or N-chloroacetyl-L-tyrosine as initiating residues. (C) Binding of RT-D1, RT-D2, RT-D3, RT-L1, RT-L2, and RT-L4 with Retromer (blue), Vps29 (light green), Vps26A (orange), Vps29 – Vps35 (red) and Vps26A – Vps351-390 (dark green) by ITC. SPR binding curves for each peptide are shown in Fig. S3. (D) ITC thermogram showing that addition of α-helix 8 and 9 of Vps35 (residues 173 to 224) contributes to RT-L4 binding affinity but is not essential for interaction. All ITC graphs represent the integrated and normalized data fit with 1 to 1 ratio binding. The binding affinity (Kd) is given as mean of at least three independent experiments (Table S2). (E) Relative binding position of each cyclic peptide to Retromer based on the ITC measurements indicated on the structure of the mouse Retromer complex (PDB ID 6VAC) (61).

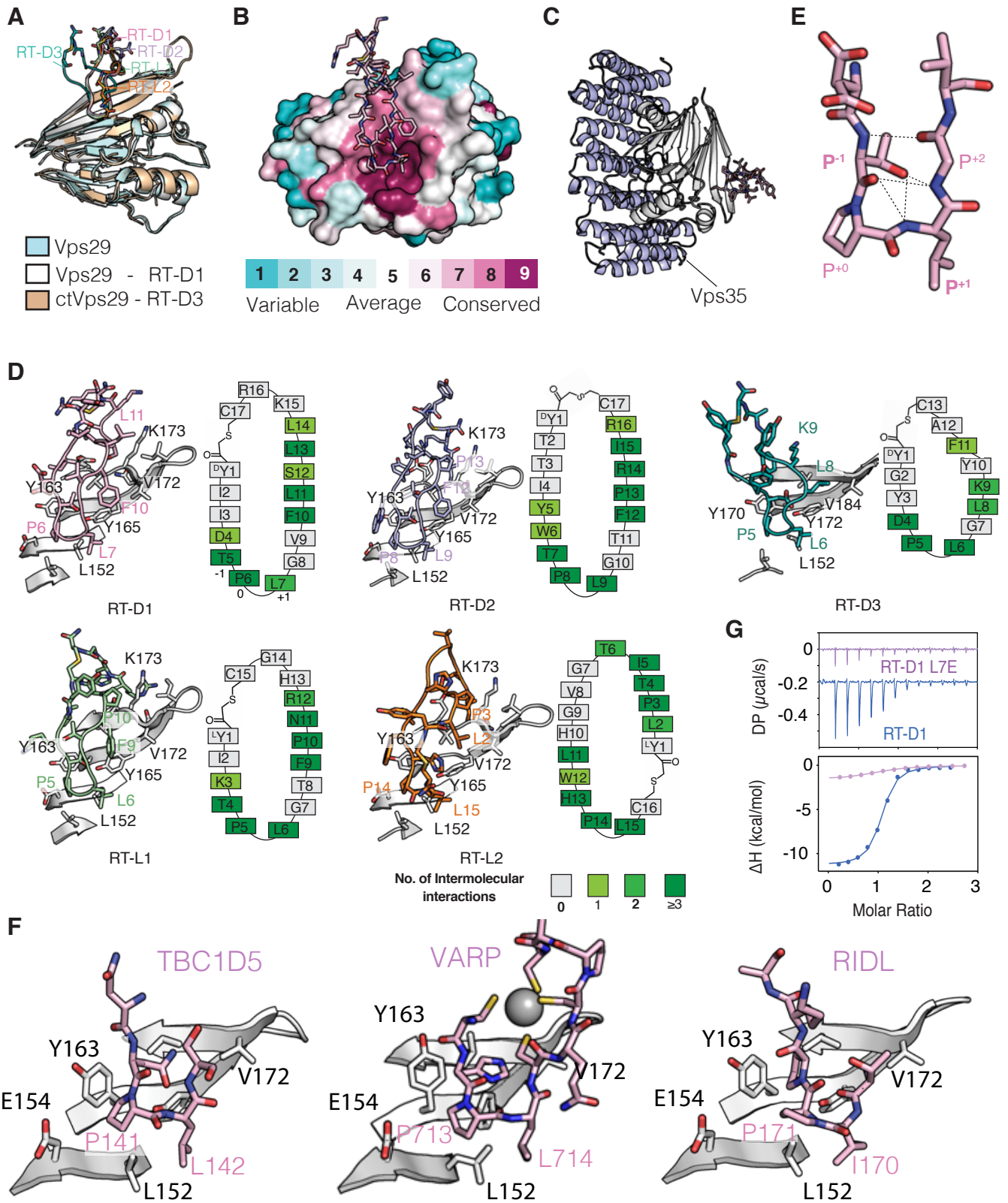

Figure 2. Crystal structures of Vps29 in complex with cyclic peptides.
(A) Superimposition of the crystal structures of Vps29 in complex with five macrocyclic peptides. (B) Sequence conservation mapped onto the hVPS29 structure surface highlights the conserved binding site for each of the cyclic peptides, with RT-D1 shown as an example. (C) Superimposition of the Vps29 – RT-D1 peptide complex with the Vps29 - Vps35483-780 crystal structure (PDB ID: 2R17) (57). The cyclic peptides bind opposite to the Vps35 interface. (D) Details of macrocyclic peptides in stick representation bound to Vps29. Schematic diagrams indicate the number of intermolecular contacts (salt bridge, hydrogen bonds and hydrophobic interactions) of each residue on the peptide with Vps29. The residues on the peptide with 0, 1, 2 and ≥3 contacts are shown in grey, light green, green and dark green boxes respectively. Each peptide utilises a core Pro-Leu sequence forming a -hairpin, labelled as position 0 and 1 for reference. Electron density for each peptide is shown in Fig. S3. (E) Close-up of the -hairpin conformation of the bound RT-D1 peptide. (F) TBC1D5 (PDB ID 5GTU) (56), VARP (PDB ID 6TL0) (64) and RIDL (PDB ID 5OSH) (43) bind to the same site of Vps29 using a similar -hairpin comprised of a Pro-Leu dipeptide sequence. For clarity, only the key residues involve in the contact are shown. (G) ITC thermogram for the titration of RT-D1 (purple) and RT-D1 L7E (blue) with Retromer showing the importance of Pro-Leu motif in the interaction. The graph represents the integrated and normalized data fit with a 1 to 1 binding ratio.

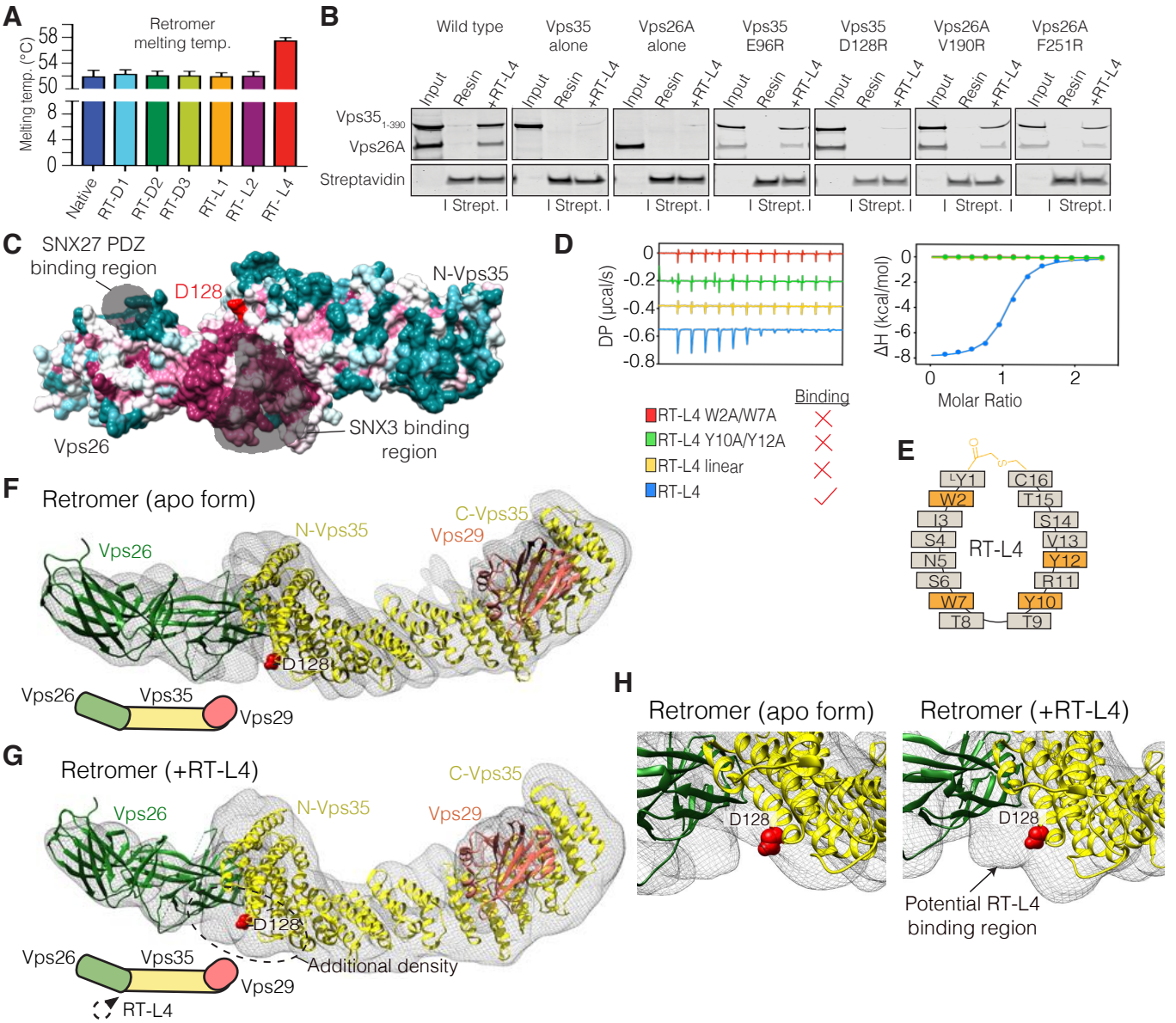

Figure 3. The RT-L4 macrocylic peptide is a molecular chaperone that binds Retromer at the Vps35-Vps26 interface.
(A) Bar graph summarizing the measured thermal unfolding temperatures (Tm) of Retromer in the presence of cyclic peptides. Raw data is shown in Fig. S4. (B) Pull-down assay showing the interaction of biotinylated RT-L4 bound to streptavidin-coated agarose beads with either wild-type Vps26A-Vps351-390 subcomplex or indicated point mutants. Individual Vps26A and Vps351-390 proteins do not bind the peptide, while the D128R mutation in Vps351-390 specifically blocks sub-complex interaction. (C) Sequence conservation map of Vps26A-Vps3512-470 subcomplex (PDB ID 5F0L) highlighting the proposed RT-L4 binding site, and its relationship to known binding sites for SNX3 (59) and SNX27 (66). (D) ITC thermograms showing that linear RT-L4, or RT-L4 with alterations in bulky aramotic sidechains is unable to bind to Retromer. The graph represents the integrated and normalized data fit with a 1 to 1 binding ratio. (E) Schematic diagram of RT-L4 highlighting aromatic residues important for binding to Retromer. (F) CryoEM reconstruction of the human Retromer (apo form) and (G) in complex with RT-L4. CryoEM density shown as transparent molecular envelope, with crystal structures of Retromer subcomplexes (PDB ID 2R17 and 5F0L) overlapped to the map (contoured at 4.7σ). The additional density seen on addition of the cyclic peptide added Retromer supports the mutagenesis data indicating RT-L4 binds at the Vps26 and Vps35 interface. (H) Enlarged view of the Vps26 and Vps35 interface highlighting the additional density in the CryoEM map of RT-L4 added Retromer but not in the apo form. For clarity, D128 of Vps35 is highlighted in red.

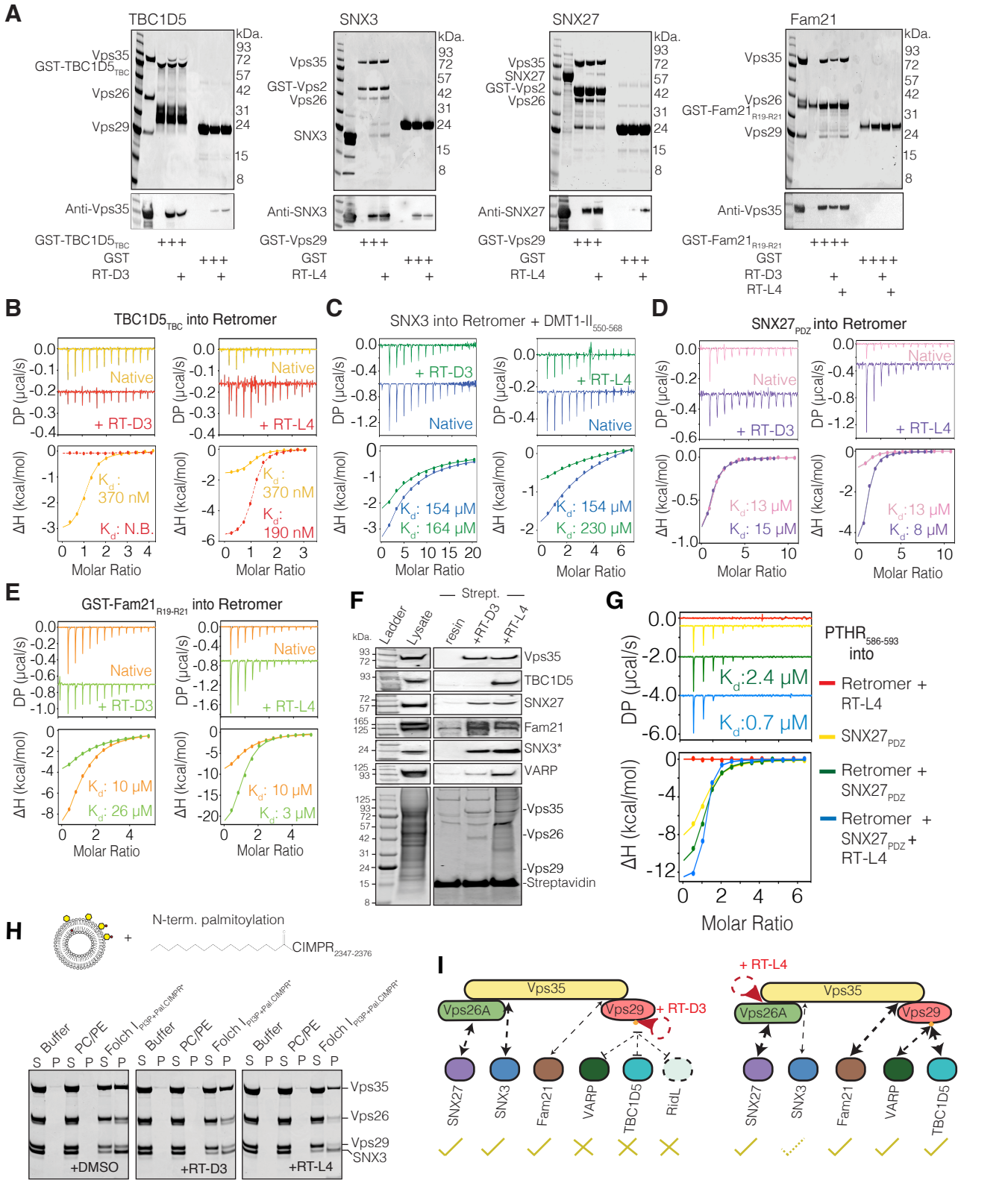

Figure 4. The effect of cyclic peptides on the interaction of Retromer with known regulatory and adaptor proteins.
(A) Interactions of Retromer with TBC1D5, SNX3, SNX27 and Fam21 in the presence of either RT-D3 or RT-L4. GST-TBC1D5TBC and GST-Fam21R19-R21 were used as baits for Retromer, while GST-tagged Retromer (Vps29 subunit) was used as bait for SNX3 and SNX27. (B) ITC measurement of TBC1D5TBC, (C) SNX3 (with DMT1-II550-568 present), (D) SNX27, and (E) GST-Fam21R19-R21 with Retromer in the presence or absence of RT-D3 or RT-L4. (F) Hela cell lysates were incubated with streptavidin agarose coated with biotinylated RT-D3 or RT-L4 and bound proteins subjected to SDS-PAGE and western blotting with antibodies against indicated proteins. (G) ITC measurement of PTHR586-593 cargo peptide (98) with SNX27PDZ alone (yellow), Retromer + RT-L4 (red), Retromer + SNX27PDZ (green) and Retromer + SNX27PDZ + RT-L4 (blue). RT-L4 allosterically enhances the affinity of Retromer + SNX27PDZ for cargo. The cargo peptide binds to SNX27 All ITC graphs represent the integrated and normalized data fit with a 1 to 1 binding ratio. The binding affinity (Kd) is given as mean of at least two independent experiments. (H) Liposome-binding assay of Retromer with membrane-associated SNX3 cargo complex in the presence of cyclic peptides. Multilamellar vesicles were composed of either control PC/PE lipids, or Folch I lipids containing added PtdIns(3)P and N-terminal palmitoylated CIMPR2347-2376 peptide (schematic diagram on top). “S” and “P” indicates unbound supernatant and bound pellet respectively. Control experiments are shown in Fig. S7B and S7C. (I) Schematic summarizing the effects of RT-D3 and RT-L4 on Retromer engagement with known regulatory, adaptor and bacterial effector proteins.

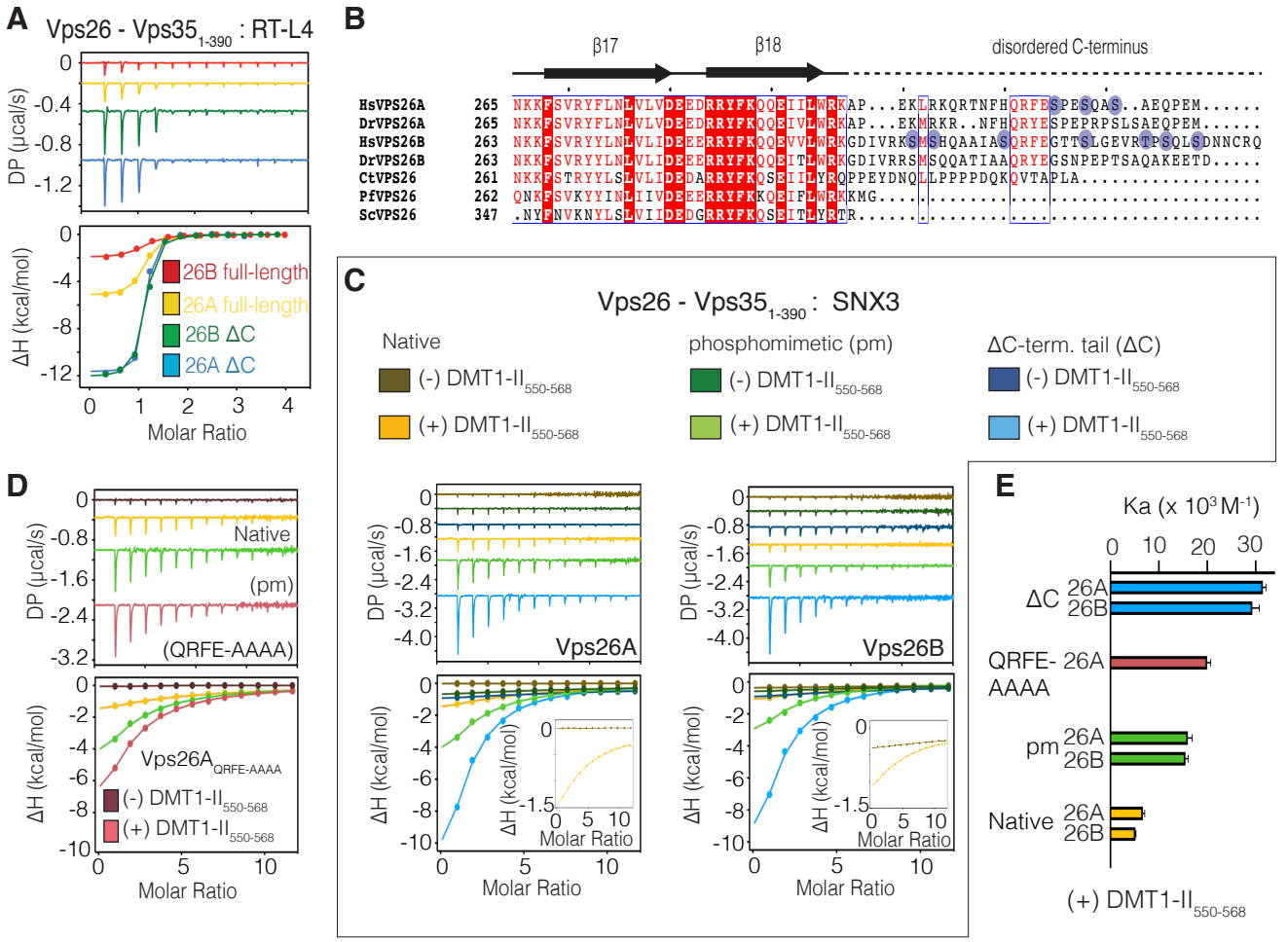

Figure 5. An autoinhibitory role for the disordered C-terminal tail of Vps26 in binding RT-L4 and SNX3.
(A) ITC thermogram for the titration of RT-L4 with Vps351-390 sub-complex with either full-length or C-terminal truncated Vps26A and Vps26B paralogues. (B) Sequence alignment of the C-terminal region of Vps26 highlighting the low-sequence similarity of the unstructured C-terminal tail apart from the QRF/YE motif highlighted with a blue square. Sites of phosphorylation are indicated in circle (www.phosphosite.org) (69). Hs, Homo sapiens; Dr, Danio rerio; Ct, Chaetomium thermophilum; Pf, Plasmodium falciparum, Sc, Saccharomyces cerevisiae. (C) ITC measurement of SNX3 binding to native, phosphomimetic (pm), and C-terminal tail truncated (ΔC) versions of Vps26A/B – Vps351-390 subcomplexes. In each case, the presence of DMT1-II cargo peptide was required to detect SNX3 binding. (D) ITC measurement of SNX3 binding to QRFE-AAAA mutant Vps26A – Vps351-390. ITC thermograms in (A), (C) and (D) represent the integrated and normalized data fit with a 1 to 1 binding ratio. (E) Summary of binding affinities of SNX3 for each Vps26A/B – Vps351-390 subcomplex in the presence of DMT1-II550-568 cargo peptide. For clarity, the association constant (Kd¬-1) is shown. The binding affinity is given as mean of at least two independent experiments.

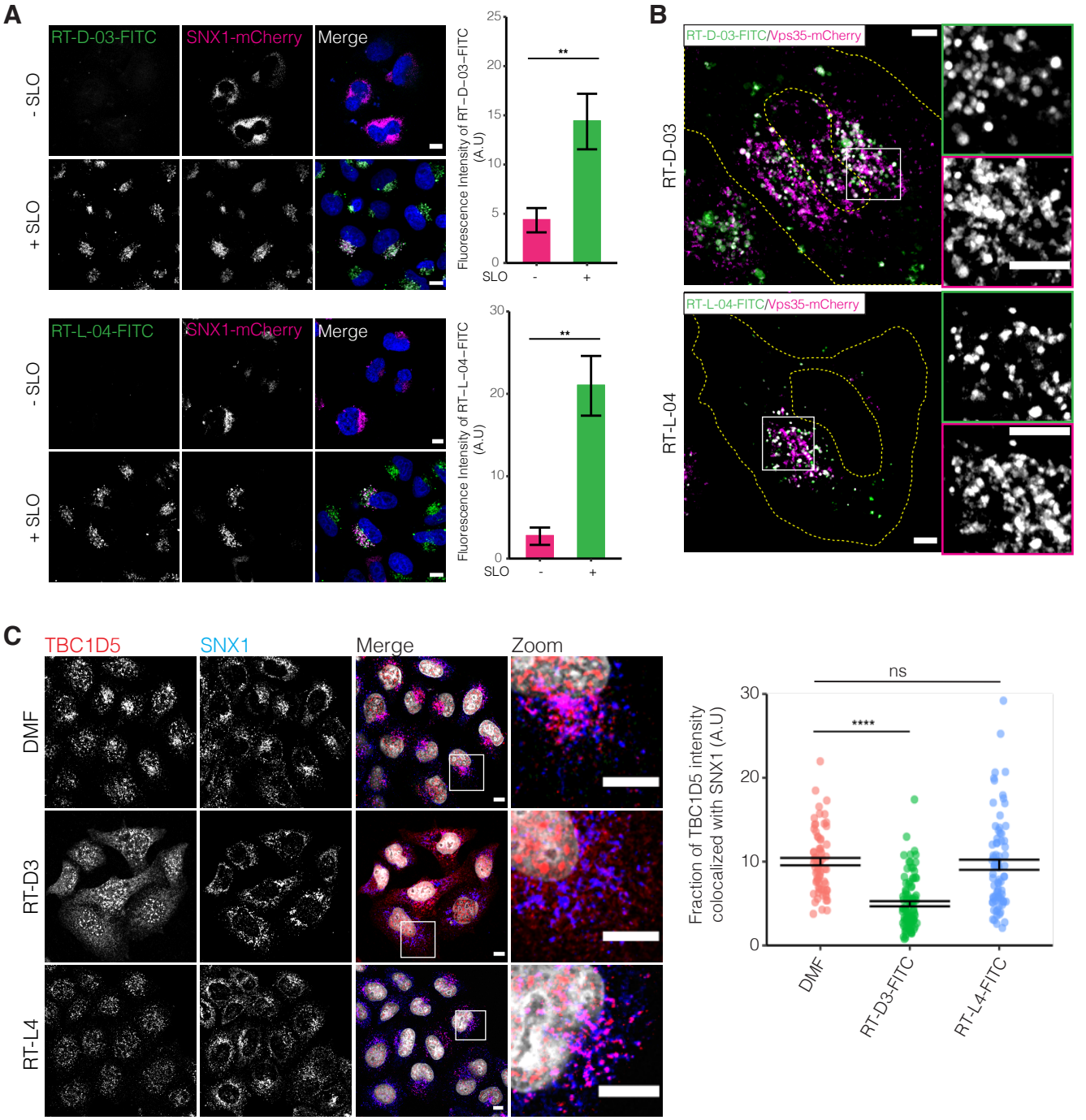

Figure 6. Macrocyclic peptides can be used to study Retromer localization in cells.
(A) Specific targeting of endosomal structures by streptolysin O (SLO) delivered cyclic peptides. HeLa cells transiently expressing SNX1-mCherry were exposed to SLO at 37°C for 9 min before incubating with the cyclic peptide RT-D3-FITC or RT-L4-FITC on ice for 5 min. Permeabilized cells were recovered in the recovery medium containing Hoechst 33342 for 20 min, then fixed in 4% PFA. The negative control (-SLO) shows no labeling of intracellular structures. Scale bar, 10 µm. Graphs show the fluorescence intensity of RT-D3-FITC or RT-L4-FITC in HeLa cells (means ± SEM). Two-tailed Student's t-test was used to determine the statistical significance (n=3). **, $P < 0.01$. (B) HeLa cells transiently expressing Vps35-mCherry were labeled by SLO-delivered cyclic peptide RT-D3-FITC or RT-L4-FITC, fixed in 4% PFA, and imaged by Airyscan super-resolution microscopy. Scale bar, 5 µm. (C) HeLa cells treated with SLO-delivered RT-D3-FITC, RT-L4-FITC, or DMF control were incubated in recovery medium for 2 h, fixed in ice-cold methanol, and co-immunolabeled with antibodies against endogenous TBC1D5 and SNX1, followed by Alexa Fluor-conjugated fluorescent secondary antibodies. Scale bar, 10 µm. The colocalization between TBC1D5 and SNX1 was quantified by Pearson's correlation coefficient and represented in the graph (means ± SEM). Two-tailed Student's t-test was utilized to determine the statistical significance (n=3). ****, $P < 0.0001$; ns, not significant.

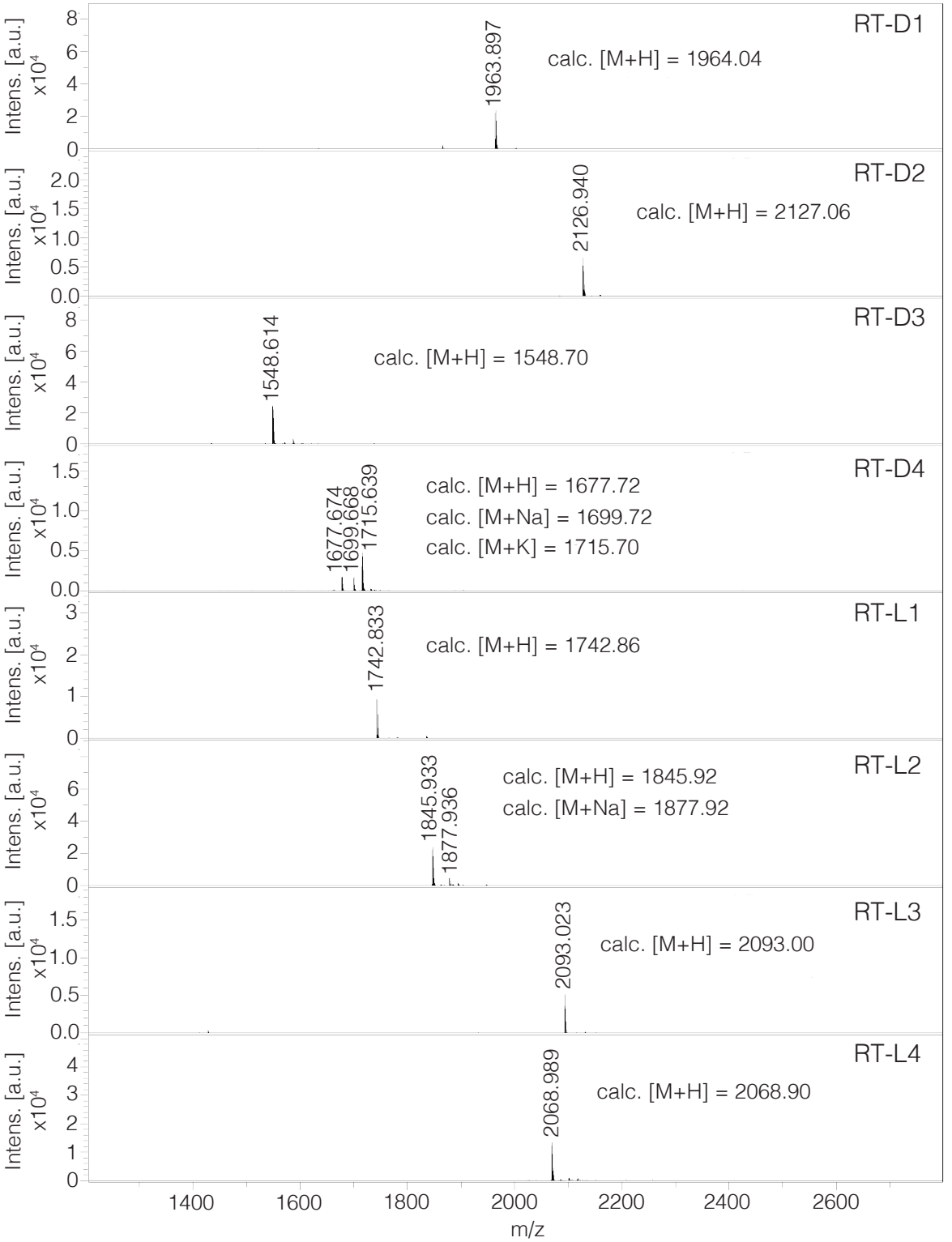

Figure S1. MALDI-TOF spectra of the Retromer associated cyclic peptides.
The molecular mass of RT-D1, RT-D2, RT-D3, RT-D4, RT-L1, RT-L2, RT-L3 and RT-L4 are shown in the spectrum.

A

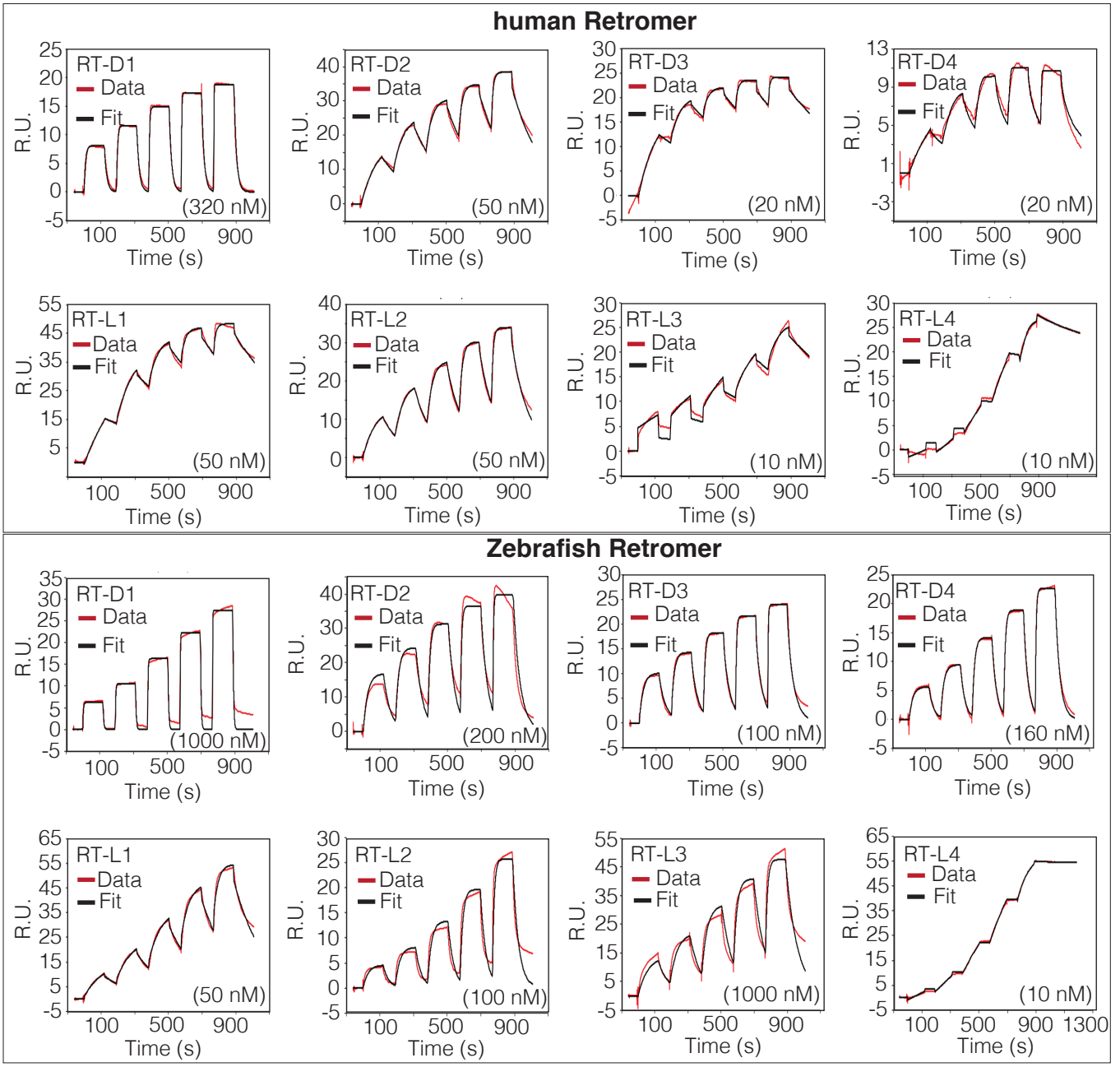

B

hRetromer

	K_{on} ($M^{-1}.S^{-1}$)	K_{off} (S^{-1})	K_D (nM)
RT-D1	2.25×10^6	0.070	31
RT-D2	1.82×10^6	0.005	2.9
RT-D3	6.57×10^6	0.002	0.3
RT-D4	1.79×10^{10}	18.43	1.0
RT-L1	1.54×10^6	0.002	1.4
RT-L2	2.02×10^6	0.010	5.2
RT-L3	1.52×10^6	0.002	1.1
RT-L4	4.91×10^6	0.001	0.2

zRetromer

	K_{on} ($M^{-1}.S^{-1}$)	K_{off} (S^{-1})	K_D (nM)
RT-D1	8.61×10^5	0.253	294
RT-D2	1.24×10^6	0.025	20
RT-D3	3.38×10^6	0.029	8.6
RT-D4	9.03×10^5	0.036	40
RT-L1	6.52×10^5	0.005	8.2
RT-L2	6.71×10^5	0.030	45
RT-L3	7.15×10^4	0.014	198
RT-L4	1.50×10^6	< 0.001	< 0.1

C

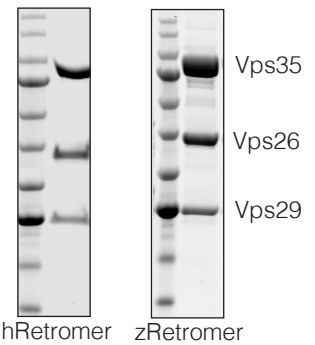

Figure S2. Preliminary SPR binding kinetics of Retromer-associated cyclic peptides.
(A) Single cycle kinetics experiments were performed using SPR with His-tagged human or zebrafish Retromer with varying concentrations of cyclic peptides. In each case, 2-fold serial dilutions of peptide were tested starting from a highest concentration of 200 or 1000 nM as indicated. (B) Binding kinetics of macrocyclic peptides for human and zebrafish Retromer complexes as determined by SPR. (C) Gels showing purity of human and zebrafish Retromer complexes used for Rapid peptide screening and SPR experiments.

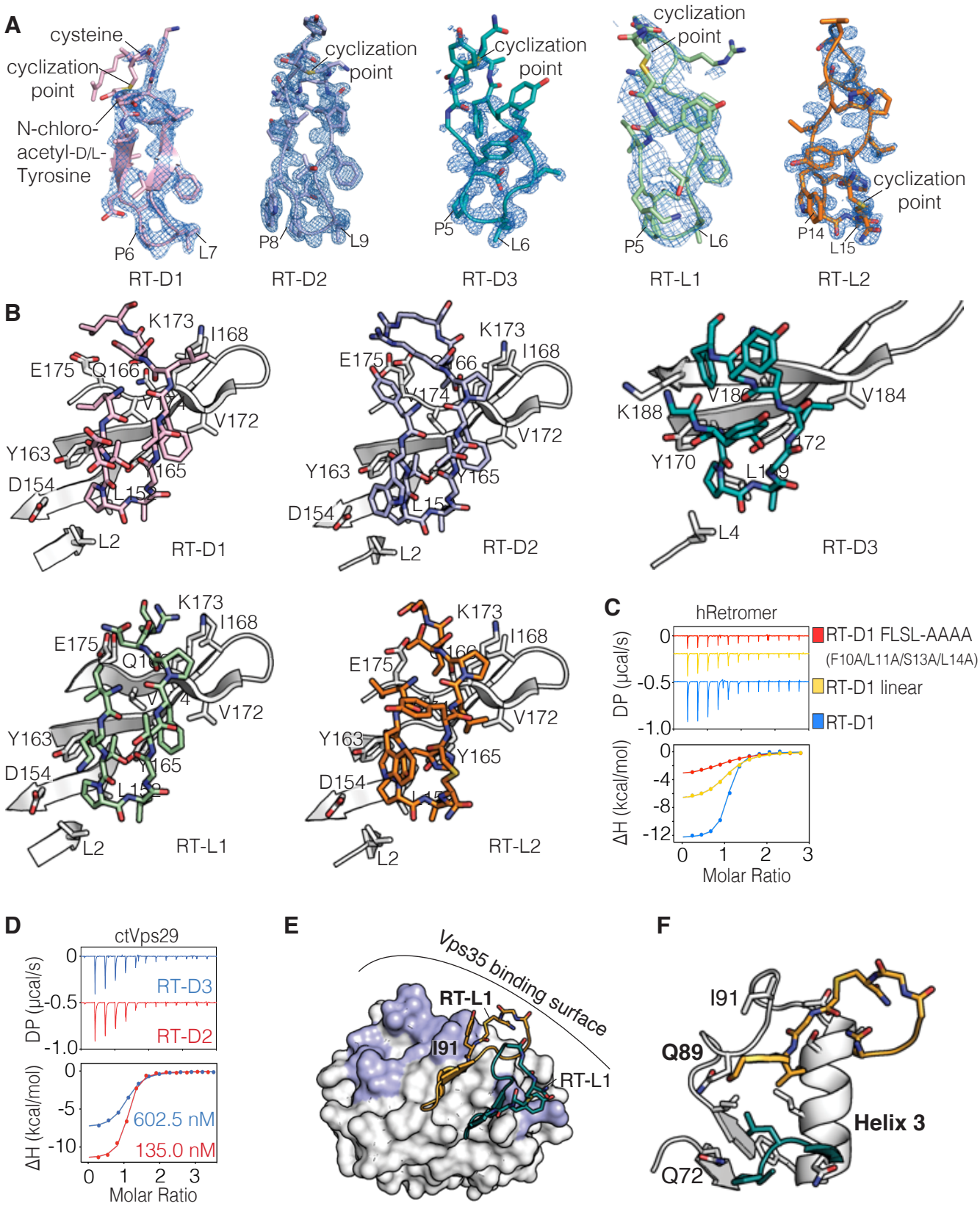

Figure S3. Interaction analysis of Vps29 and cyclic peptides.
(A) Structures of the Vps29 bound cyclic peptides, RT-D1, RT-D2, RT-D3, RT-L1 and RT-L2. For clarity, the main chain backbones are shown in ribbon and side chains are shown in stick form. The electron density shown corresponds to a simulated-annealing OMIT Fo - Fc map contoured at 3σ. (B) Highlighted details of the residues involved in the interactions between Vps29 and bound macrocyclic peptides. (C) ITC thermogram showing that both linear and mutant form of RT-D1 binds weakly to Retromer. (D) ITC titration of RT-D2 (red line) and RT-D3 (blue line) with ctVps29. Both graphs represent the integrated and normalized data fit with a 1 to 1 binding ratio. The binding affinity (Kd) is given as mean of three independent experiments. (E) Surface and (F) cartoon representations of the human Vps29 – RT-L1 structure highlighting the secondary binding site located opposite to the primary common binding site. Residues involve in contact with Vps35 are shown in light blue.

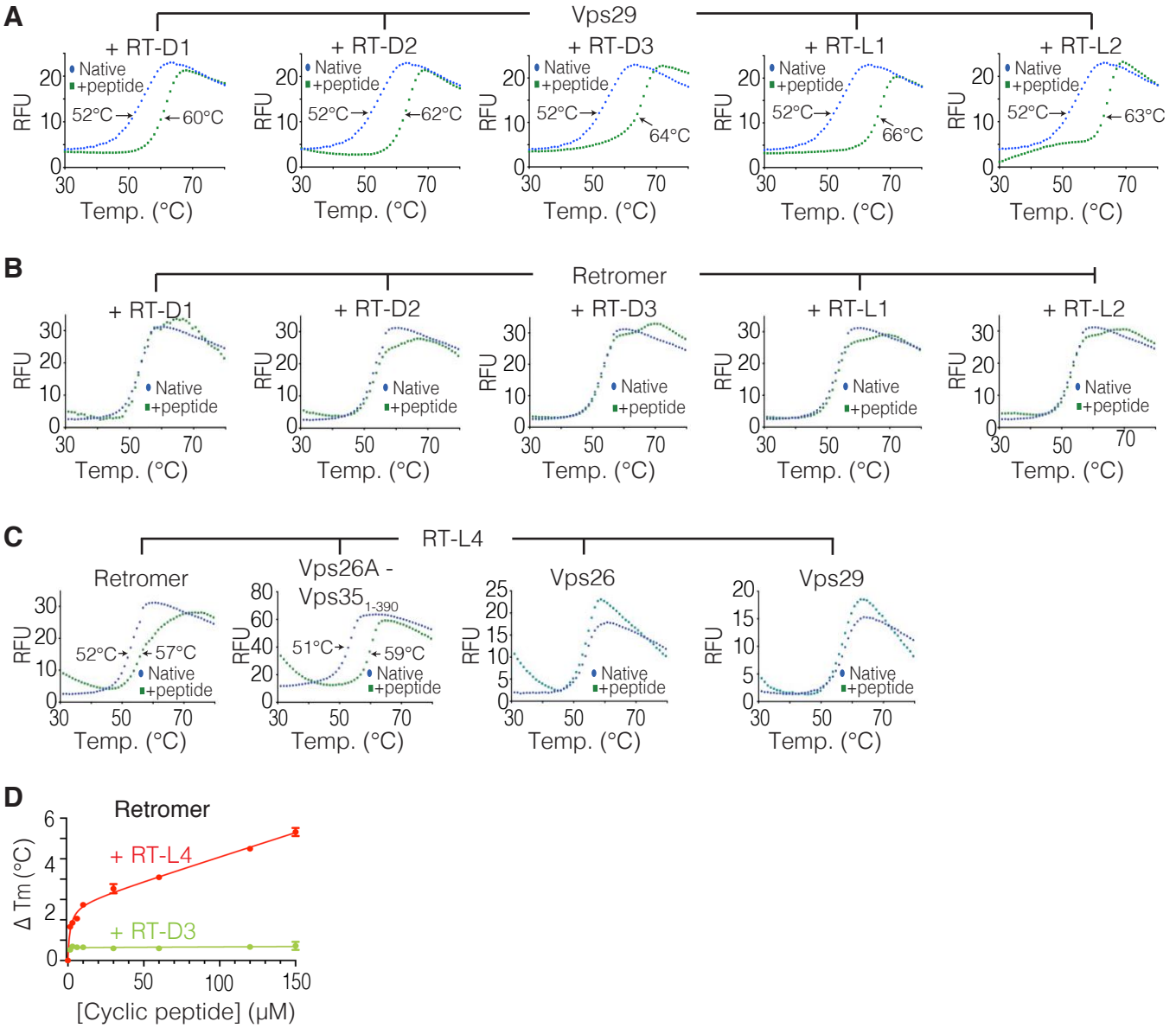

Figure S4. RT-L4 enhances the thermal stability of Retromer in solution.
(A) Temperature dependent unfolding of Vps29 in the presence of 30-fold molar excess of RT-D1, RT-D2, RT-D3, RT-L1 and RT-L2. (B) Temperature dependent unfolding of native Retromer in the presence of 30-fold molar excess of RT-D1, RT-D2, RT-D3, RT-L1 and RT-L2 complexes, and (C) in the presence of 30-fold molar excess of RT-L4. Melting temperatures (Tm) were assessed by differential scanning fluorimetry. The sigmoidal curve is characteristic of cooperative thermal denaturation of a folded protein. A shift in melting temperature indicates the stabilization of the proteins upon the addition of cyclic peptide. (D) Dose-response curve of Retromer in the presence of RT-L4 (red line) or RT-D3 (green line).

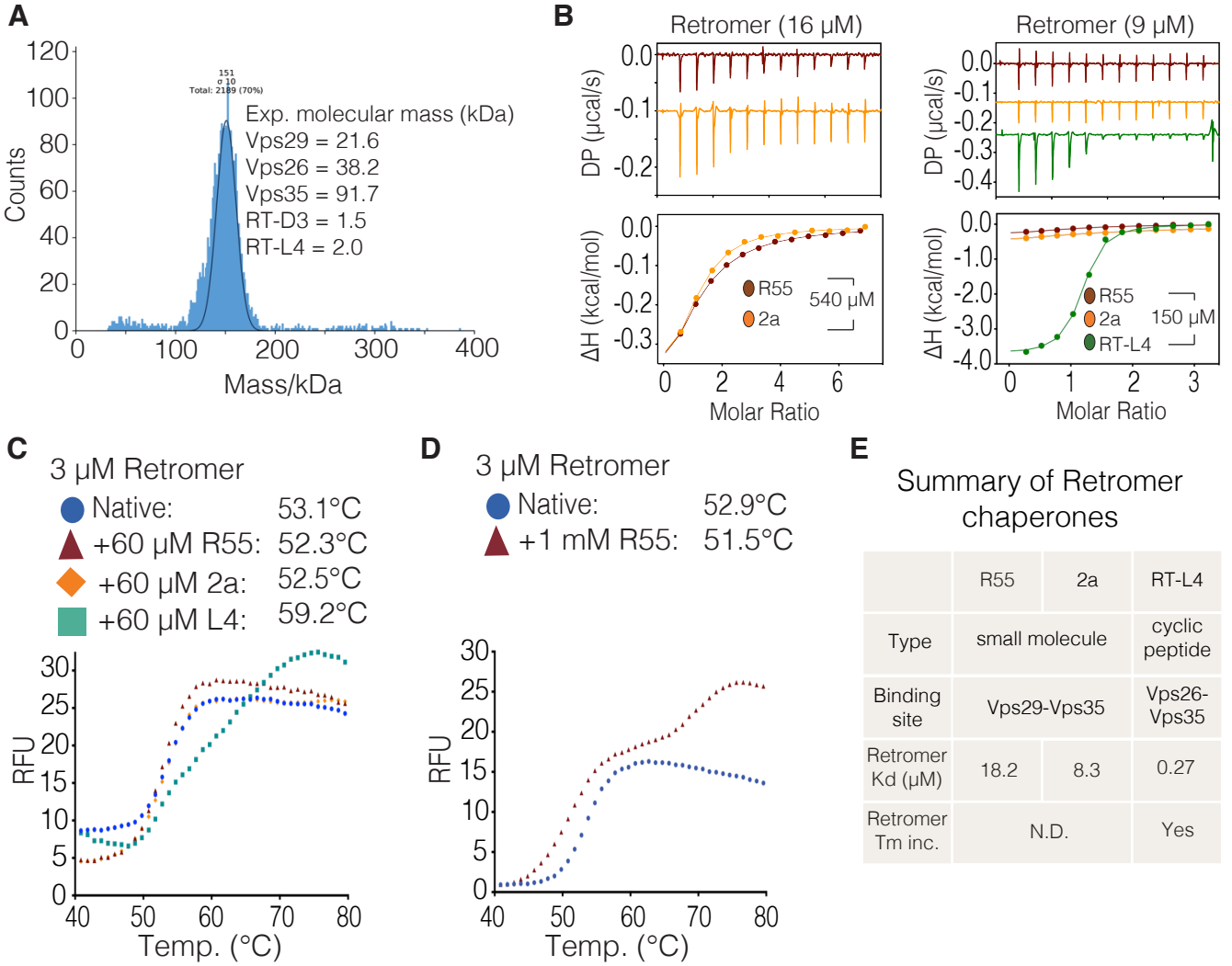

	R55	2a	RT-L4
Type	small molecule		cyclic peptide
Binding site	Vps29-Vps35		Vps26-Vps35
Retromer Kd (μM)	18.2	8.3	0.27
Retromer Tm inc.	N.D.		Yes

Figure S5. R55 does not significantly increase the thermal-stability of Retromer.
(A) Molecular mass of Retromer in the presence of RT-D3 and RT-L4 monitored by mass photometry. In this experiment, Retromer shows a mass of 151 kDa, corresponding to the heterotrimeric state of Retromer. (B) ITC thermogram for the titration of R55, compound 2a and RT-L4 with Retromer under two different concentrations. Both graphs represent the integrated and normalized data fit with a 1 to 1 binding ratio. The binding affinity (Kd) is given as mean of three independent experiments. (C) Temperature dependent unfolding of 3 M Retromer (blue dot) compared with samples containing 60 μM of R55 (brown triangle), 60 μM compound 2a (orange rhombus) or 60 μM RT-L4 (green square). (D) Same as (C) but with 1 mM of R55 showing two stages of unfolding. Note that preparation of 1 mM compound 2a and RT-L4 in aqueous buffer was not possible due solubility characteristics. (E) Summary of Retromer binding properties and thermal-stability effect of molecular chaperones R55, compound 2a and RT-L4.

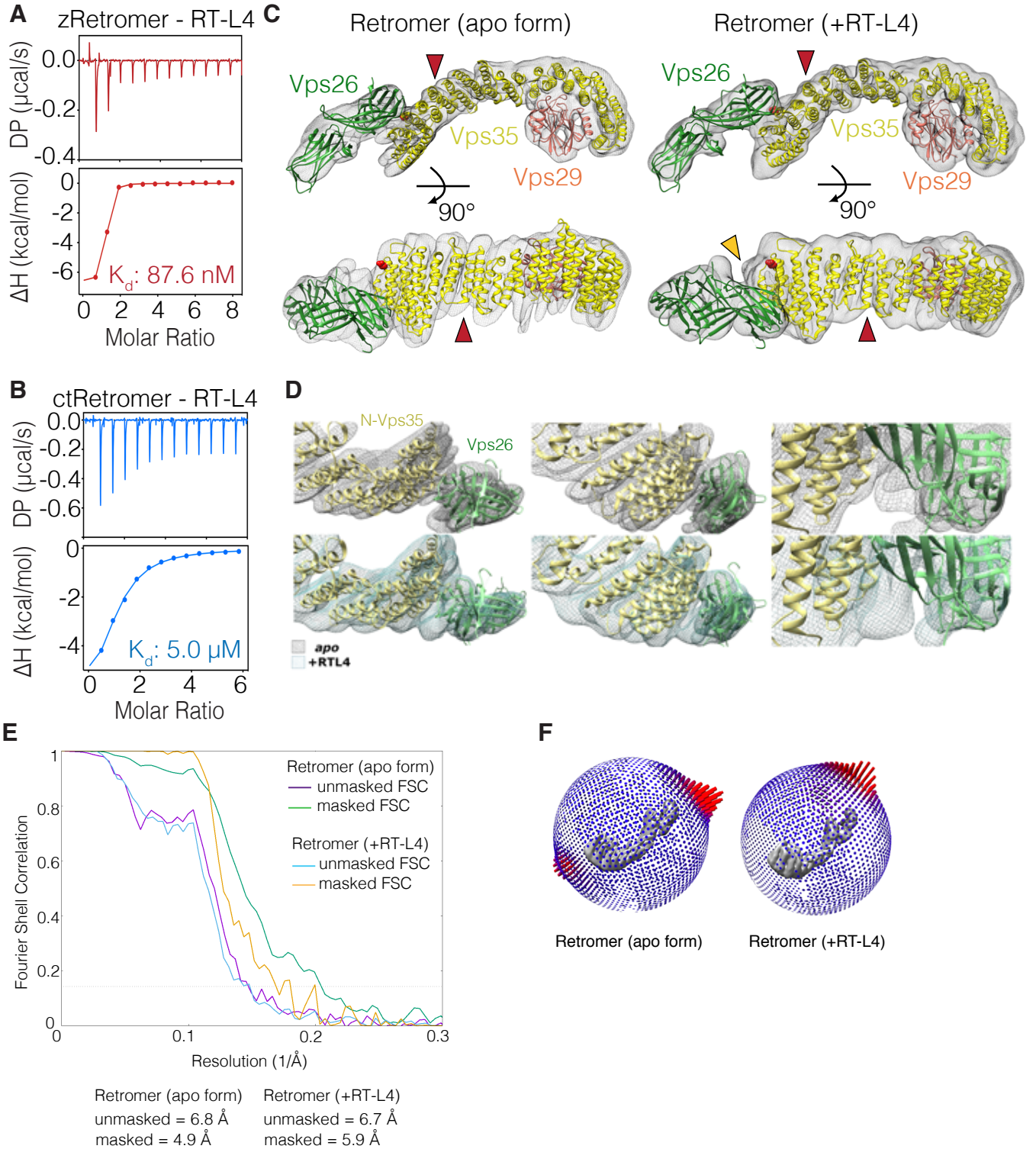

Figure S6. Binding of RT-L4 to Retromer from different species and assessed by cryoEM.
(A) ITC thermograms for the titration of RT-L4 with zebrafish Retromer showing a strong binding similar to human Retromer. (B) ITC thermograms for the titration of RT-L4 with C. thermophilum Retromer shows a lower affinity compared to zebrafish or human Retromer. The graphs represents the integrated and normalized data fit with a 1 to 1 binding ratio. The binding affinity (Kd) is given as mean of at least three independent experiments. (C) CryoEM density map of human Retromer (apo form) and in complex with RT-L4 displayed as mesh surface, with crystal structures of Retromer subcomplexes (PDB ID 2R17 and 5F0L) overlapped to the map. Red arrow indicates the Vps35 model fitting into α helices. Yellow arrow indicates the extra density observed between Vps26 and Vps35 interface in the RT-L4-bound Retromer. (D) Three different views of the Retromer CryoEM structure reconstructions highlighting the Vps35 and Vps26 interface. The cryoEM density from apo Retromer (grey mesh) is overlayed with the cryoEM density from RT-L4-bound Retromer (light blue surface). Maps were scaled to represent equivalent Å/pixel and box size in relion_image_handler and rendered in Chimera. Apo map shown at 1.096 Å/pixel and 220 pixel box size; retromer/RTL4 is shown at 1.099 Å/pixel and 228 pixel box size. (E) Fourier Shell Correlation (FSC) plots highlighting masked and unmasked resolution estimates from RELION are shown for Retromer (apo form) and in complex with RT-L4. The intersections of the curve with FSC=0.143 (grey dotted line) are shown. (F) Angular distribution of the particles used for the final round of refinement. The height and colour of the cylinder bars is proportional to the number of particles in those views.

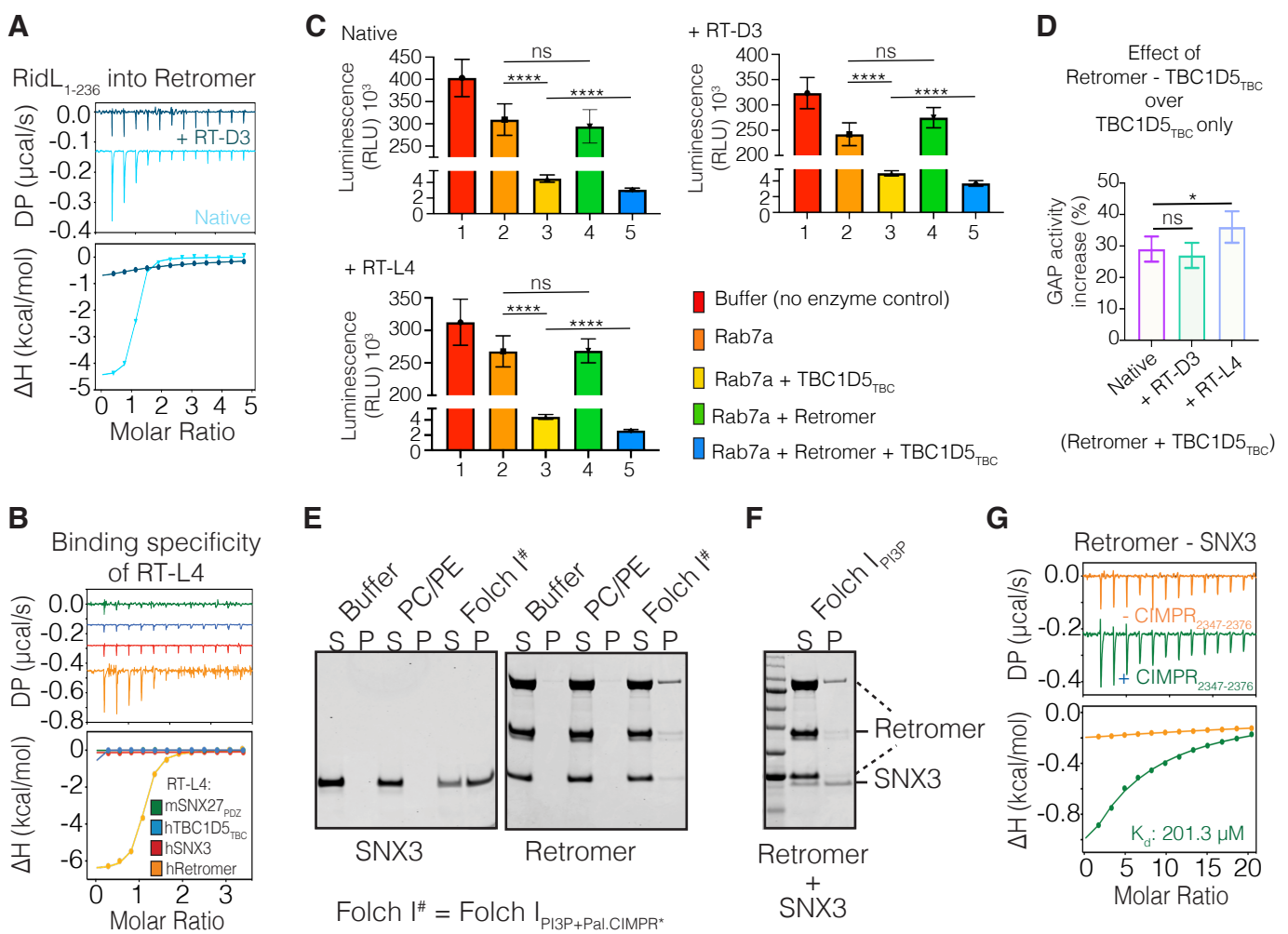

Figure S7. The effect of cyclic peptides on the interaction of Retromer with RidL, Rab7a and SNX3.
(A) ITC measurements of RidL1-236 with Retromer in the presence or absence of RT-D3. (B) Interaction of RT-L4 with Retromer, SNX27PDZ, TBC1D5TBC and SNX3 demonstrate the binding specificity of the cyclic peptide to Retromer. (C) GAP-stimulated GTPase activity of Rab7a in the presence of TBC1D5TBC and Retromer. Effect of cyclic peptide was perfomed by adding either RT-D3 or RT-L4 into the reaction. For the native control, equivalent percentage (v/v) of DMSO was added to the reaction. (D) Retromer and RT-L4 shows enhancement of GAP-stimuated GTPase activity of Rab7a over TBC1D5 alone. Two-tailed Student's t-test was utilized to determine the statistical significance (n=3). ****, $P < 0.0001$; *, $P<0.05$, ns, not significant. (E) Liposome-binding assay of SNX3 and Retromer using Folch I liposomes containing 10% PtdIns(3)P and 10% N-terminal palmitoylated CIMPR2347-2376 peptide. (F) Liposome-binding assay of Retromer and SNX3 mixture as in (E) except Folch I liposomes contain only 10% PtdIns(3)P without the CI-MPR cargo. Retromer binds only weakly to Folch liposomes in the absence of either SNX3 or cargo sequence. In all three SDS-PAGE gels, "S" indicates unbound supernatant and "P" indicates bound pellet after ultracentrifugation. (G) ITC measurement of SNX3 with Vps26A –Vps351-390 subcomplex in the presence of CIMPR2347-2376 cargo peptide. The graph represents the integrated and normalized data fit with a 1 to 1 binding ratio. The binding affinity (Kd) is given as mean of three independent experiments.

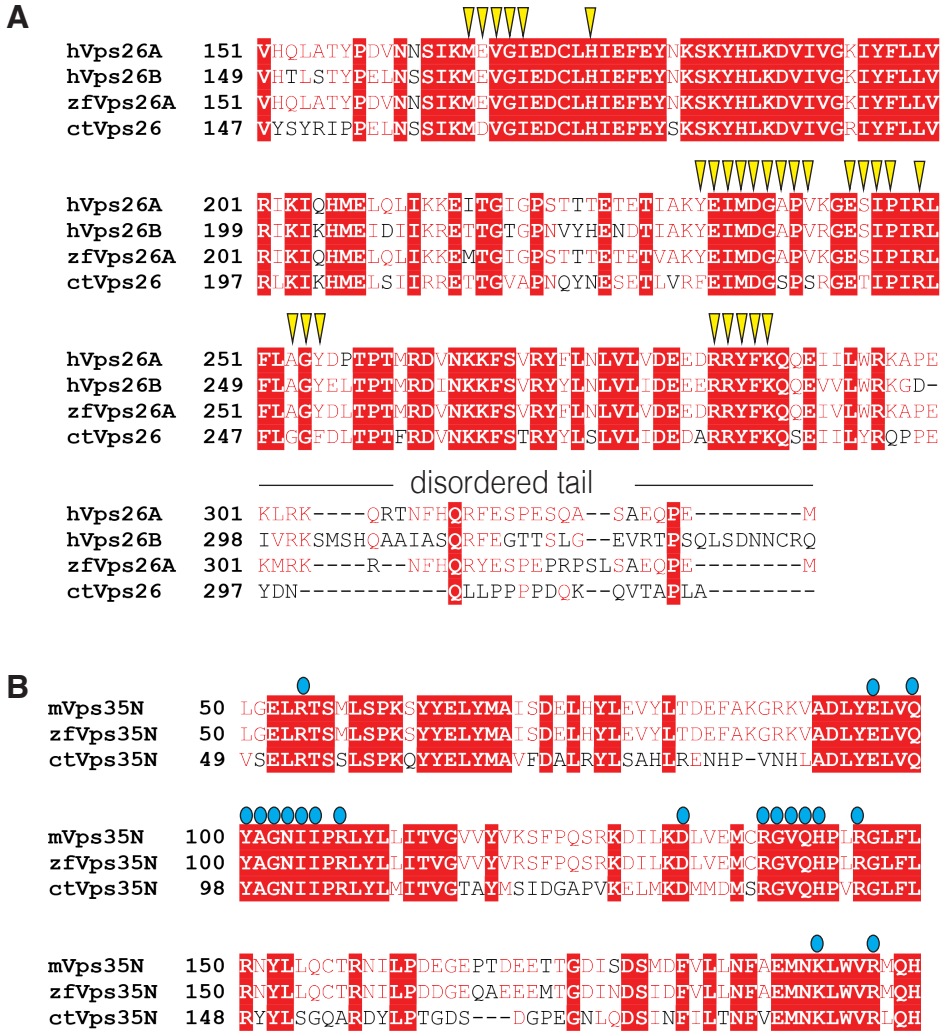

Figure S8. Sequence alignment of Vps29 and Vps35.
(A) Sequence alignment of the C-terminal region of Vps26 and (B) the N-terminal region of Vps35 showing the similarity between species. Key residues involve in contacts with Vps35 (yellow arrow) and Vps26 (blue dots) are labelled on top of the sequence. h, Homo sapiens; zf, Danio rerio; Ct, Chaetomium thermophilum; m, Mus musculus.

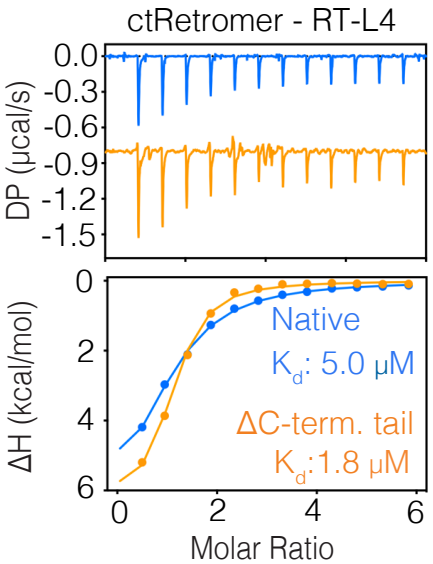

Figure S9. ctVps26 C-terminal disordered tail reveals similar autoinhibitory characteristics.
ITC measurement of RT-L4 with native and ctVps26 C-terminal tail truncated ctRetromer. The graph represents the integrated and normalized data fit with a 1 to 1 ratio binding. The binding affinity (Kd) is given as mean of at least three independent experiments.

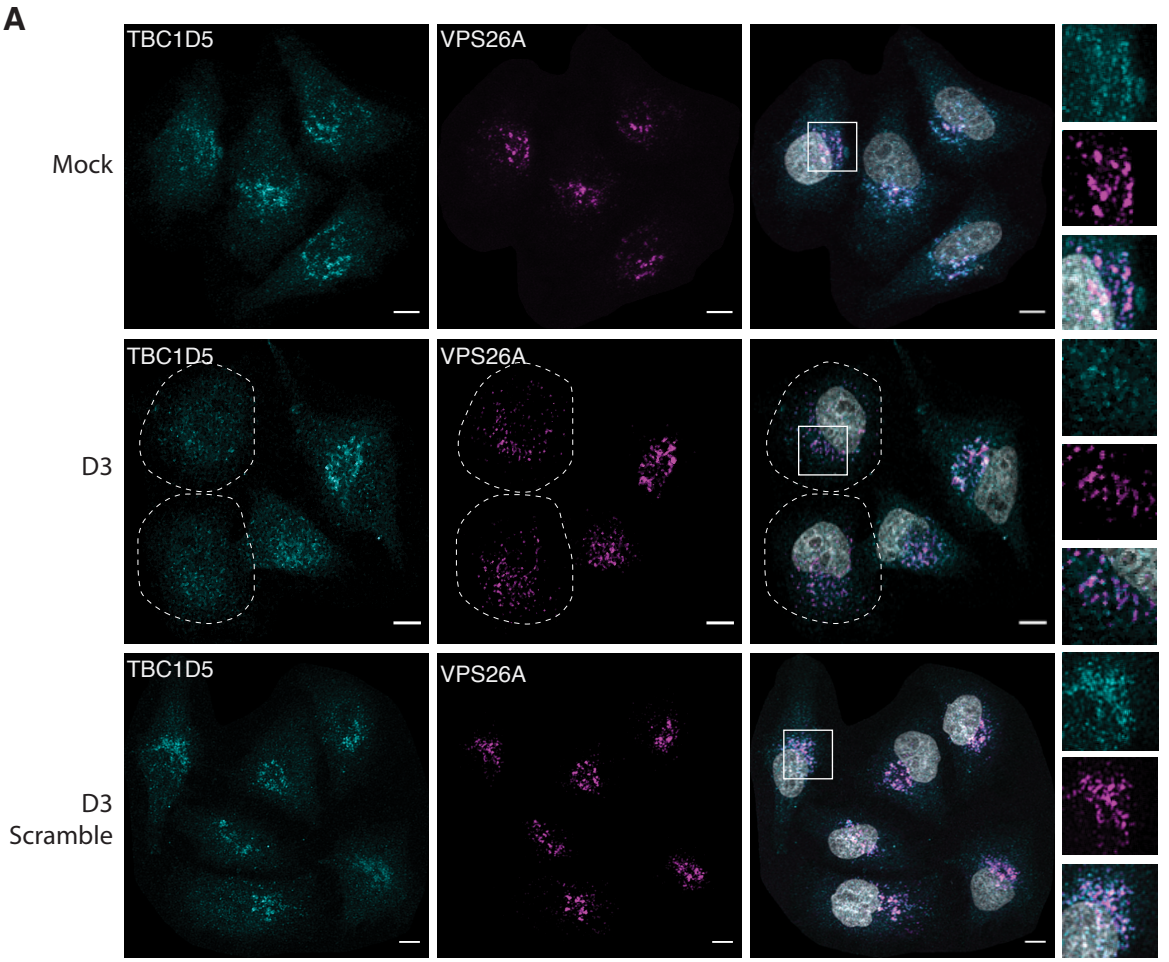

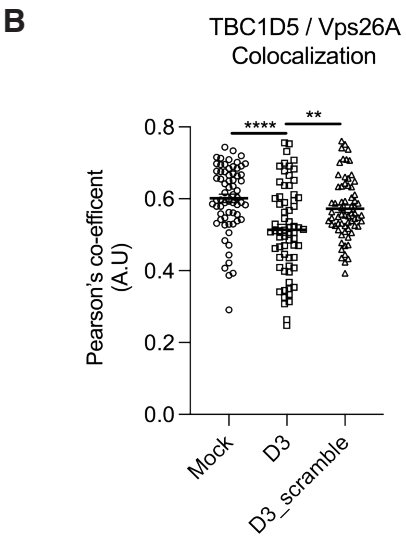

Figure S10. Electroporation of RT-D3 inhibits Retromer-dependent endosomal localisation of TBC1D5.
(A) HeLa cells were electroporated with either RT-D3 peptide or scrambled RT-D3 as a negative control. Electroporated cells were recovered for 16 h, fixed and then labelled for endogenous TBC1D5 (cyan) and Vps26A (magenta). In a large proportion of cells (indicated by dashed areas) the endosomal colocalisation of TBC1D5 with Vps26A was significantly reduced. (B) The colocalization between TBC1D5 and SNX1 was quantified by Pearson's correlation coefficient (means ± SEM). Two-tailed Student's t-test was used to determine the statistical significance (n=3). ****, $P < 0.0001$; ns, not significant.

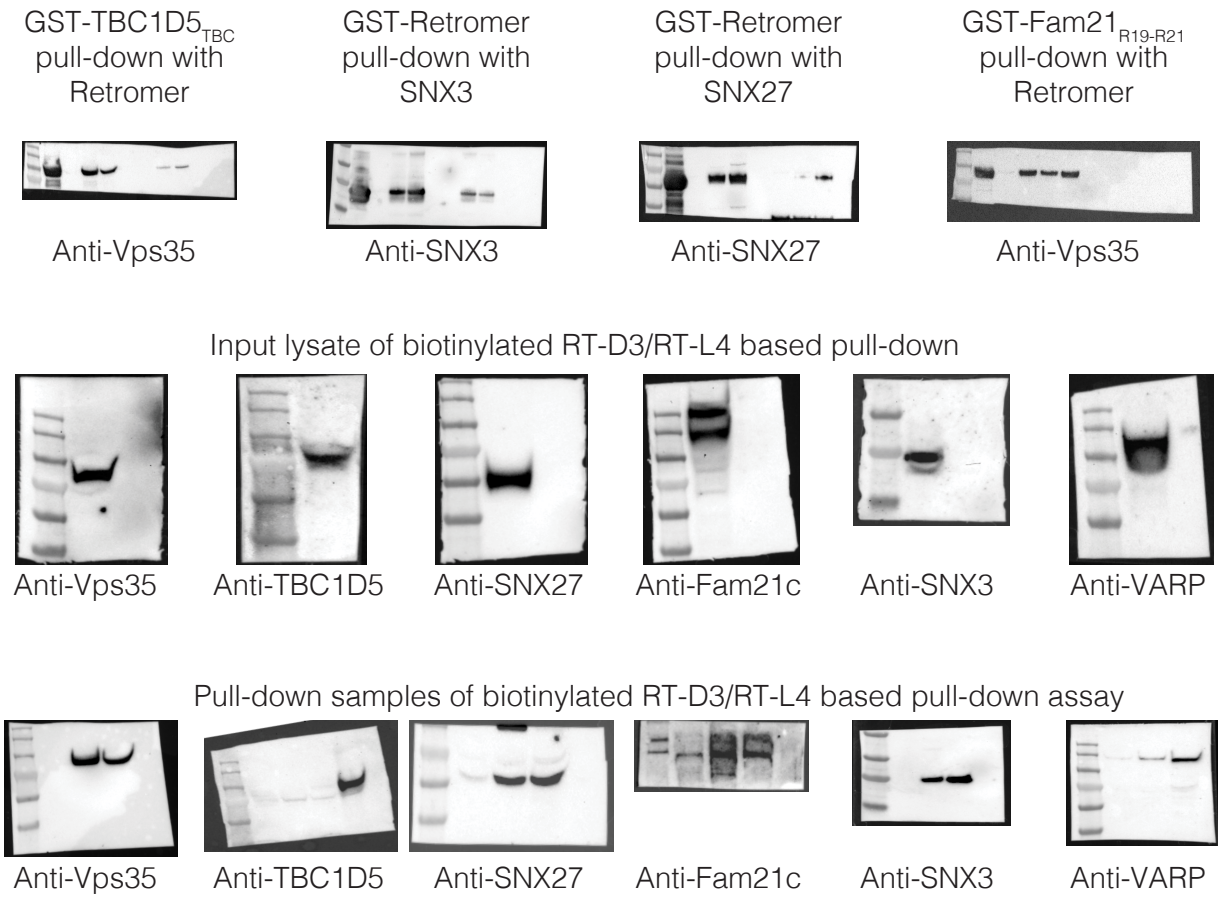

Figure S11. Unprocessed original scans of western blots for the main figure.
Unprocessed images of all blots in this study.